Development and Validation of an Aeroelastic Ground Wind Loads Analysis Tool for Launch Vehicles

Thomas G. Ivanco

Thesis submitted to the Faculty of the Virginia Polytechnic Institute and State University in partial fulfillment of the requirements for the degree of

Master of Science
in
Aerospace Engineering

Dr. Mayuresh Patil, Chair
Dr. Walter A. Silva
Dr. Rakesh K. Kapania

July 30, 2009
Blacksburg, Virginia

Keywords: Ground Wind Loads, Aeroelasticity, Launch Vehicle, Vortex Shedding

Development and Validation of an Aeroelastic Ground Wind Loads Analysis Tool for Launch Vehicles

Thomas G. Ivanco

(Abstract)

An analytical modal response tool was developed to investigate the characteristics of and to estimate static and dynamic launch vehicle responses to ground wind loads (GWL). The motivation of this study was to estimate the magnitude of response of the Ares I-X launch vehicle to ground winds and wind-induced oscillation (WIO) during roll-out and on the pad. This method can be extended to other launch vehicle designs or structures that possess a nearly cylindrical cross-section. Presented in this thesis is an overview of the theory used, a comparison of the theory with wind tunnel data, further investigation of the data to support the assumptions used within the analysis, and a prediction of the full-scale Ares I-X response. Additionally, an analytical investigation is presented that estimates the effect of atmospheric turbulence on WIO response.

Most of the wind tunnel data presented in this report is taken from the GWL Checkout Model tested in the NASA Langley Transonic Dynamics Tunnel (TDT) in April 2007. The objective of the GWL Checkout Model was to reestablish and evaluate the capability of the facility to conduct GWL testing and to operate the associated equipment. This wind tunnel test was not necessarily intended to predict the full scale Ares vehicle response to GWL; however, it can be used to help validate the newly developed analytical method described in this thesis.

A detailed GWL test incorporating updated vehicle designs and launch pad configurations of the Ares I-X flight test vehicle was also conducted in the TDT during the fall of 2008. This test provides more accurate predictions of the second bending mode response of the Ares I-X, and it models effects of the nearby tower and support structures. The proposed analytical method is also compared to select data from the Ares I-X GWL test; however, it is presented as normalized values to protect the sensitivity of the data.

Results of the proposed analytical method show reasonable correlation to wind tunnel data. Also, this method was the first to determine that second bending mode WIO response was not only possible for the Ares I-X, but will also produce the most critical loads. Finally, an explanation is offered in this thesis regarding discrepancies between wind tunnel and full-scale WIO response data.

This thesis is considered a work of the United States Government, funded in part by the National Aeronautics and Space Administration.

Table of Contents

Table of Figures

Nomenclature

a/D	Sectional amplitude (due to structural motion) to diameter ratio
Approach(es)	Phrase used to distinguish between different levels of complexity simulated within the proposed analytical method
C_D	Steady drag coefficient
C_D'	Oscillating drag coefficient for use in the aeroelastically-coupled discrete-frequency approach
C_L	Steady lift coefficient
C_L'	Oscillating lift coefficient for use in the aeroelastically-coupled discrete-frequency approach
$\widetilde{C}_L$	Lift coefficient RMS
$\widetilde{C}_{Lm}$	In-phase component of lift coefficient RMS due to structural motion
$\widetilde{C}_{Lo}$	Lift coefficient RMS for rigid structure with no turbulence
$\widetilde{C}_{LoT}$	Lift coefficient RMS for rigid structure with turbulence
D	Diameter
ESDU	Engineering Sciences Data Unit
f	Frequency (Hz)
f_{ns}	Turbulence correction factor for small values of $^{x}L_u/D$
f_{turb}	Parameter that determines the effect of turbulence upon the unsteady lift coefficient
FEM	Finite element model
f_{VS}	Vortex shedding frequency (Hz)
GVT	Ground vibration test
GWL	Ground wind loads
i	Index value of structural location along the length of the vehicle
I_u	Along-wind component of turbulence intensity, RMS divided by the mean velocity
j	Index value of structural modes in a given axis
Lock-on	Specific case of WIO where the structural motion causes an alteration of the natural vortex shedding frequency such that the vortex shedding frequency matches the structural frequency of a mode aligned orthogonal to the flow direction
NASTRAN	Name of a commercial FEM and analysis tool
OML	Outer mold line
Proposed Analytical Method	Phrase used to refer to the entire analytical method developed for and described in this thesis
PSD	Power spectral density
Re	Reynolds number
Resonant WIO Response	Phrase that describes a condition in which the

	frequency of WIO matches the natural frequency of a structural mode aligned orthogonal to the flow direction
RMS	Root mean square
S_{CLr}	Power spectral density of the lift coefficient for a rigid structure
Sigma	Standard deviation
St	Strouhal number
TDT	Transonic Dynamics Tunnel, NASA Langley Research Center
T_u	Turbulence correlating parameter
U	Free-stream velocity
$U_{60\,ft}$	Free-stream velocity at a reference height of 60 feet above the mean ground plane
V	Relative velocity, accounts for free-stream and structural motion
WIO	Wind-induced oscillation, caused by vortex shedding (one component of GWL)
X	Longitudinal axis of the vehicle (or model) in wind-axis or vehicle-axis system
Y	Axis definition, orthogonal to longitudinal axis in wind-axis system (see figure 10)
Z	Axis definition, orthogonal to longitudinal axis in wind-axis system (see figure 10)
α	Angle between the free stream velocity and the relative wind velocity that results from structural motion (see figure 10)
δ_B	Bandwidth parameter of vortex shedding, associated with turbulence-coupled approach (see equation 27)
ζ	Axis definition, orthogonal to longitudinal axis in vehicle-axis system (see figure 10)
$\zeta_{\varsigma j}$	Structural damping (ratio of critical damping) for mode *j* in the ζ axis
$\zeta_{\eta j}$	Structural damping (ratio of critical damping) for mode *j* in the η axis
η	Axis definition, orthogonal to longitudinal axis in vehicle-axis system (see figure 10)
θ_{TT}	Angle of rotation between the vehicle axis system and the wind axis system (see figure 10)
ρ	Density of fluid
ϕ	Mode shape, function of X
$\omega_{\eta j}$	Structural frequency (rad/s), of mode *j* in the η axis
$\omega_{\varsigma j}$	Structural frequency (rad/s), of mode *j* in the ζ axis
Ω_L	Vortex shedding frequency (rad/s)

Author's Acknowledgements

The author would like to acknowledge the following people for their help and contribution to this thesis work.

Dr. Mayuresh Patil – Advisor and Counselor throughout graduate work

Advisory committee, Dr. Mayuresh Patil, Dr. Walter A. Silva, Dr. Rakesh K. Kapania – Review of and assistance with thesis work and graduate studies

Dr. Bernard M. Grossman – Guidance and assistance with graduate work taken through the National Institute of Aeronautics

Stanley R. Cole and Boyd Perry III – Aeroelasticity Branch Head and Assistant Branch Head; for offering guidance, mentorship, and allotting time to pursue thesis ideas

Donald F. Keller – Development of test plans and collection of data, and the design of wind tunnel models

Marie L. Ivanco – For love, support, and understanding during graduate studies

1.0 Introduction

1.1 Problem Overview and Description

Launch vehicles erected on the pad and during rollout to the pad are exposed to atmospheric winds. The response of the vehicle to these winds can produce significant steady (mean) and oscillatory (dynamic) loads. The magnitude of these loads and oscillations, commonly referred to as Ground Wind Loads (GWL), must be considered in the design of the launch vehicle and support structures, and in the development of plans for ground and launch operations. Often the accurate prediction of the ground wind velocity is difficult and significant margin should be considered to allow for winds that could be encountered during storms, or during "rollback" when conducted to avoid an approaching storm. NASA handbooks exist to guide the design of a launch vehicle based upon the length of expected pad stay and probability of exceeding a given wind velocity (ref. 1). Structural load predictions are thereby often required for many velocities to develop wind placards for rollout and to evaluate the operational capability of a new design. The oscillatory load magnitude is sensitive to many parameters such as Reynolds number, structural damping, geometry, and flow characteristics. Due to this sensitivity, the accurate prediction or modeling of ground wind loads is often difficult.

In addition to launch vehicles, the study of flow around cylindrical or nearly-cylindrical structures is also applicable to industrial chimneys, certain designs of tall buildings, underwater pilings, and bridge supports as well as other structures. Often the study of this phenomenon has been approached independently by research efforts within the different disciplines. As a result, there has been the independent development of different analytical tools (ref. 2, 3, 4, 5) and differing conclusions regarding sensitive parameters. For example, the study of vortex shedding around underwater structures gives notice to the added mass of the surrounding fluid in the dynamics of the structure whereas other methods neglect this term. This thesis will focus upon the application of the problem to launch vehicles, but will note the potential applicability to other engineering disciplines.

1.2 Purpose and Layout of this Thesis

The purpose of this thesis is to develop and evaluate a simplified analytical method to predict the dynamic and steady response of a launch vehicle to ground wind loads. This new analytical method is expected to be useful during vehicle preliminary design and trade studies when wind tunnel testing is too expensive to evaluate each design concept and the time requirements for such testing are too prohibitive. Additionally, as discussed in Section 1.3, certain components and effects of ground wind loads cannot be predicted with wind tunnel testing and can only be evaluated analytically. Furthermore, in the steady low-turbulent flow environment of a wind tunnel, large dynamic responses are very sensitive to wind azimuth angle and velocity, and analytical results can be

used to guide testing conditions. The proposed analytical method is applicable to structures of nearly cylindrical geometry, and it does not account for the aerodynamic effects of nearby structures or multi-body vehicles. However, vehicle configurations that incorporate external dampers and stays can be simulated within the proposed method by alteration of the mode shapes and frequencies. The change in the aeroelastic response can then be evaluated while ignoring the aerodynamics associated with nearby structures.

This thesis will begin with a description of the ground wind loads problem, a presentation of the current state of the art, a discussion of the limitations of currently available techniques, and a description of the proposed analytical method. The development of the proposed analytical method and its component validation will be presented in addition to a comparison with wind tunnel data. Additional details will be provided showing capabilities of the new method to explore turbulence and gust effects upon vortex shedding lift magnitude, and the ability to model varying atmospheric turbulence and gust content. Throughout this thesis, the term “analytical method” refers to the entire analytical tool proposed in this thesis. Within this analytical method are different “approaches” each having different levels of complexity with different capabilities. The term “approach(es)” will be used to distinguish these differences, and certain components of the equations of motion and results are categorized by approach. Finally, the new analytical method is used to offer an explanation regarding discrepancies between wind tunnel data and full-scale measurements.

1.3 Components of Ground Winds and Resulting Loads

Ground winds that impact a launch vehicle can be decomposed into three separate components: a steady ground wind with a boundary layer profile, atmospheric gusts and turbulence, and the turbulent wake of nearby structures. A graphic of the wind components acting on a vehicle is shown in figure 1 and borrowed from Hanson and Jones (ref. 6).

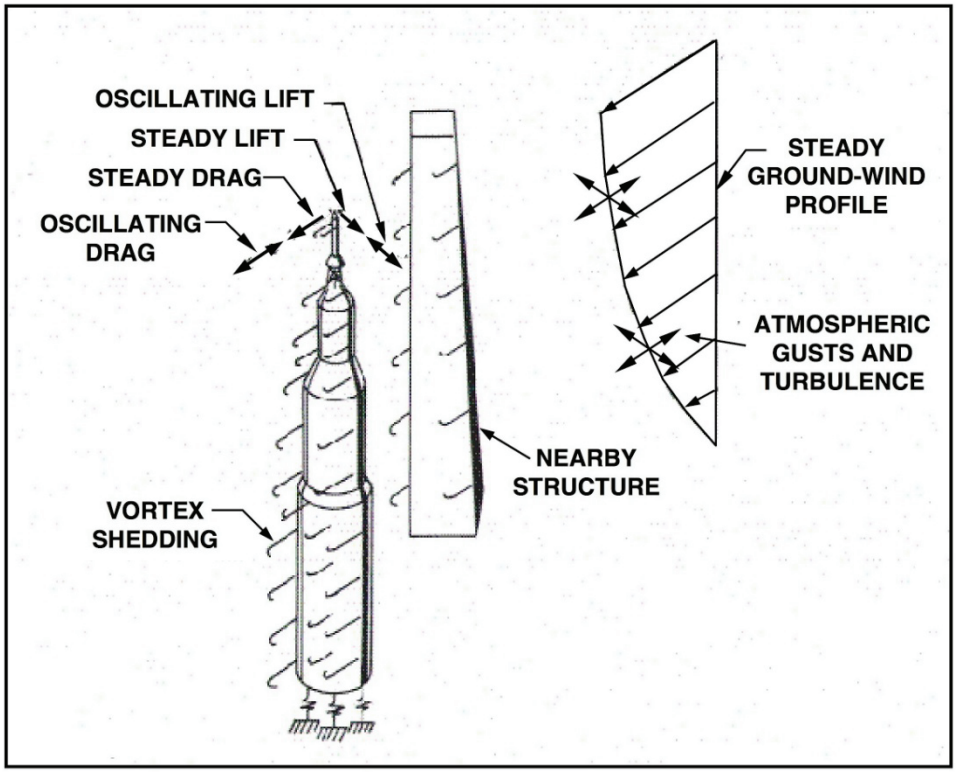

Figure 1. Components of Ground Wind and Corresponding Vehicle Response.
(used with permission from Hanson and Jones, ref. 6)

As a result of ground winds, the launch vehicle structure (or wind tunnel model) experiences a dynamic response and structural loads which can be categorized as steady (mean) and oscillatory (dynamic). The resulting structural loads can be resolved in the drag and lateral (lift) directions. Viewing the vehicle from above, drag is defined to act on the vehicle cross section parallel to the wind velocity and lift is defined to act perpendicular (90°) to the wind velocity. A conceptual plot illustrating the components of these loads as viewed from above is shown in figure 2. The response envelope, depicted in figure 2, is a cartoon representing a notional time history trace of base bending moment. The horizontal axis represents base bending moment due to drag, and the vertical axis represents base bending moment due to lift.

The material stresses that result from bending moments typically far exceed those resulting from shear forces for the launch vehicle ground wind loads problem. Therefore, bending moments are often presented in this thesis in lieu of shear forces to express the vehicle response due to lift and drag forces. It is also important for the reader to realize that the dynamic bending moment load magnitudes typically do not equal the magnitude of the aerodynamic moments. Rather, the study of GWL involves the investigation of the dynamic response of a structure with low damping undergoing oscillation where large dynamic bending

moments typically result from the inertial forces associated with the motion of the structure.

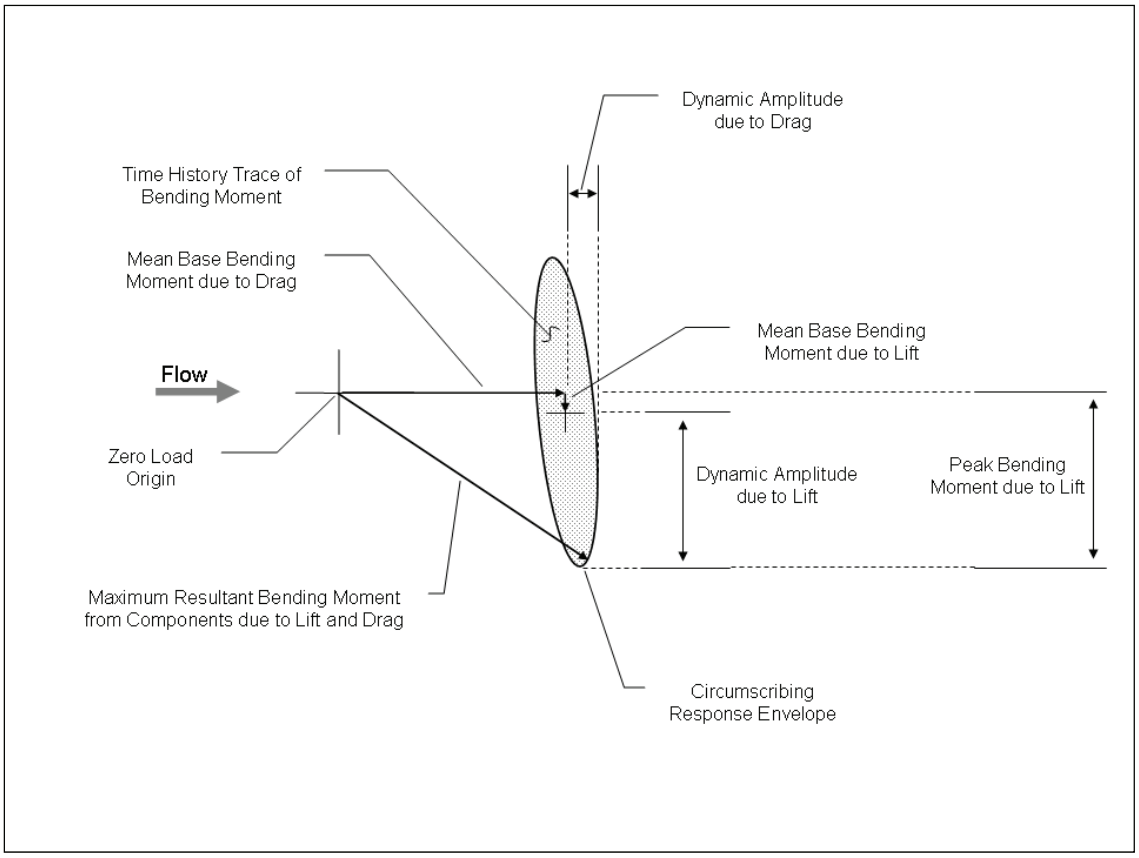

Figure 2. Components of Base Bending Moment

Mean load components are a function of a launch vehicle's outer mold line (OML) and the properties of the air flow within a wind velocity range. Typically, mean drag loads are significantly larger than the mean lift loads and are a key consideration in launch vehicle and attachment structure design.

Dynamic loads can be the result of vehicle response to flow perturbations or the result of vortex shedding. Of particular concern for launch vehicles and the primary focus of this thesis, is the dynamic response due to vortex shedding. This loading component is caused when a Kármán vortex street forms in the wake of a vehicle which results in nearly sinusoidal lift and drag loads. The response due to vortex shedding, referred to in this report as wind-induced oscillation (WIO), is a function of wind velocity, section diameter, fluid properties, and the frequency and damping of the vehicle structure. Large oscillatory loads can result if the frequency of the vortex shedding is at or near one of the natural frequencies of the vehicle and there is insufficient structural damping to dissipate the energy being imparted to the vehicle. The term "resonant WIO response" in this thesis refers to a condition when the frequency from WIO equals the

frequency of a natural mode of vibration. By nomenclature definition, this thesis also distinguishes the term “lock-on” as a specific case of WIO resonant response. Lock-on is defined here as a condition where the structural motion alters the frequency and correlation of the shed vortices, as described in Chen and ESDU (ref. 2 and 3). WIO and lock-on responses are capable of generating loads great enough to damage the vehicle or producing levels of motion that affect ground support and guidance systems.

1.4 Characteristics of Vortex Shedding and Sensitive Parameters

Vortex shedding on a cylinder is highly dependent upon the boundary layer flow at the point of separation which is governed by Reynolds number. At low Reynolds numbers, below 10^5, the boundary layer at separation is laminar and vortex shedding is periodic (ref. 2, 3 and 7). This thesis uses the term subcritical to refer to this region. At high Reynolds numbers, above 5.7×10^6, the boundary layer at separation is turbulent and the vortex shedding is also regular and periodic. Consistent with Szechenyi (ref. 7), this thesis uses the term supercritical to refer to this region. In the Reynolds number range from approximately 3×10^5 to 3.5×10^6, the boundary layer is transitioning and the wake is narrow and disorganized, and vortex shedding is irregular and broadband in frequency. This thesis uses the term transcritical to refer to this region. For Reynolds numbers of approximately 3.5×10^6 to 5.7×10^6, the vortex shedding is becoming reestablished; however, the frequency bandwidth tends to be broader than the subcritical or supercritical regions. This thesis uses the term upper-transcritical to refer to this region. Figure 3 illustrates the different flow regimes and development of vortices in the wake of a cylinder.

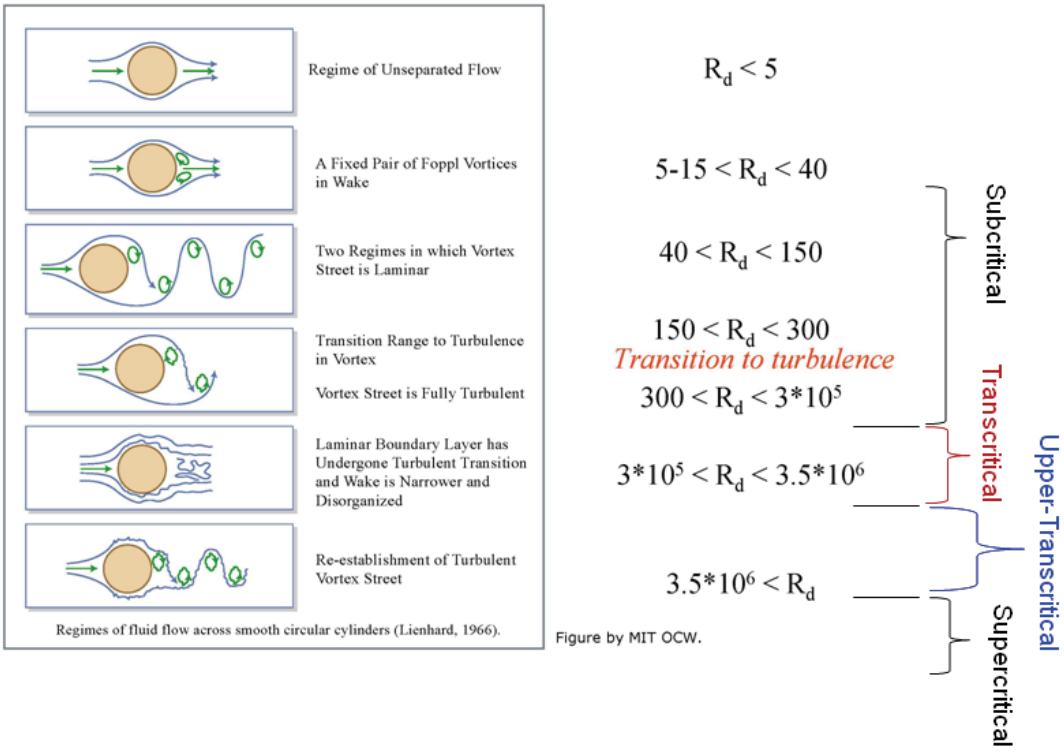

Figure 3. Characteristic Regions of Vortex Shedding.

(used with permission)

This material was created by or adapted from material created by MIT faculty member, A. H. Techet, Professor, 2005. Copyright © 2005 A. H. Techet.

Equation 1 shows the definition of Strouhal number (St), which is dependent upon velocity (*V*), diameter (*D*), and the vortex shedding frequency (f_{VS}). For a large range of Reynolds numbers, the Strouhal number for two-dimensional cylinders is in the vicinity of 0.2. Figure 4 shows the relationship of Strouhal number to Reynolds number (as defined in equation 3) based upon data acquired for two-dimensional flow on cylindrical structures.

$$\text{Strouhal number (St)} = \frac{f_{VS} D}{V} \qquad (1)$$

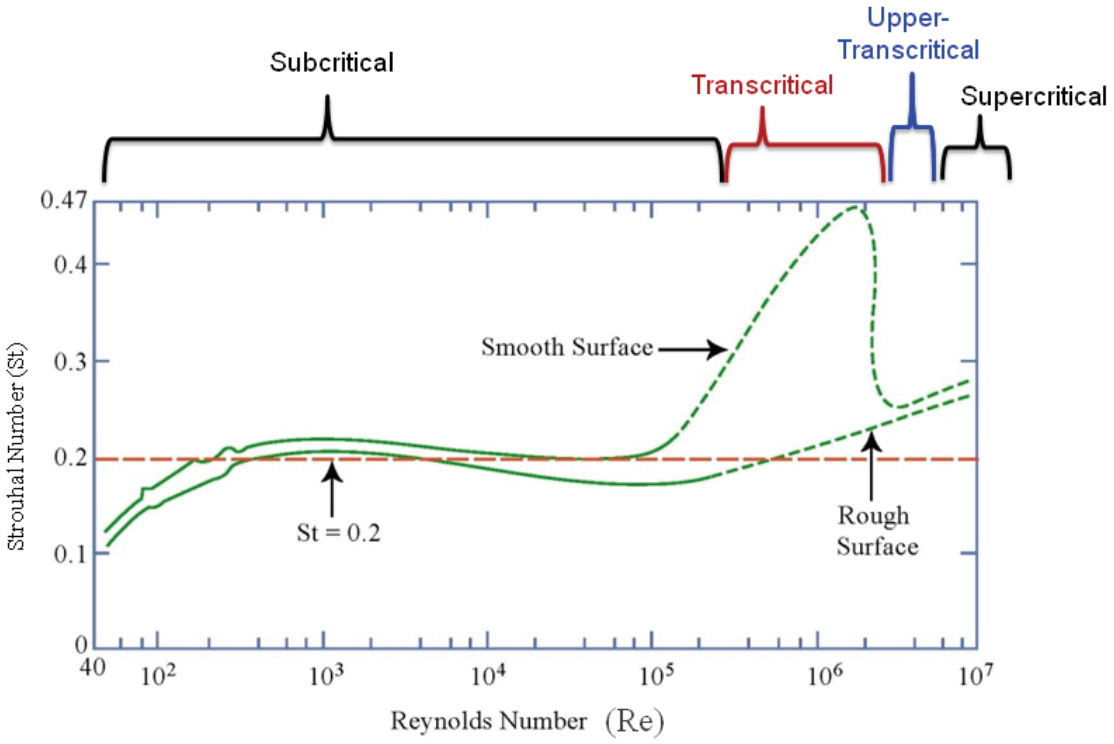

Relationship between Strouhal number and Reynolds number for circular cylinders. Data from Lienhard (1966) and Achenbach and Heinecke (1981). S~0.21 (1-21/Re) for 40<Re<200, from Roshko (1955).

Figure 4. Relation of Strouhal Number and Reynolds Number.

(used with permission)

To simulate a higher Reynolds number (for a smooth surface) surface roughness is often applied to wind tunnel models in order to increase the turbulence in the boundary layer approaching the separation point (Szechenyi, ref. 7). By applying this technique, the supercritical Reynolds number region can be simulated with subscale tests at lower Reynolds numbers.

1.5 Investigating Second Mode Response in Addition to First Mode Response

In this thesis, first bending modes refer to the fundamental modes of the launch vehicle or wind tunnel model in the horizontal axes. The η and ζ axes directions are defined in Section 4.1 as being orthogonal to the vehicle's longitudinal axis. Figure 5 is an illustration of representative fundamental mode shapes, labeled as modes 1η and 1ζ since they represent deflection in the η or ζ directions.

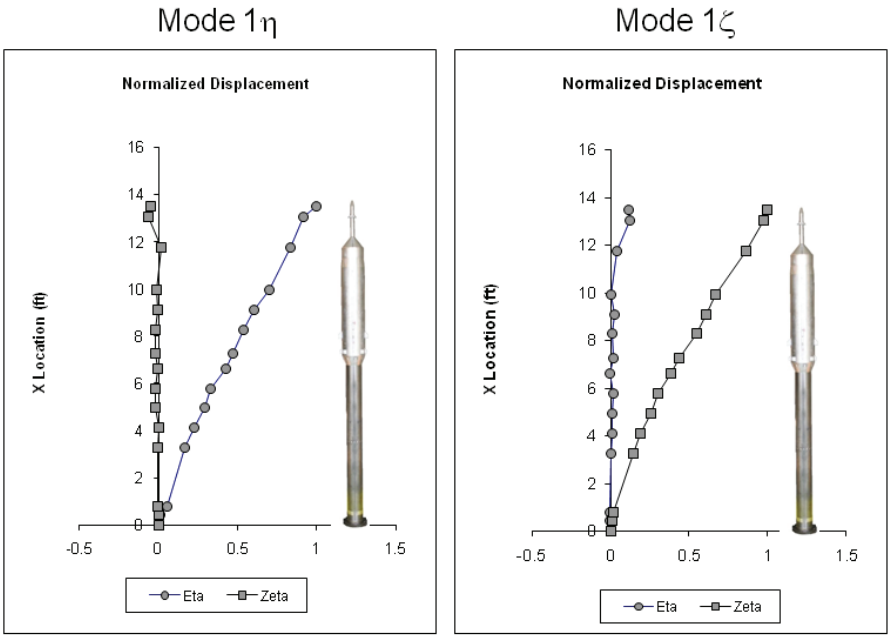

Figure 5. First Bending Modes of a Representative Launch Vehicle.

Second bending modes refer to the second natural modes of the launch vehicle or wind tunnel model. Figure 6 is an illustration of representative second bending modes labeled as modes 2η and 2ζ.

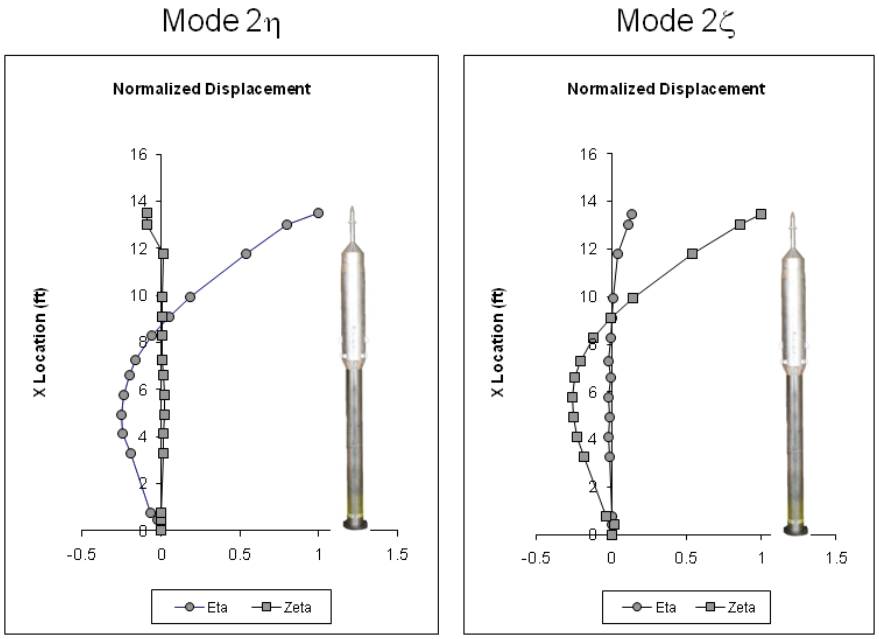

Figure 6. Second Bending Modes of a Representative Launch Vehicle.

Vortex shedding typically excites the first bending modes of launch vehicles. The dynamic responses of these modes are usually the focus of WIO analyses and wind tunnel tests (ref. 6, 8, 9, and 10). As a result of significant first bending mode deflections and load distributions, ground wind loads studies have typically driven the strength requirements for the lower portion of launch vehicles. The Ares I-X, however, has small section diameters and low natural frequencies. Therefore, the wind speed ranges where vortex shedding frequencies could align with the natural frequencies of the second bending modes are within the design ground wind speed envelope, contrary to the typical results presented by Hanson and Jones, NASA SP-8008, Farmer and Jones, and Jones and Gilman (ref. 6, 8, 9, and 10). Additionally, the load distribution associated with a second bending mode deflection is considerably different than a first bending mode deflection. Therefore, ground wind loads may drive the strength requirements of other areas of the Ares I-X in addition to the vehicle base region.

To illustrate the difference in bending moment distribution for higher modes, Figure 7 shows the normalized bending moments resulting from first mode and second mode deflections as a function of vehicle station (X) for a uniform cantilever beam (ref. 11). By inspection of figure 7, one can see that a uniform beam undergoing a second bending mode deflection has a resulting bending moment midway on the beam (in the vicinity of the anti-node) of approximately 70% of the load at the base. The same uniform beam undergoing a first mode deflection experiences a bending moment at the same axial location of only 30% of the load at the base.

Documented experimental data showing such an occurrence of a second bending mode response of a launch vehicle to WIO was not known. Therefore, investigating this unique case of second bending mode response was a unique focus of the proposed analytical method. The proposed analytical method was the first to determine that second mode response was not only possible, but will also produce the most critical loads for the Ares I-X launch vehicle.

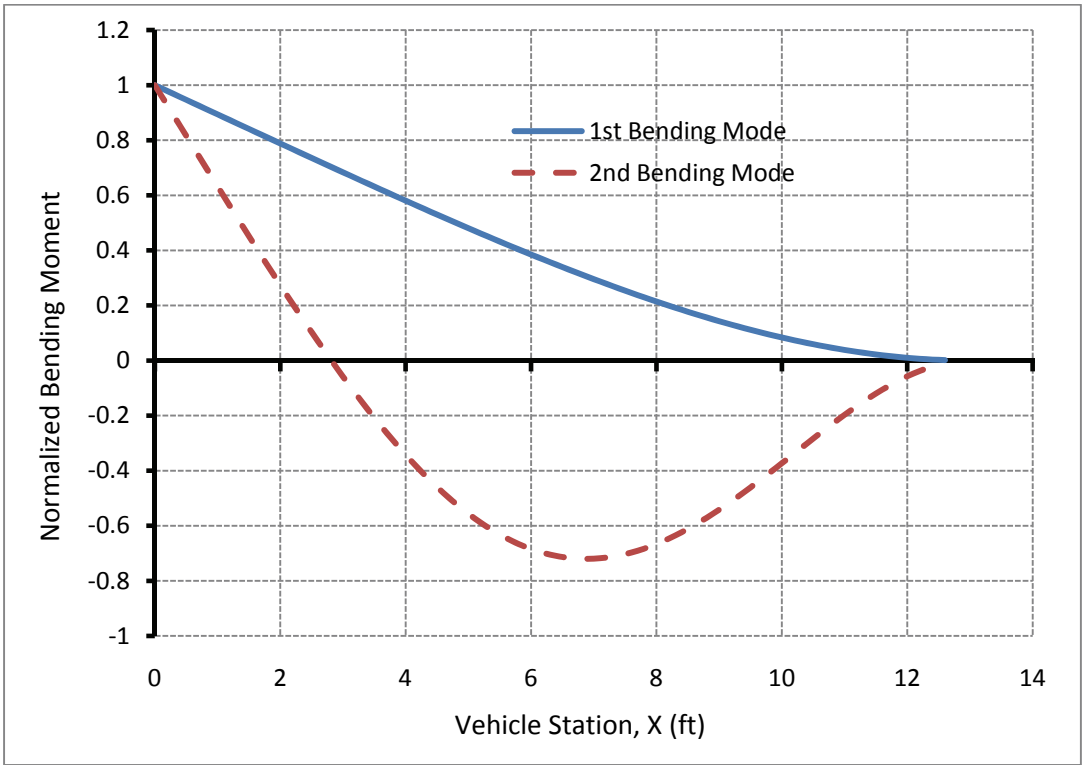

Figure 7. Bending Moment Resulting from First Mode and Second Mode Deflections for a Uniform Beam, Cantilevered at Station 0.

2.0 Current State of the Art and Limitations

2.1 NASA SP-8008, Mean Load Increase

The guidance provided in the Space Vehicle Design Criteria, NASA SP-8008 (ref. 8) is for preliminary design only and does not make an attempt to actually calculate the anticipated loads or response due to vortex shedding. Rather, uncertainty factors are proposed for preliminary design iterations to provide additional strength to endure vortex shedding loads. NASA SP-8008 recommends applying an uncertainty factor of 1.5 in the direction of flow to account for vortex shedding loads. This is adequate provided that:

1. The vehicle is designed to withstand wind loads from any azimuth.
2. The design peak wind velocity is high enough so that the predicted static loads envelope the dynamic loads encountered from vortex shedding.

In reality, the oscillatory lift force generated from vortex shedding will be applied perpendicular to the flow at a frequency proportional to the flow velocity. At some given velocity, the frequency of the forcing function will match a natural vibration mode of the vehicle and force it in resonance. The magnitude of this resonant response is highly dependent upon vehicle damping. Therefore, the actual vortex shedding loads are not proportional to the static drag loads in and around resonant WIO response conditions.

2.2 Computational Fluid Dynamics Predictions of Ground Wind Loads

Historically, computational fluid dynamics (CFD) codes have not been successful in predicting a launch vehicle's response to WIO (ref. 12). The development of CFD capabilities has been oriented around aircraft in flight whose primary aerodynamic loads involve the disturbance of the free-stream air at high velocity. Consequently, the Reynolds number averaged turbulence models within CFD codes are not formulated for separated flows and cannot correctly model the complex interaction associated with a separated vortex. It is also impractical to run direct numerical solutions for the Reynolds number range of interest and the multitude of conditions required for analysis. Another prohibition of using CFD to model ground wind loads response is that CFD predictions are often very costly requiring the use of a super computer. Acquiring these results is often time consuming and requires the creation of detailed structural and aerodynamic grids for an aeroelastically-coupled model.

Recent efforts in CFD to predict the oscillatory loads of the Ground Wind Loads Checkout Model have also been unsuccessful. The occurrence of vortex shedding has been modeled for certain wind tunnel conditions, but the calculated magnitude of the loads and the occurrence of other WIO events have not been correctly modeled.

2.3 Other Analytical Prediction Methods

The proposed analytical method is not the first attempt to predict loads resulting from vortex shedding. A literature search revealed previously developed analytical routines developed for civil engineering structures and launch vehicles. Many of these previously developed routines lack the detail required to appropriately model the problem as described in this section.

2.3.1 Method Developed by Wilmer Reed

In support of the Apollo program, Wilmer Reed developed a mathematical relation to simulate ground wind loads with the use of an analog computer (ref. 13). This relation represents the dynamic lift force as a random white-noise signal passed through a filter to replicate the atmospheric (or wind tunnel) turbulence spectra. This mostly random force is then combined with an aerodynamic damping term to model the observed self-sustained oscillations. This analytical simulation was not intended to stand alone, but rather be combined with wind tunnel data and used only to gain insight. The analytical equations alone do not attempt to capture the magnitude of dynamic response, but explain the trends.

2.3.2 Method for Predicting Response of Concrete Chimneys

D'Asdia, and Noe (ref. 5) document a method developed for calculating the WIO response of concrete chimneys. This method is rather simple and does not model many of the observed behaviors of WIO. Also, this method was developed for an industry where factors of safety are large and structural weight is not a critical performance parameter unlike launch vehicles.

2.3.3 Equations Described in Chen

Much of the proposed analytical method is inspired by Chen (ref. 2) and many of the equations of motion are of the same form. Chen presents and references a large quantity of data compiled from many tests. Even though it is discussed and documented, the equations shown in Chen do not make an attempt to predict aeroelastically-coupled events. Also, the simplified equations and coefficients recommended within Chen will produce over-conservative results for supercritical Reynolds numbers.

2.3.4 Method of ESDU Report

The Engineering Sciences Data Unit (ESDU) report (ref. 3), is a very detailed and comprehensive document on vortex shedding with data compiled from many resources. The proposed analytical method described in this thesis relies heavily on this document for the prediction of turbulence effects and three-dimensional tip effects. Finished codes are available for distribution from ESDU and results are presented in ESDU compared to full-scale and wind tunnel chimney data. However, a comparison of the ESDU code to experimental launch vehicle data is unknown.

The equations in ESDU and the input parameters are often too complex to be easily implemented from scratch. A simplified method is not offered and detailed discussion regarding the sensitive parameters is also lacking. The distinguishing features of the analytical method proposed in this thesis are:

- This thesis shows the construction of the aerodynamic equations into a modal analysis and state-space form that will quickly calculate the final result. This form of the equations of motion also enables the simulation of complex asymmetrical structures in a simple and common form that is not detailed in ESDU.
- This thesis describes the equations of motion in such a manner that the reader can build an analysis routine from scratch, whereas, the intent of the ESDU report is background information to supplement the distribution of a finished code.
- ESDU presents the dynamic lift and turbulence effects as power spectral density distributions and RMS magnitude. The current analytical method calculates the forcing functions in the time-domain and produces a time-history result.
- This thesis focuses the study around the launch vehicle problem and results are compared with launch vehicle wind tunnel data.
- Simplified versions of the proposed analytical method are presented that are far easier to implement than the complicated relations documented in ESDU. Results of a less complicated approach of the analytical method compared with wind tunnel data are presented in this thesis.

2.3.5 Proprietary Analytical Codes within Industry

Proprietary codes are also known to exist within Boeing and Lockheed Martin to predict launch vehicle response to ground wind loads. However, these codes are not available to the government or the public, nor are their accuracies known outside of the companies for which they were created. It is also important to note that all major manned and unmanned launch vehicles have undergone wind tunnel testing to evaluate their response to ground wind loads in spite of the existence of these proprietary codes.

2.4 Wind Tunnel Testing

Wind tunnel simulation is currently the only acceptable method to predict launch vehicle response to ground winds (ref. 6, 8, 9, 10, 14, and 15). However, a wind tunnel does not accurately replicate all of the atmospheric components or vehicle characteristics. The steady ground wind with a boundary layer profile is typically replaced with a steady uniform flow. The turbulent wake of nearby structures is simulated, but limited to flow and structural modeling accuracy. Typically, the atmospheric gusts and turbulence are not simulated, and the wind tunnel flow contains only its inherent turbulence content usually significantly below natural atmospheric turbulence. Finally, accurate simulation of the vehicle is difficult, and the accurate replication of scaling parameters or geometric details may not

be possible.

Aeroelastically-scaled wind tunnel models, of the type required to accurately define WIO loads, are costly to design and build as a result of their complexity. Ideally the wind tunnel model would match the full-scale values of mass ratio, Reynolds number, reduced frequency and structural damping ratio as defined in equations 2 through 5. The distinguishing difference between reduced frequency and Strouhal number (presented in eqn. 1) is that reduced frequency is based upon structural frequencies whereas Strouhal number is based upon the frequency of vortex shedding.

$$\text{Mass ratio} = \frac{\text{mass}_{\text{vehicle}}}{\text{mass}_{\text{displaced fluid}}} \quad (2)$$

$$\text{Reynolds number (Re)} = \frac{\rho V L}{\mu} \quad (3)$$

$$\text{Reduced frequency}^{1} = \frac{f_{\text{structural mode}} D}{V} \quad (4)$$

$$\text{Damping ratio } (\zeta) = \frac{\text{C}}{\text{C}_{\text{critical}}} \quad (5)$$

Some references refer to the Scruton number as a critical modeling parameter to characterize vortex shedding response. Scruton number is simply a combination of the mass ratio and damping ratio presented in equations 2 and 5. Therefore, for the same value of structural damping, a wind tunnel model will match the Scruton number of a full-scale vehicle provided that the above aeroelastic scaling parameters are also matched. Additionally, Mach number matching is typically not important provided that the wind tunnel or atmospheric velocity is below a Mach number of 0.3 and incompressible assumptions can be made.

Timing of wind tunnel test results can also be problematic. As a result of the model complexity, design and construction is a lengthy process that can take several months to a year in time. Additionally, analyzing the complex data and reporting the results can take several months. As a result, the wind tunnel data may not be available to the design and operations community for over a year after the completion (or freezing) of the vehicle design.

2.5 Typical Use of Analysis Combined with Wind Tunnel Results

The oscillatory responses that are difficult to accurately simulate in wind tunnel tests are those due to atmospheric turbulence and gusts. Therefore, these components of the vehicle response are typically determined analytically and

[1] Reduced frequency is defined here in a non-standard fashion utilizing frequency in Hz, in lieu of rad/s, and length as diameter, in lieu of semi-chord. This non-standard definition allows a direct comparison of reduced frequency with Strouhal number.

assumed to occur independently of WIO response (ref. 6, 8, and 16). Also, accurate boundary layer profiles are difficult to simulate in wind tunnels and corrections are often made in order to present the data as a function of an appropriate “representative” velocity (ref. 6, 8, and 16). This section will illustrate the combination of analytical and wind tunnel results as suggested by Hanson and Jones (ref. 6). More importantly, this section will also discuss the significant discrepancies observed between combined analytical-wind tunnel results and measured full-scale loads.

Atmospheric turbulence can cause oscillations in both the lift and the drag directions and in this thesis refers to the relatively random perturbations in local flow velocity. Gust in this thesis refers to the change in mean ground wind velocity that causes structural oscillations in the drag direction. Gust loading can be applied as either a single discrete gust with a cycle period tuned to the vehicle natural frequency (tuned gust), or as a statistical process in the form of a power spectral density (PSD) distribution. Hanson and Jones (ref. 6), mention the later is more representative of the atmosphere and also offers the opportunity to simulate turbulence in a very similar fashion.

Hanson and Jones (ref. 6) describe a two-part method to correct experimental test data in order to account for boundary layer profiles, turbulence and gusts. The first part involves the “modification” of the velocity value of uniform wind tunnel flow to an equivalent full-scale reference height velocity with a boundary layer profile. The second part involves the computation of dynamic response to atmospheric turbulence and gust, and the combination of this calculated response with that acquired in the wind tunnel. It is important to note that this typical analysis of turbulence and gusts is not aeroelastically-coupled, but is rather a fixed forcing function being applied to a structural model.

The first part of the correction method requires a definition of the atmospheric boundary layer profile. NASA-HDBK-1001 (ref. 1) specifies the atmospheric boundary layer to use for design as a function of reference height velocity for vehicles at Kennedy Space Center. The specified boundary layer has increasing velocity as a function of altitude where many sections of the vehicle will be exposed to flow velocities significantly higher from that at the standard reference height of 60 feet. To reduce uncertainty regarding the effect of the boundary layer profile, Hanson and Jones (ref. 6) recommend “finding an equivalent uniform velocity which distributed along the vehicle gives the same steady-state bending moment at the base as the design ground wind profile.” This procedure produces a velocity mapping for relating uniform flow velocity to a boundary layer profile. Presenting the wind tunnel results as a function of the equivalent reference height velocity would yield a more accurate representation of the full-scale loads with respect to atmospheric winds (ref. 6, 8, and 16). This adjustment does not affect the magnitude of the wind tunnel loads, but rather changes the velocity value for which wind tunnel data represents. This typical

boundary layer correction may produce inaccurate velocity mapping as WIO may be associated with a specific vehicle section that is exposed to a velocity that may not be represented by the “equivalent” velocity.

The second part of the correction method involves modifying the magnitude of the wind tunnel measured loads by combining the analytical turbulence and gusts response with the wind tunnel data. As illustrated in figure 8, the ellipse representing the envelope of the calculated dynamic response to turbulence and gusts is centered about the mean value measured in the wind tunnel. Hanson and Jones (ref. 6) suggests shifting the wind tunnel response envelope such that the mean is on the boundary of the calculated turbulence/gust response envelope producing a curve from which the maximum bending moment magnitude (wind tunnel + calculated results) can be determined.

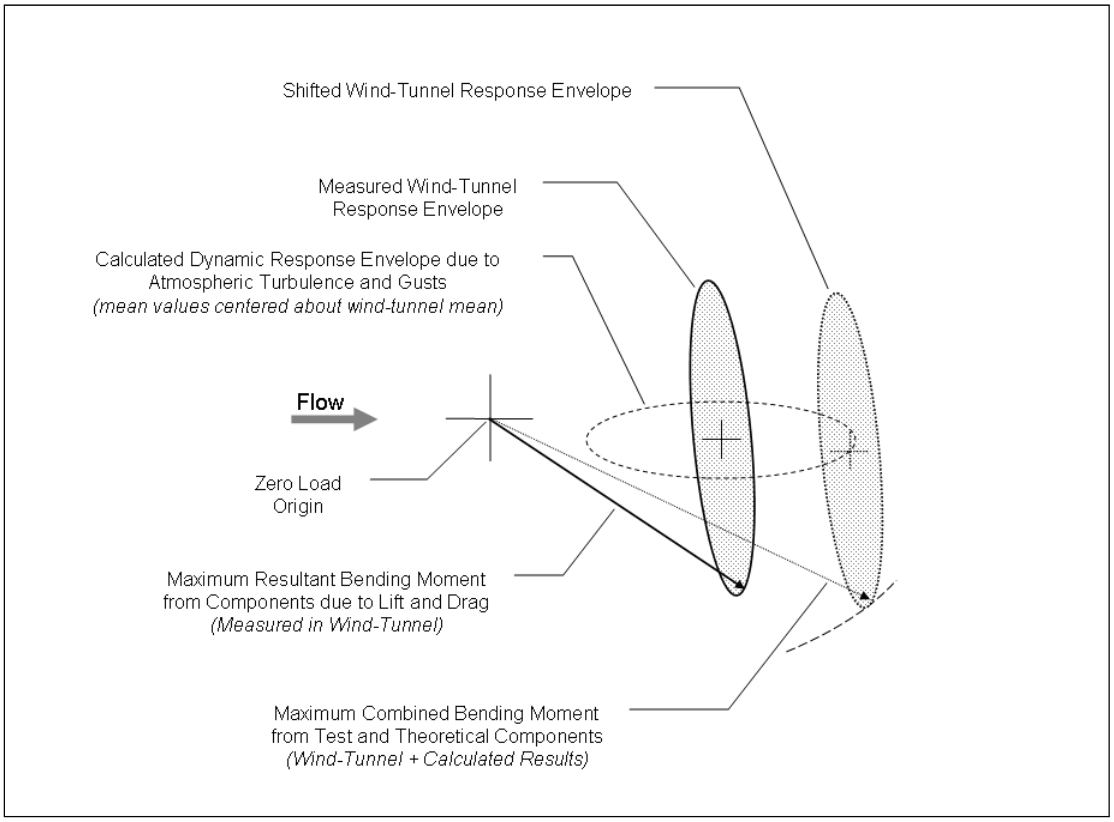

Figure 8. Concept Sketch for Traditional Method of Determining Maximum Combined Loads using Wind Tunnel Data and Analysis.

The maximum combined bending moment (wind tunnel + calculated) illustrated in figure 8 appears to be a conservative and reasonable estimate. However, Foughner and Duncan (ref. 17) show that full-scale response data measured on a Jupiter launch vehicle is several times larger than the maximum combined bending moment predicted from wind tunnel and analytical methods. Additionally, Runyan, Morgan and Mixson (ref. 15) also show that full-scale loads

measured on a Scout launch vehicle exceed the “corrected” wind tunnel results. Furthermore, it was also a finding of a NASA meeting on ground wind loads (ref. 18) that better understanding and correlation is needed between wind tunnel, analytical and full-scale results. However, little work has been found that addresses this lack of correlation.

The proposed analytical method, described in this thesis, is capable of producing load predictions due to gust and turbulence that are coupled with WIO response. This thesis will therefore make an attempt to explain the discrepancy between wind tunnel and full-scale data noted by Foughner and Duncan (ref. 17), and Runyan, Morgan and Mixson (ref. 15).

2.6 Need to Improve Current State of the Art

A need exists for a GWL analysis tool that allows trade studies and intelligent decisions during preliminary vehicle design. Lessons learned throughout the development of launch vehicles during the Apollo program have expressed the need to accurately evaluate WIO earlier in the design of launch vehicles than wind tunnel testing allows (ref. 19). The new analytical tool needs to be quick to implement and flexible enough to adapt to different vehicle configurations. Load predictions from the new analytical tool should envelope maximum peak loads acquired from experimental data resulting from WIO. Additionally, the ability to model aeroelastic coupling between structural motion and aerodynamic loads is needed in order to properly scale wind-tunnel results for various structural damping values. Finally, the ability to investigate the effect of turbulence on the forces associated with WIO is needed. As a result, a new analytical tool can lead to intelligent early design decisions and can guide wind tunnel testing of final configurations or assist in the development of wind placards and damping and stay devices for a full-scale vehicle.

3.0 Proposed Analytical Method

3.1 Method Description

The proposed analytical method is a modal analysis technique developed and run within MATLAB and originally motivated by the Ares program at NASA. The dynamic characteristics of a launch vehicle structure are reduced into a linear sum of the natural modes of vibration. Associated with each mode is a generalized coordinate describing the time-varying magnitude of the modal deflection. The accuracy of the structural model is limited only by the detail of an associated finite element model (FEM). It is important to note that this is not a beam analysis, but rather a modal analysis of the launch vehicle with the capability to model complex and asymmetric structures in addition to the study of configurations with stays and damper systems. When a detailed FEM is not yet developed for a new vehicle, estimated beam bending mode shapes, frequencies, and damping can be used.

Within the code, the vehicle is discretized into small cylindrical sections along its length. Each discrete section has a specified diameter, mean velocity, Reynolds number, Strouhal number, and time-varying displacement. Time-varying aerodynamic forcing functions are developed based upon historical wind tunnel data of two-dimensional cylinders (of applicable Reynolds number) undergoing dynamic motion. The magnitude of each sectional aerodynamic forcing function is dependent upon section diameter, mean velocity (Reynolds number), and motion of the discrete section among other parameters. These aeroelastically-coupled time-varying forces are multiplied by the mass-normalized mode shapes to create generalized forces with respect to time. A Runge-Kutta routine is employed to solve the equations in the time domain. This time domain solution is iterated until the dynamic displacement of each mode is converged. The influence due to surface roughness and protuberances is not directly modeled; however, the effects can be estimated by proper selection of the two-dimensional aerodynamic coefficients. Additionally, a complex “approach” of the proposed analytical method includes the simulation of free-stream turbulence and its affect on WIO loads (aeroelastically-coupled turbulence-coupled approach).

Corrections are made to the aerodynamic loads to account for three-dimensional and tip effects in the following manner. For all approaches, the Strouhal distribution is altered in the tip region. For the aeroelastically-coupled turbulence-coupled approach, the vortex shedding strength and the effect of turbulence are also corrected for the finite length based upon the vehicle’s “fineness ratio” (H/D). ESDU (ref. 3) provides details regarding the nature of vortex shedding around the tip of a chimney for various fineness ratios. Additionally, Ivanco and Keller (ref. 20, and 21) present launch vehicle wind tunnel data that supplements the theory and data presented in ESDU.

The proposed analytical method can be easily adapted to launch vehicles of any geometry, mode shapes, and frequencies, provided that the vehicle is generally cylindrical in cross-section and is single-body. Extensions to chimneys, submerged pilings, or other similar structures can also be made.

3.2 General Assumptions

The following assumptions were made in generating and evaluating the analytical method:

A1) The mode shapes are assumed to match those of the FEM.
A2) The frequencies are assumed to match those of the FEM.
A3) The mass distribution is assumed to be consistent with the FEM.
A4) The KSC boundary layer profile is assumed to be as specified in NASA-HDBK-1001 (ref. 1) for a 3-sigma maximum velocity profile distribution.
A5) It is assumed that local (discrete vehicle section) lock-on will occur within the velocity range described by Chen and ESDU (ref. 2 and 3) based upon local flow properties and geometry.
A6) It is assumed that the dynamic response of the vehicle can be represented as a linear sum of the mode shapes (method of assumed modes).
A7) The aerodynamic loads are assumed to be closely represented by a series of discrete two-dimensional forcing functions spanning the length of the vehicle with diameters representative of the vehicle OML, and corrections made for three-dimensional effects.
A8) The Strouhal number is assumed to vary due to three-dimensional effects as presented within this thesis.
A9) The bending moment loads are assumed to be linearly proportional to displacement (linear structure).
A10) The effects of protuberances are assumed to be negligible provided that proper aerodynamic coefficients are selected. However: experimental results, discussed by Chen and SP-8008 (ref. 2 and 8), describe extreme changes in the dynamic response of a model with the introduction of very small geometric changes such as a strip of tape or protuberance. It is hypothesized that these geometric changes can either incite or disrupt vortex shedding synchronization and lock-on. Therefore, it is theorized that the maximum possible amplitude and loads are independent of these details and can be enveloped by assuming a large area of synchronization for a given diametrical section. As a result of this assumption, the output of the analytical model is not expected to match the response of the wind tunnel model or vehicle (due to the lack of protuberance modeling and current simulation limitations) with respect to wind azimuth angle changes. However, the maximum predicted loads from the analytical model are expected to be representative of the maximum possible loads physically encountered by the wind tunnel model or vehicle.

3.3 Layout of the Analytical Model

A setup code is run to produce the geometry of the vehicle, the discrete step size, the Strouhal number distribution, and mass-normalized mode shapes. The output matrices of this setup code are then read by the combined aero-structural code that specifies the aerodynamic values and calls a Runge-Kutta ODE routine to step through time. Deflections are calculated as a generalized coordinate output, and then adjustments are made to the aerodynamic input values based upon the calculated local deflections. This iteration repeats until the solution is converged and outputs a time history of vehicle displacement for a given free-stream velocity and boundary layer profile. A flow chart of the analytical method is shown in figure 9.

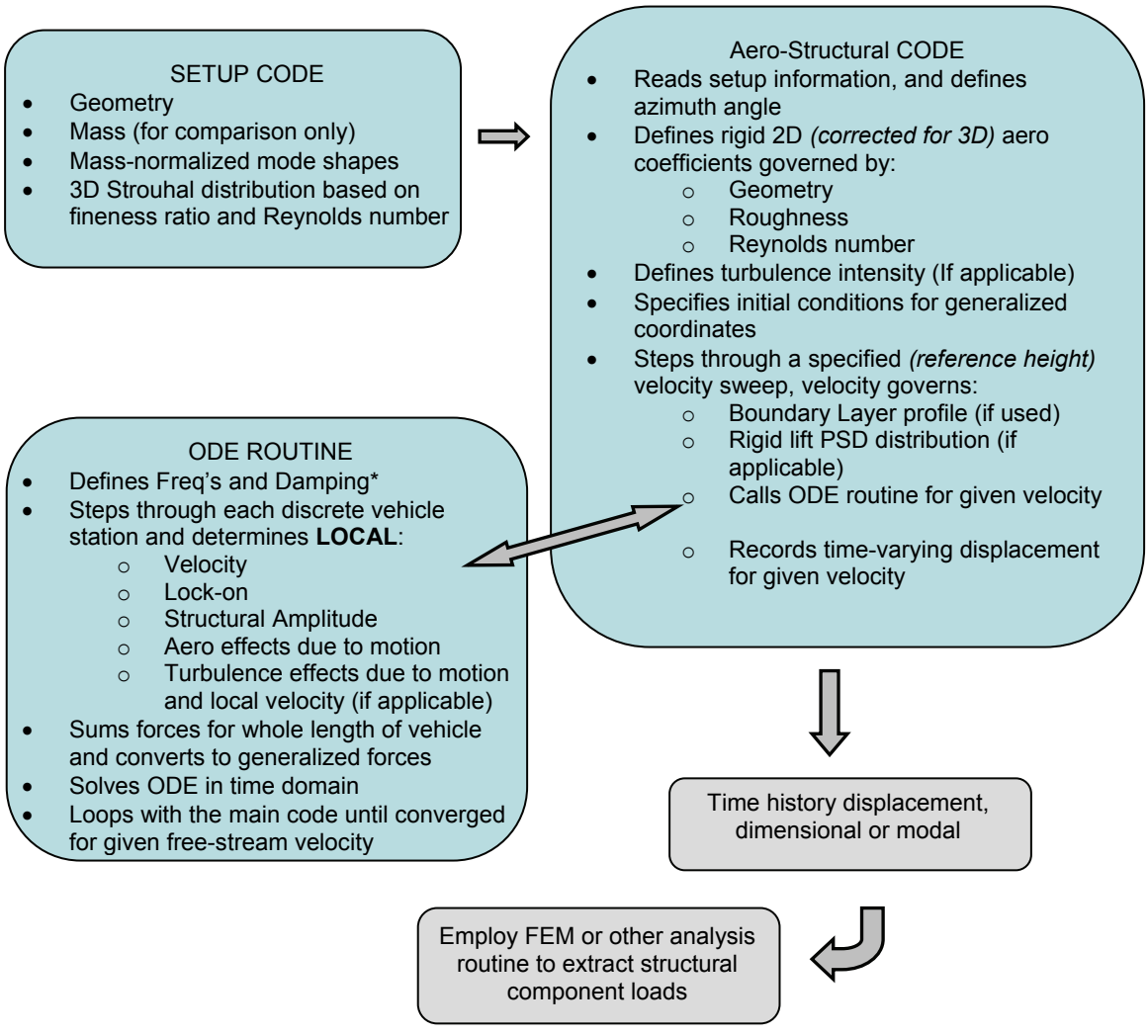

Figure 9. Flow Chart of the Proposed Analytical Method.

* *Frequencies and Damping are defined in the ODE routine in lieu of the setup code in order to reduce computational time.*

4.0 Equations of Motion

4.1 General

The coordinates defined in the proposed analytical method are as specified in figure 10 with the X coordinate positive vertically from the tail towards the nose of the vehicle, and the wind-axis system denoted by *Y* and *Z* in the directions shown. The vehicle axis components are denoted by η and ζ, are fixed to the vehicle, and represent the fundamental axes of the vehicle. Therefore, the modal vibrations will occur in the η or ζ axis.

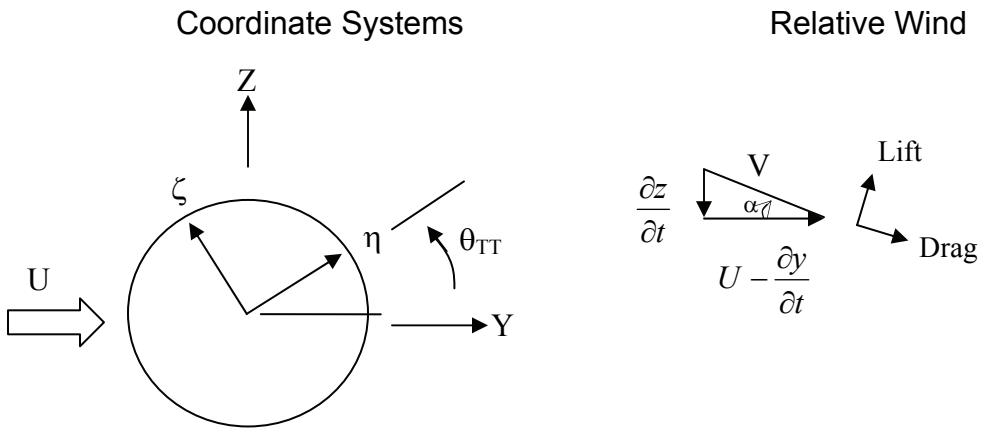

Figure 10. Definition of Coordinate System and Direction of Positive Force.

The lift and drag components can be determined as a time-dependent sum of the quasi-steady, vortex shedding, and turbulence/gust components of the aerodynamic force for a discrete vehicle section.

$$Drag_{Section} = \frac{1}{2}\rho V^2 DC_D dx + Drag_{vortex+turbulence} \quad (6)$$

$$Lift_{Section} = \frac{1}{2}\rho V^2 DC_L dx + Lift_{vortex+turbulence} \quad (7)$$

$$Forces_y = Drag_{Section}\cos(\alpha) + Lift_{Section}\sin(\alpha) \quad (8)$$

$$Forces_z = Lift_{Section}\cos(\alpha) - Drag_{Section}\sin(\alpha) \quad (9)$$

where,
C_L and C_D are the sectional steady lift and drag coefficients
$Drag_{vortex+turbulence}$ and $Lift_{vortex+turbulence}$ are the sectional components due to vortex shedding and turbulence/gust as described in Section 4.2.4
dx = section height (geometrical step size of discrete model)
V is the relative flow velocity, $V = \sqrt{\left(U - \frac{\partial y}{\partial t}\right)^2 + \left(\frac{\partial z}{\partial t}\right)^2}$,and in terms of η and ζ is:

$$V = \sqrt{\left(U + \dot{\varsigma}\sin\theta_{TT} - \dot{\eta}\cos\theta_{TT}\right)^2 + \left(\dot{\varsigma}\cos\theta_{TT} + \dot{\eta}\sin\theta_{TT}\right)^2}$$

The calculation of the relative velocity (*V*) as shown is done to account for local structural motion and the resulting flow angularity (α). This creates an aerodynamic damping term and is a more accurate representation of the applied loads for large deflections. For a simplified analysis, the free-stream velocity (U) can be used in lieu of V, and one can also assume that α=0 placing drag in the Y-direction and lift in the Z-direction. Making these simplifications decreases the computation time; however, the maximum structural velocity must be considerably less than the wind velocity in order for this simplification to be valid. For the range of conditions and structural motion considered in the current study, these simplifications have a negligible impact on the results. This may not be the case for applications of this method to other disciplines or conditions with large structural motion.

θ_{TT} represents a rotation of the vehicle axis system with respect to the wind axis system such that the axis Y is always in the flow direction and the axes η and ζ are aligned with the natural modes of the structure. This is analogous to the turntable angle used in wind tunnel data. Rotating the forces into the vehicle axis system yields:

$$Forces_{\eta} = Forces_{y}\cos(\theta_{TT}) + Forces_{z}\sin(\theta_{TT}) \quad (10)$$

$$Forces_{\zeta} = Forces_{z}\cos(\theta_{TT}) - Forces_{y}\sin(\theta_{TT}) \quad (11)$$

The resulting motion of the vehicle in the η and ζ vehicle axis directions is a function of vehicle station (X) and time (t). By using generalized coordinates and mode shapes, one can separate the time-varying and spatial components as shown in equations 12 and 13. The time-varying generalized coordinates are denoted as *q*, and are associated with a specific mode shape ϕ. The subscripts η and ζ denote the axis of deflection for a particular mode, and the sub-subscript "*j* " denotes the mode number in the respective axis.

$$\eta(x,t) = \sum_{j=1}^{\#Modes} q_{\eta_j}(t)\phi_{\eta_j}(x) \quad (12)$$

$$\varsigma(x,t) = \sum_{j=1}^{\#Modes} q_{\varsigma_j}(t)\phi_{\varsigma_j}(x) \quad (13)$$

The mode shapes in the vehicle axis system, $\{\phi_{\eta,\zeta}\}$ are mass-normalized such that the relation in equation 14 holds. It is important for the reader to notice that the mode shape magnitudes are important. The equations of motion are only valid if the relation in equation 14 is met.

$$\{\phi_{\eta,\varsigma}\}^T [M] \{\phi_{\eta,\varsigma}\} = 1 \qquad (14)$$

In this report, the subscript *"i"* is the index for discrete vehicle stations along the X-axis (referred to as the node number), and the mode shape vectors are *i*x1 in size for each mode. The mass matrix [M] is square with a size of *ixi*.

For any system where the mass of the displaced fluid is not an order of magnitude below the mass of the structure, one needs to consider the relation in equation 15 for each diagonal entry of the mass matrix M. For launch vehicles in air, the added mass terms can be neglected and the mass matrix can consist of only the structural mass. However, this may not be the case for other systems such as underwater structures where the added mass terms in equation 15 become relevant.

$$M_{ii} = m_i + C_m M_{d_i} \qquad (15)$$

where,
m_i is the mass of the discrete vehicle section
M_{d_i} is the mass of the displaced fluid for the vehicle section, $M_{d_i} = \rho \pi R^2 dx$
C_m is the added mass coefficient of the fluid as a function of Mach number, C_m = 1.0 for Mach << 1

The decomposition of the structural motion into generalized coordinates and mode shapes requires the forces to be converted into generalized forces (Q), as shown in equation 16. If *j* modes are considered in the η and ζ directions, then Q is a vector of size 2*j* x 1.

$$\{Q(t)\} = \begin{Bmatrix} \sum_{i=1}^{\#nodes_j} \left(Forces_\eta \; abs\left(\phi_{\eta 1}\right)\right)_i & \text{for 1st mode in } \eta \\ \sum_{i=1}^{\#nodes_j} \left(Forces_\varsigma \; abs\left(\phi_{\varsigma 1}\right)\right)_i & \text{for 1st mode in } \varsigma \\ \vdots & \\ \text{higher modes} & \end{Bmatrix} \qquad (16)$$

The absolute value of the mode shape deflection is used in equation 16 because of the manner in which the equations of motion are written. Some approaches of the proposed analytical method use a discrete frequency aerodynamic forcing which may be in phase for various sections of the vehicle. If this in-phase forcing function exists along various sections of the vehicle undergoing a second beam bending mode (or higher) response, the generalized force would otherwise be reduced in magnitude as a result of the sign change in modal deflection along the length of the vehicle.

Casting the EOM's in the form of generalized coordinates and mode shapes yields the relation shown in equation 17.

$$\begin{Bmatrix} \ddot{q}_{\eta_1} \\ \ddot{q}_{\varsigma_1} \\ \vdots \\ \ddot{q}_{\varsigma_j} \end{Bmatrix} + \begin{bmatrix} 2\zeta_{\eta 1}\omega_{\eta 1} & 0 & \cdots & \\ 0 & 2\zeta_{\varsigma 1}\omega_{\varsigma 1} & & \\ \vdots & & \ddots & 0 \\ & & 0 & 2\zeta_{\varsigma j}\omega_{\varsigma j} \end{bmatrix} \begin{Bmatrix} \dot{q}_{\eta_1} \\ \dot{q}_{\varsigma_1} \\ \vdots \\ \dot{q}_{\varsigma_j} \end{Bmatrix} + \begin{bmatrix} \omega_{\eta 1}{}^2 & 0 & \cdots & \\ 0 & \omega_{\varsigma 1}{}^2 & & \\ \vdots & & \ddots & 0 \\ & & 0 & \omega_{\varsigma j}{}^2 \end{bmatrix} \begin{Bmatrix} q_{\eta_1} \\ q_{\varsigma_1} \\ \vdots \\ q_{\varsigma_j} \end{Bmatrix} = \{Q(t)\} \qquad (17)$$

where,
Q(t) is the generalized aerodynamic force shown in equation 16
$\zeta_{\eta j}$ and $\zeta_{\varsigma j}$ are the modal damping terms, fraction of critical, for mode *j* (in η or ζ)
$\omega_{\eta j}$ and $\omega_{\varsigma j}$ are the frequencies of mode *j* (in η or ζ) in rad/s

In general, all modes of vibration from the fundamental modes up to a frequency of f_{max} (Hz), defined in equation 18, should be considered. This relation will identify the modes that could be excited by vortex shedding for the range of velocities from zero to velocity$_{max}$. For the current study of the Ares launch vehicle, four modes were included in the analysis (*j* =2): 1st and 2nd beam bending modes in the η and ζ directions.

$$f_{\max}(Hz) = \frac{0.25 \cdot velocity_{\max}(ft/s)}{D_{average}(ft)} \qquad (18)$$

The equations of motion can be represented in state-space format as shown in equation 19, where the vector {y} has a size of 4*j* x 1

$$\{\dot{y}\} = \begin{bmatrix} [0] & [I] \\ -[\omega^2] & -[2\zeta\omega] \end{bmatrix} \{y\} + \begin{Bmatrix} \{0\} \\ \{Q(t)\} \end{Bmatrix} \qquad (19)$$

$$\{y\} = \begin{Bmatrix} \{q\} \\ \{\dot{q}\} \end{Bmatrix} \qquad (20)$$

Where,
{Q(t)}, [2ζω], and [ω^2] are the vector and matrices shown in equations 16 and 17

This state space equation is solved in MATLAB using a time-marching Runge-Kutta routine (ode45). The resulting output is a time-domain solution of the generalized coordinates.

To derive a physical displacement for any point along the vehicle, the generalized coordinate output values can be multiplied by the normalized mode shapes as shown in equations 12 and 13.

4.2 Details Regarding Components of the Equations of Motion

For clarity, certain details regarding the equations of motion were not discussed in the previous section. Specifically: the determination of structural damping and frequencies, mode shapes, vortex shedding frequencies, lift and drag forces due to vortex shedding and turbulence, and the extraction of bending moment loads from the time history displacement. The calculations of all of these components are detailed in this section.

4.2.1 Determination of Structural Damping

Structural damping can be estimated by comparing a new vehicle design with existing vehicles or through component tests and analytical means. NASA SP-8079 (ref. 22) contains structural damping values for free-free modal tests of many launch vehicles. Although these values are not for cantilever supported vehicles, the results can provide valuable insight. When no other information is available, a structural damping value of 0.5% of critical ($\zeta_{\eta j}, \zeta_{\varsigma j} = 0.005$) is considered to be conservative.

Actual structural damping values for the vehicle mounted in the rollout and/or launch configurations can be determined from full-scale dynamic tests following vehicle buildup. The actual values should be acquired and compared with the estimated values used in design to determine the conservatism with regard to ground wind loads calculations and operational limitations and placards.

4.2.2 Determination of Mass-Normalized Mode Shapes and Frequencies

There are two manners proposed here to determine the mass-normalized mode shapes. The first involves estimation from beam theory followed by proper scaling to satisfy equation 14. The second involves extraction from FEM codes.

4.2.2.1 Mode Shape and Frequency Estimation in Early Design

Some knowledge of the vehicle structural properties is required before an estimate can be done of the mode shapes and frequencies. Of particular importance is an estimate of the mass distribution and the structural stiffness. Once these properties are determined, Euler beam theory can be used to estimate the cantilever frequencies and mode shapes. Once a mode shape is estimated, the magnitude can be adjusted such that equation 14 is satisfied for each mode. Meirovitch (ref. 11) offers equations for cantilever beam mode shapes and frequencies for specified properties of mass and stiffness.

4.2.2.2 Mode Shape and Frequency Extraction from Detailed FEM Design

Mode shapes and frequencies are typical outputs from FEM codes. However, a detailed model may provide too much information to gain usable mode shape deflections. In this case, a curve fit to the centerline deflection of the vehicle will suffice. Also, defining the mode shape as an equation will allow easy adjustment

of the longitudinal step size (length of discrete vehicle sections) within the proposed analytical method.

Some FEM codes, such as NASTRAN, offer the capability to output mass-normalized mode shapes. This may ease the application of the mode shapes within the proposed analytical method; however, great care must be exercised to ensure proper unit conversion. For example, the English unit of length within NASTRAN is often inches. This will create a mass unit of slinch (in lieu of slugs). If the length units of the analytical method are ft, then the user is required to scale the NASTRAN mode shapes by a factor of $1/\sqrt{12}$ in order to satisfy equation 14.

4.2.3 Distribution of Strouhal Number

ESDU 96030 (ref. 3) provides equations and charts showing the typical variation of Strouhal number in the tip region (within 2 to 3 diameters) for parallel sided or tapered structures. According to ESDU, the Strouhal distribution for a conical structure is shown by equation 21. Also in accordance with ESDU, a parallel sided structure (or one with a small amount of taper >> 0.02) has a tip Strouhal number of 0.16 that merges into the value predicted by equation 21 as the distance from the tip increases beyond a value of 0.43D. It is mentioned in ESDU that these relations are based upon wind tunnel studies where data in the supercritical range is very limited and not considered. For any significant wind velocity, the Ares I-X (like many launch vehicles) will be in the supercritical Reynolds number range. Also like many launch vehicles, the Ares I-X contains several taper changes and diameter steps in the vicinity of the tip and it does not fall into a category of a simply tapered or parallel sided structure. Therefore, direct application of the equations shown in ESDU is not recommended for many launch vehicle designs and the user should apply judgment and caution when correcting for tip effects.

$$St = St_{2D}\left(1 - 0.4\exp\left(-1.6\left(r'/D\right)\right)\right) \qquad (21)$$

Where,
r' = distance from the tip
St_{2D} = Strouhal number for two-dimensional flow at the appropriate Reynolds number

While the exact distribution of Strouhal number in the tip region resulting from various geometries may be difficult to predict, it is rather certain that the value of Strouhal number in the tip region will be significantly lower than the equivalent two-dimensional value. Also, wind tunnel data of Ares-like vehicles (ref. 20) contains evidence of supercritical tip shedding. The data presented by Ivanco and Keller (ref. 20) indicate that the predominant tip Strouhal number is lower than shown by ESDU (ref. 3) and is in the vicinity of 0.14. The unsteady pressure data also shows that this value may extend throughout the tip region. Using the data presented by Ivanco and Keller as a guide in addition to ESDU,

the tip Strouhal distribution on Ares-like vehicles was separated into three areas. First, the narrow launch abort system (LAS) tower has a large height to diameter ratio and was treated as a region dominated only by two-dimensional flow. Second, the highly tapered region of the command module was treated as a conical structure with a Strouhal distribution described by equation 21. Third, the region from the base of the command module to 2 diameters below the base of the command module was treated as a parallel sided structure with a Strouhal number equal to 0.14. As a result, the tip region Strouhal number distribution, for Ares-like vehicles, is as shown in figure 11.

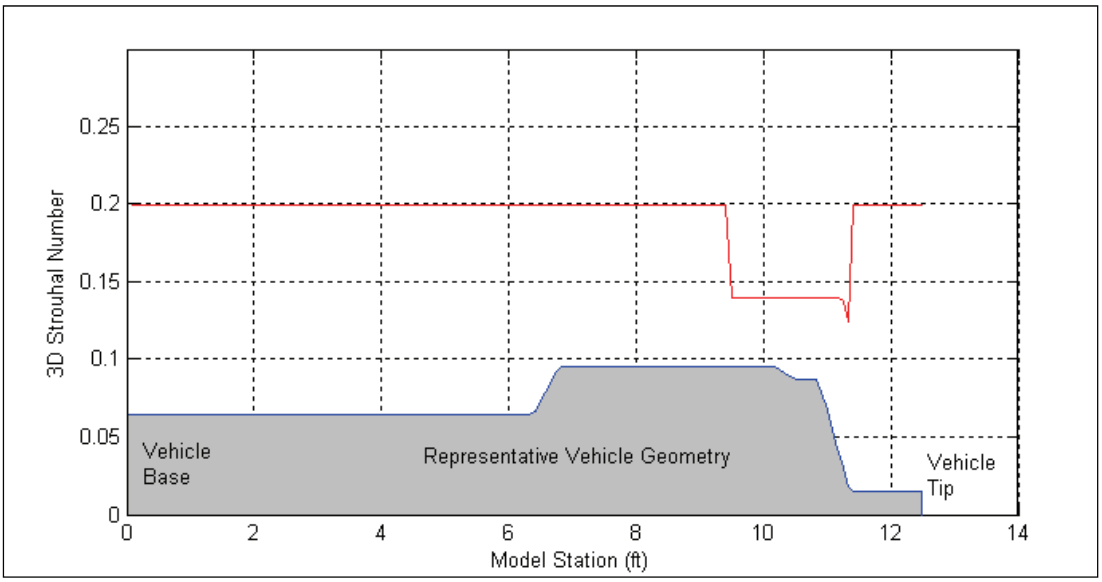

Figure 11. Longitudinal Distribution of Strouhal Number for Ares-Like Launch Vehicles

It is theorized that the lower Strouhal numbers obtained by experiment (0.14 in lieu of 0.16 for the tip region) may be caused by the existence of protuberances on the launch vehicle. The addition of a protuberance will create a wider wake and increase the *effective* diameter of the vehicle section. This larger effective diameter may also be represented as a lower Strouhal number when based upon the actual geometric diameter of the same section. Furthermore, two-dimensional Strouhal numbers in the supercritical range are expected to be above 0.2 and a function of velocity, as was shown in figure 4. However, experimental data on Launch vehicles with protuberances (ref. 20) in the supercritical Reynolds number range yield slightly lower than predicted values. Therefore, to simplify the analytical method, a value of 0.2 was chosen as a two-dimensional reference Strouhal number for all velocities.

4.2.4 Detailed Sectional Lift and Drag Forces

There are three separate approaches described in this thesis to represent the sectional lift and drag forces resulting from vortex shedding and turbulence. Each approach is increasingly more complex and offers better representation of

the problem. The three approaches discussed in this thesis are:

1. Simplified Approach. Contains harmonic aerodynamic forcing functions with fixed coefficients (results not shown). The frequency of the forcing varies based upon section diameter, sectional wind velocity and sectional Strouhal number.

2. Aeroelastically-Coupled Discrete Frequency Approach. Contains aerodynamic forcing functions that are discrete in frequency and independent for each discrete section of the vehicle. The magnitudes of the aerodynamic loads are dependent upon the motion for each vehicle section, and the frequency is dependent upon the section diameter, sectional wind velocity, and sectional Strouhal number.

3. Aeroelastically-Coupled Turbulence-Coupled Approach. This is similar to the aeroelastically-coupled discrete frequency approach where the magnitudes of the aerodynamic coefficients are dependent upon motion and discrete section properties. However, the dynamic lift forcing functions also have a frequency bandwidth governed by sectional motion and free-stream turbulence. Additionally, the turbulence intensity affects the magnitudes of the aerodynamic coefficients.

4.2.4.1 Simplified Approach

Within the simplified approach, the aeroelastic coupling is ignored and conservative values of the oscillating lift and drag coefficients are chosen. These coefficients are fixed and the method is not aeroelastically-coupled. As a result, a convergence routine is not required and the solution is rapidly calculated. Inputs for turbulence and gust forcing are still available; however in this approach they will be treated as independent quantities and will not affect the WIO forcing.

The sectional lift and drag forces are calculated as shown in equations 22 and 23 based upon the data presented in Chen (ref. 2).

$$Lift_{vortex+turbulence} = \frac{1}{2}\rho U^2 DdxC_L' \sin(\Omega_L t) + h' \qquad (22)$$

$$Drag_{vortex+turbulence} = \frac{1}{2}\rho U^2 DdxC_D' \sin(2\Omega_L t) + g' \qquad (23)$$

where,
C_L' = 0.4 for supercritical flow, C_L' = 1.2 for subcritical flow
C_D' = 0.8 for supercritical flow, C_D' = 1.0 for subcritical flow
h' = 0 for smooth flow, or a time-varying across-flow turbulence as desired
g' = 0 for smooth flow, or a time-varying along-flow turbulence/gust as desired
$\Omega_L = \frac{2\pi StU}{D}$, unless lock-on as shown in equation 24
dx = section height (geometrical step size of discrete model)

The condition of lock-on is expected to occur when the relation in equation 24 is satisfied. If lock-on occurs, the vortex shedding frequency is altered to match the structural frequency of the mode aligned orthogonal to the flow direction. Therefore, for each discrete vehicle section within the analytical method a condition statement evaluates the shedding frequency.

$$\begin{aligned} &if: \quad 0.95\omega_n < \Omega_L < 1.1\omega_n \\ &then: \quad \Omega_L = \omega_n \end{aligned} \tag{24}$$

where,
Ω_L = vortex shedding frequency (rad/s)
ω_n = structural natural frequency of the mode(s) aligned nearly orthogonal to the flow direction (rad/s)

4.2.4.2 Aeroelastically-Coupled Discrete Frequency Approach

Within the aeroelastically-coupled discrete frequency approach, the sectional lift and drag forces are calculated using the same equations as that shown for the simplified approach in equations 22 and 23. Also, the lock-on condition represented in equation 24 is utilized. However, the values of the unsteady lift and drag coefficients are dependent upon structural motion. Chen (ref. 2), has compiled two-dimensional cylinder data from a multitude of wind tunnel tests ranging in Reynolds number from a few thousand to 19×10^6. The data is shown as fluctuating force coefficient amplitudes as a function of cylinder (sectional) motion. These coefficients are intended for use as sinusoidal amplitudes (peak C_L) similar in manner to that shown in equations 22 and 23 as C_L' and C_D'. Considering the range of Reynolds number, surface condition, structural motion, and material presented in Chen, there is reasonable scatter in the presented data. A slightly conservative curve fit was applied to the presented data and is shown in equations 25 and 26 applicable to upper-transcritical and supercritical Reynolds numbers. These values, however, may be un-conservative for subcritical Reynolds numbers.

$$\begin{aligned} C_L' &= -1.6(a/D)^2 + 1.36(a/D) + 0.3, \quad for\ (a/D) \le 0.5 \\ C_L' &= -0.36(a/D) + 0.8, \quad for\ (a/D) > 0.5 \end{aligned} \tag{25}$$

$$C_D' = 3.667(a/D) + 0.15 \tag{26}$$

where,
(a/D) = local peak amplitude to diameter ratio.

Initial conditions of modal displacement and velocity, and sectional peak amplitude (a/D) are assumed. An iteration of the ODE is then run and generalized coordinate response is predicted. New sectional peak amplitudes (a/D) are determined by multiplying the peak generalized coordinate response by the local value of the corresponding mode shape (independently in the η and ζ axes). When more than one mode shape (in the η and ζ axes) is simulated, then

the peak amplitude of the combined response should be considered to derive (a/D). The new (a/D) values are then used to determine new sectional force coefficients (equations 25 and 26), and the routine is iterated until converged.

It is acknowledged that for many flow conditions the aerodynamic WIO forcing will not be sinusoidal but will contain broadband content. It is also acknowledged that for many velocities far removed from a resonant WIO condition the response may be commensurate with a lowly damped structure exposed to random forcing. The present aeroelastically-coupled discrete frequency approach will not properly capture or represent these responses. However, ESDU (ref. 3) states that the WIO forcing associated with large amplitude oscillations is relatively independent of turbulence, Reynolds number, and surface roughness. Additionally, the data presented by Ivanco and Keller (ref. 20), portions of which are presented in Section 7.0 and Appendix II, indicate similar findings. Therefore, the most dangerous of the WIO resonant events should be adequately modeled with the aeroelastically-coupled discrete frequency approach. However, it is acknowledged that the dynamic response at off-resonant conditions will not be accurately predicted and will be un-conservative.

4.2.4.3 Aeroelastically-Coupled Turbulence-Coupled Approach

Within the aeroelastically-coupled turbulence-coupled approach, the unsteady drag forces are calculated in the same manner as the aeroelastically-coupled discrete frequency approach. The unsteady lift equations; however, are considerably more complicated. The equations used for this approach are based upon the relations shown in ESDU (ref. 3). In ESDU, the magnitude of the lift forces are presented as RMS (root mean square) values and the frequencies are shown as power spectral density (PSD) distributions which are dependent upon turbulence intensity and structural motion. Therefore, the fluctuating lift forces are defined in the frequency domain with an RMS magnitude. Once defined, the lift forces are calculated in the proposed analytical method by conversion into the time-domain with the use of a Fourier series with random phasing. Proper conversion of the lift force is verified by comparing the PSD of the time history with the "as defined" lift force in the frequency domain. Proper magnitude is also confirmed by comparing the RMS value of the force time history with the RMS values presented by ESDU. It is beyond the scope of this thesis to explain or demonstrate the validity of the equations used in this section. ESDU is a comprehensive report that presents these equations and supports them with references of wind tunnel data. Additionally, ESDU does not distinguish between the RMS of the lift coefficient with smooth flow, and the RMS of the lift coefficient with turbulent flow for sections of the report not dealing specifically with turbulence. In this thesis, however, the turbulent and smooth flow lift coefficient RMS is always distinguished based upon the author's understanding of ESDU.

For this approach, turbulence intensity is represented in an unusual manner of an along-wind component of turbulence (I_u). I_u is a ratio of the standard deviation

(sigma) of wind velocity due to turbulence over the mean wind speed. For wind tunnel flows, a value of 0.003 to 0.02 is considered representative. For light turbulence atmospheric flow, (or perhaps in the presence of structural wake in a wind tunnel), a value of 0.08 to 0.12 is considered representative. For turbulent and windy atmospheric flow, a value of 0.20 is considered representative. This high turbulent value of 0.20 was determined with the use of NASA-HDBK-1001 (ref. 1), were the 3-sigma wind gust applied to a 31 knot wind creates a peak wind speed of approximately 47 knots.

The turbulence intensity determines the bandwidth parameter (δ_B) of fluctuating lift as shown in equation 27 taken from ESDU (ref. 3).

$$\delta_B = 0.45 - 0.43\exp\left(-118 I_u{}^{2.8}\right) \qquad (27)$$

The bandwidth parameter is used to define a "target" normalized PSD distribution of the rigid lift force coefficient (C_{Lr}) as shown in equation 28 taken from ESDU.

$$\frac{f\, S_{C_{Lr}}}{\widetilde{C}_{LoT}{}^2} = \frac{4\delta_B\left(f/f_{VS}\right)}{\pi}\left[\frac{1}{\left[1-\left(\frac{f}{f_{VS}}\right)^2\right]^2 + \left(2\delta_B\frac{f}{f_{VS}}\right)^2}\right] \qquad (28)$$

Where,
f = frequency (Hz)
f_{VS} = frequency of vortex shedding (Hz) = $\Omega_L / 2\pi$
S_{CLr} = power spectral density of the lift coefficient for a rigid structure
$\widetilde{C}_{LoT}$ = lift coefficient RMS of rigid structure with turbulence content

Curves of the normalized spectral density of C_{Lr} for various values of turbulence intensity are shown in figure 12 as a function of f/f_{VS}.

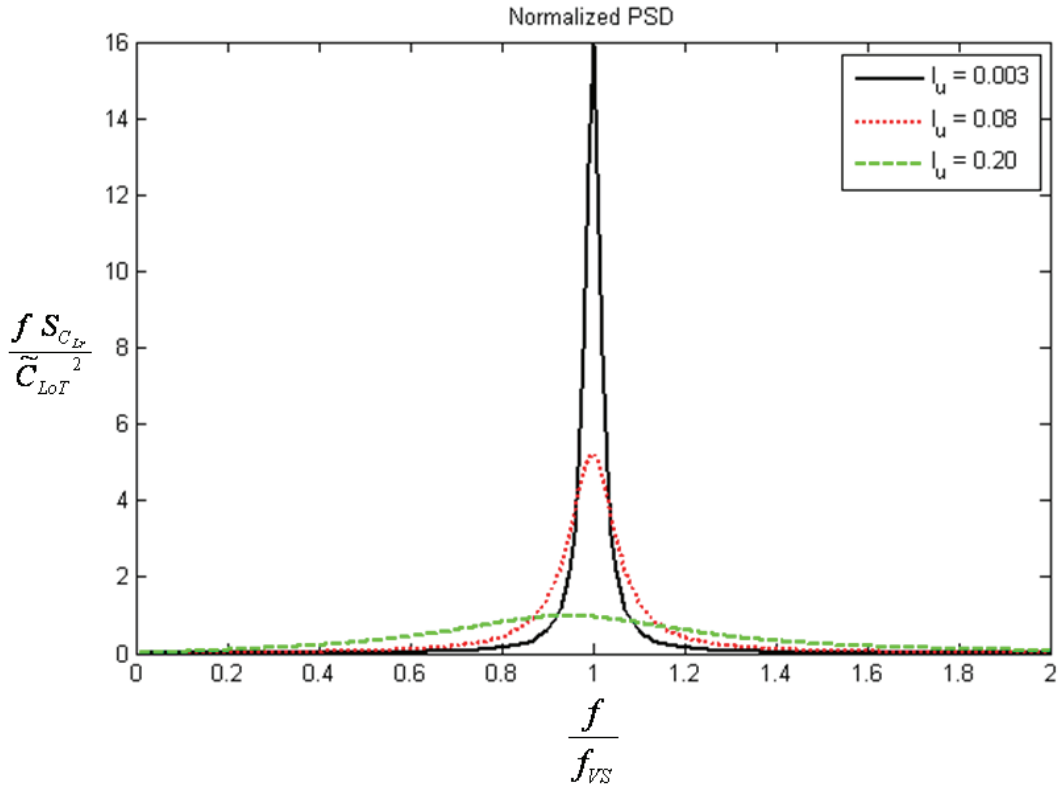

Figure 12. Normalized Spectral Density of Lift Coefficient with Various Values of Turbulence Intensity.

To convert the result of equation 28 (plotted in figure 12) into a form that can be used to calculate lift, one needs to find the lift coefficient RMS of the rigid structure with turbulence content ($\tilde{C}_{LoT}$). This is determined by equations 29 through 32 taken from ESDU (ref. 3). For these equations, one needs to select a smooth-flow, rigid-structure lift coefficient RMS ($\tilde{C}_{Lo}$), which is dependent upon Reynolds number and surface roughness. For subcritical Reynolds numbers, a value of 0.5 is recommended. For transcritical, and upper-transcritical Reynolds numbers, a value of 0.07 is recommended. For smooth surfaces in supercritical Reynolds numbers, a value of 0.07 is recommended. For surfaces with some roughness (roughness height to diameter ratio of 0.0001) in supercritical Reynolds numbers, a value of 0.10 is recommended. Refer to Section 1.4 for a definition of the critical regimes of vortex shedding. For most large full-scale launch vehicles of nearly cylindrical cross-section, a value of 0.10 is considered representative.

$$f_{ns} = \sqrt{\frac{2.38\left({}^{x}L_u/D\right)^{5/3}}{1+2.83\left({}^{x}L_u/D\right)^{5/6}}} \qquad (29)$$

$$Tu = I_u\left({}^{x}L_u/D\right)^{-1/3}\delta_B{}^{1/2} f_{ns} \qquad (30)$$

$$f_{turb} = 2.15\left[1-\exp\left(-53\,Tu^{1.05}\right)\right] \qquad (31)$$

$$\widetilde{C}_{LoT} = \sqrt{f_{turb}{}^2\widetilde{C}_{Lo}{}^2 + \widetilde{C}_{Lo}{}^2} \qquad (32)$$

where,

${}^{x}L_u/D$ is the longitudinal integral length scale of along wind component of turbulence divided by the section diameter. For model scale predictions in the analytical method, this value was set to (3/0.8). A representative full-scale value would be on the order of 100/D, where D is in ft.

f_{ns}, T_u, and f_{turb} are interim values defined in ESDU (ref. 3) as shown in equations 29 through 31

Fortunately, equations 29 to 32 are not sensitive to changes in ${}^{x}L_u/D$ which is difficult to define. An order of magnitude change is required before a significant difference is noted in the spectral density. ESDU also suggests that the f_{ns} term can be neglected entirely (f_{ns} = 1) in equation 30 for full-scale calculations.

It is noted here that no consideration is given to modeling the spectral distribution of turbulence in the atmosphere. It is assumed that the equations presented in ESDU adequately capture the important relationships between turbulence and WIO. When considering the independent effect of turbulence (as done by the aeroelastically-coupled discrete frequency approach) or when attempting to model the gust and turbulence effect in drag, one should consider the spectral distribution as outlined by Houbolt, Steiner, and Pratt (ref. 23) and von Kármán (ref. 24).

The PSD distribution of the rigid fluctuating lift coefficient, with turbulence content, can be determined by equation 33 as a function of *f*. The result of this dimensional PSD distribution is plotted in figure 13 for f_{VS} = 1.2 Hz, and $\widetilde{C}_{Lo}$ = 0.10.

$$S_{C_{Lr}} = \frac{\widetilde{C}_{LoT}{}^{2}}{f} \frac{4\delta_B \left(f / f_{VS} \right)}{\pi} \left[\frac{1}{\left[1 - \left(\frac{f}{f_{VS}} \right)^2 \right]^2 + \left(2\delta_B \frac{f}{f_{VS}} \right)^2} \right] \quad (33)$$

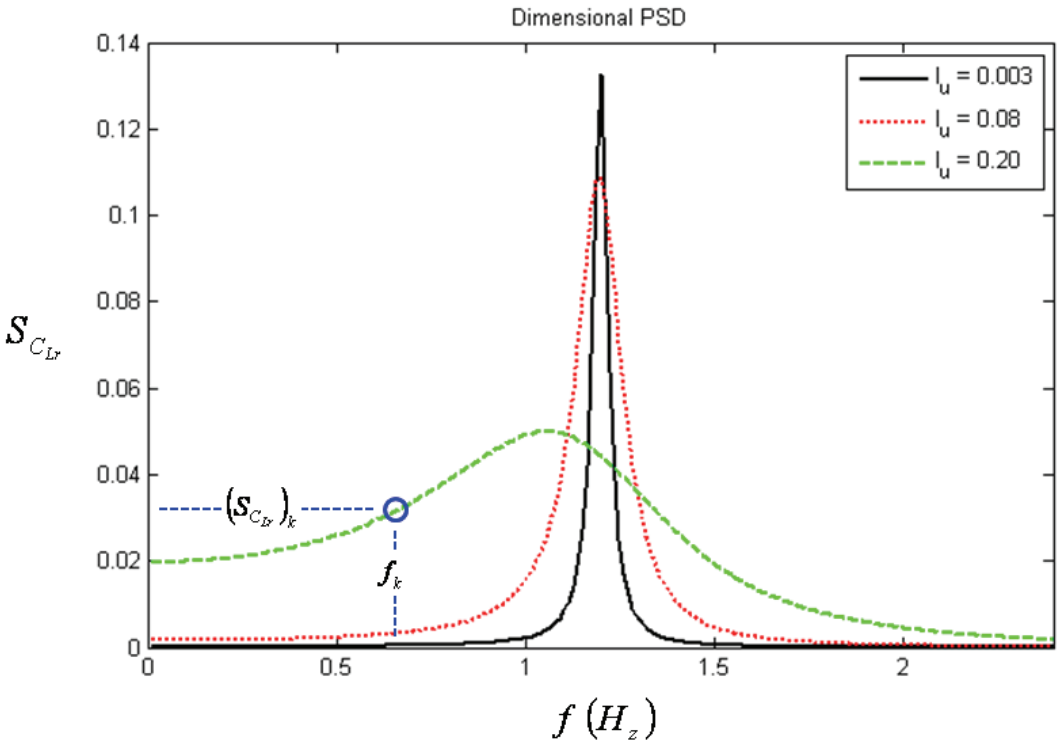

Figure 13. Spectral Density of the Rigid Lift Coefficient with Various Values of Turbulence Intensity, f_{VS} = 1.2.

Structural motion also has an impact on the fluctuating lift coefficient RMS. Within ESDU, a series of equations is provided to determine the motion component of oscillating lift RMS that is in-phase with the structural motion. This in-phase component ($\widetilde{C}_{Lm}$) is calculated as shown in equations 34 through 37.

$$n_k = 1.5 - 0.2 \exp\left(-100 \widetilde{C}_{LoT}{}^{3} \right) \quad (34)$$

$$c = 34 \widetilde{C}_{LoT}{}^{n_k - 1} \quad (35)$$

$$b = 0.45 \left\{ 1 - \exp\left[-0.00033 \left(H / D \right)^{3.25} \right] \right\} \quad (36)$$

$$\widetilde{C}_{Lm} = \frac{b\widetilde{C}_{LoT}\left[\exp\left(c\,{}^{a}\!/_{D}\right)-1\right]}{b+\widetilde{C}_{LoT}\left[\exp\left(c\,{}^{a}\!/_{D}\right)-1\right]}\left[1+\left({}^{a}\!/_{D}\right)\frac{1-\exp\left(3\,{}^{a}\!/_{D}\right)}{1+\exp\left(3\,{}^{a}\!/_{D}\right)}\right] \qquad (37)$$

where,
H/D = fineness (height to diameter) ratio
a/D = sectional amplitude (due to structural motion) to diameter ratio
n_k, *c,* and *b* are interim values defined in ESDU (ref. 3) as shown in equations 34 through 36

With the definition of S_{CLr} (eqn. 33) and $\widetilde{C}_{Lm}$ (eqn. 37), the necessary information is defined in order to calculate the sectional unsteady lift for any given value of the bandwidth parameter (δ_B) and vortex shedding frequency (f_{VS}). To convert the frequency domain definition of S_{CLr} into the time domain, S_{CLr} is digitized into 198 parts (k = 1 to 198) with an explicitly defined value of $S_{CLr}(k)$ and $f(k)$ for each part. A Fourier series, with 198 different frequencies, is then used to convert the PSD distribution into a time-domain sectional lift force that accounts for vortex shedding and turbulence. The effect of structural motion upon the unsteady lift equations is then accounted for by the inclusion of $\widetilde{C}_{Lm}$, as defined from equation 37. Therefore, the time-domain equation for the unsteady lift force that accounts for the combined effects of vortex shedding, turbulence and motion is represented in equation 38. When reviewing this equation, recall that $\widetilde{C}_{Lm}$ contains only the component in-phase with motion. Additionally, the peak value of a discrete frequency function is a factor of $\sqrt{2}$ larger than the RMS. Therefore, the contribution due to motion is added as a discrete frequency forcing function at the vortex shedding frequency (with a magnitude increase factor of $\sqrt{2}$) for the particular vehicle section. Adding the motion component in this manner is validated with equation 39 from ESDU which calculates the overall lift force RMS that includes vortex shedding, turbulence, and motion.

In equation 38, ϕ_k is a randomly determined phase (ranging from 0 to 2π) for the forcing function at a frequency of f_k. Also, by definition of S_{CLr} and the number of digitized parts, the vortex shedding frequency, magnitude, and phase corresponds to k=99. Therefore $f_{k=99} = f_{VS}$. The values in equation 39 are only used to verify the magnitude of the time-history lift force, and are not used in the equations of motion in the analytical method. In equation 39, "*fr"* is a knock-down factor that suppresses the rigid contribution of $\widetilde{C}_L$ as defined by ESDU (ref. 3).

$$Lift_{vortex+turbulence} = \frac{1}{2}\rho U^2 D\,dx[\ \sqrt{2}\ \widetilde{C}_{Lm}\sin\left(2\pi f_{VS}t + \phi_{99}\right) + \ldots \sum_{k=1}^{198} A\sqrt{f_k\left(S_{C_{Lr}}\right)_k}\sin\left(2\pi f_k t + \phi_k\right)] \quad (38)$$

where,
A = 0.1396
t = time
ϕ = randomly chosen phase for each frequency

$$\widetilde{C}_L = \sqrt{\widetilde{C}_{Lm}{}^2 + \left(fr\cdot\widetilde{C}_{LoT}\right)^2}$$

where,

$$fr = \frac{2}{1+\exp\left(18\widetilde{C}_{LoT}\left(a/D\right)^2\right)} \quad (39)$$

To verify a proper time-domain conversion of the lift coefficient, as attempted by equation 38, one can take the PSD of the time-history signal (for no-motion) and compare with the target PSD distribution of the rigid lift coefficient. Figure 14 is a comparison of the target PSD distributions of the fluctuating rigid lift coefficient as defined by equation 33, and the PSDs of the time history lift force created by equation 38 with no motion, in coefficient form (i.e. equation 38 divided by $\frac{1}{2}\rho U^2 D\,dx$). For the curves in figure 14, the turbulence intensities are 0.003, 0.08, and 0.20, and the a/D ratio is 0.00 ($\widetilde{C}_{Lm}$ = 0). By comparison of the target value PSD distributions with the PSD of the time histories, one can see that equation 38 adequately represents the desired magnitude and frequency content of lift when $\widetilde{C}_{Lm}$ = 0.

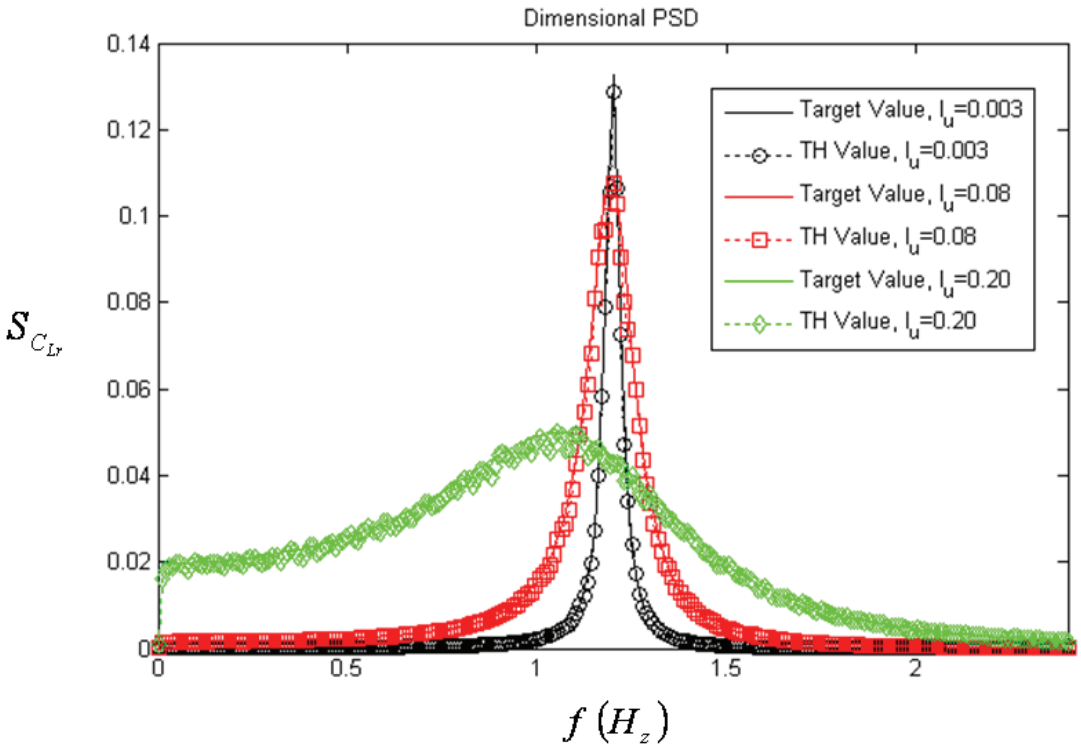

Figure 14. Power Spectral Density of Lift Coefficient, Target Values Compared to PSD of Time-History Values, No Structural Motion.

Similarly, figure 15 contains the PSD quantities of the time history lift coefficient for an a/D ratio of 0.05 where $\widetilde{C}_{Lm}$ is nonzero. This a/D ratio corresponds to a condition of significant structural motion for the Ares I-X and the effect of this motion on the PSD of the lift coefficient is significant.

To verify proper lift coefficient magnitude due to motion, the RMS values of the lift coefficient time history can be compared to direct calculation by equation 39. More explicitly, does $RMS\left(Lift_{vortex+turbulence} \Big/ \tfrac{1}{2}\rho U^2 D\,dx \right) = \widetilde{C}_L$. The RMS values of the lift coefficient time histories (generated with equation 38) for an a/D ratio of 0.05 are: 0.163, 0.235, and 0.311 for turbulence intensities of 0.003, 0.08, and 0.20 respectively. For comparison, the lift coefficient RMS values calculated directly from equation 39 are 0.139, 0.213, and 0.302 for turbulence intensities of 0.003, 0.08, and 0.20 respectively.

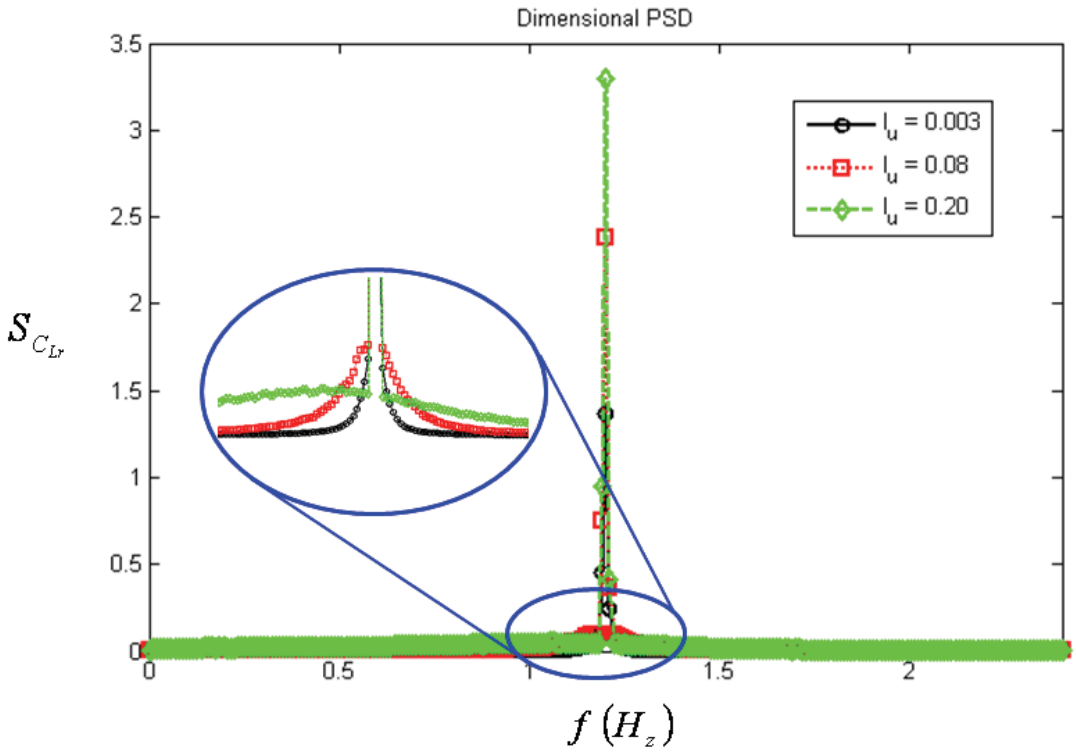

Figure 15. PSD of Time-Domain Values of Lift Coefficient, With Significant Structural Motion

Jones, Cincotta, and Walker (ref. 25) present results for the effect of motion on lift force PSD distributions for high Reynolds numbers that are similar in magnitude to that shown for low turbulence (I_u = 0.003*)* presented in figures 14 and 15. Jones et al. acquired data for a two dimensional cylinder with low turbulence (wind tunnel inherent turbulence) for rigid and forced oscillations with varying amplitudes and frequencies at high Reynolds numbers. An example is presented in figure 16 as the PSD of the lift coefficient for a rigid cylinder and a cylinder with a forced a/D ratio of 0.0278. Jones, Cincotta and Walker use the term h_o/D as the amplitude ratio in lieu of a/D used in this thesis, and Φ_{CL} as the PSD of the lift coefficient, in lieu of S_{CLr} used in this thesis. Jones et al. also emphasize that Φ_{CL} is a function of fD/V *(reduced frequency)* by the annotation Φ_{CL}(fD/V) in the graphs shown in figure 16, where the value of f_{VS} = 10.5 Hz. Therefore, the x-axis and y-axis values of the PSD in figure 16 are not consistent with this thesis, however, the RMS values are.

Jones, Cincotta, and Walker (ref. 25) show a greater sensitivity to motion with a more rapid increase in lift coefficient due to structural motion, than the equations used in this thesis. The lift coefficient RMS for an a/D ratio of 0.0278 from Jones et al. is similar in magnitude to an a/D ratio of 0.05 from the proposed analytical method. Jones et al. also show a slightly lower rigid lift coefficient RMS than

used by this thesis. The reader is reminded that the curve fits used in this thesis were generated with multiple data sets (including Jones et al.) at multiple Reynolds numbers and multiple amplitude ratios. One might obtain a better expression to represent the change in lift coefficient due to low amplitude structural motion at high Reynolds numbers by detailed study of the data contained in Jones, Cincotta, and Walker.

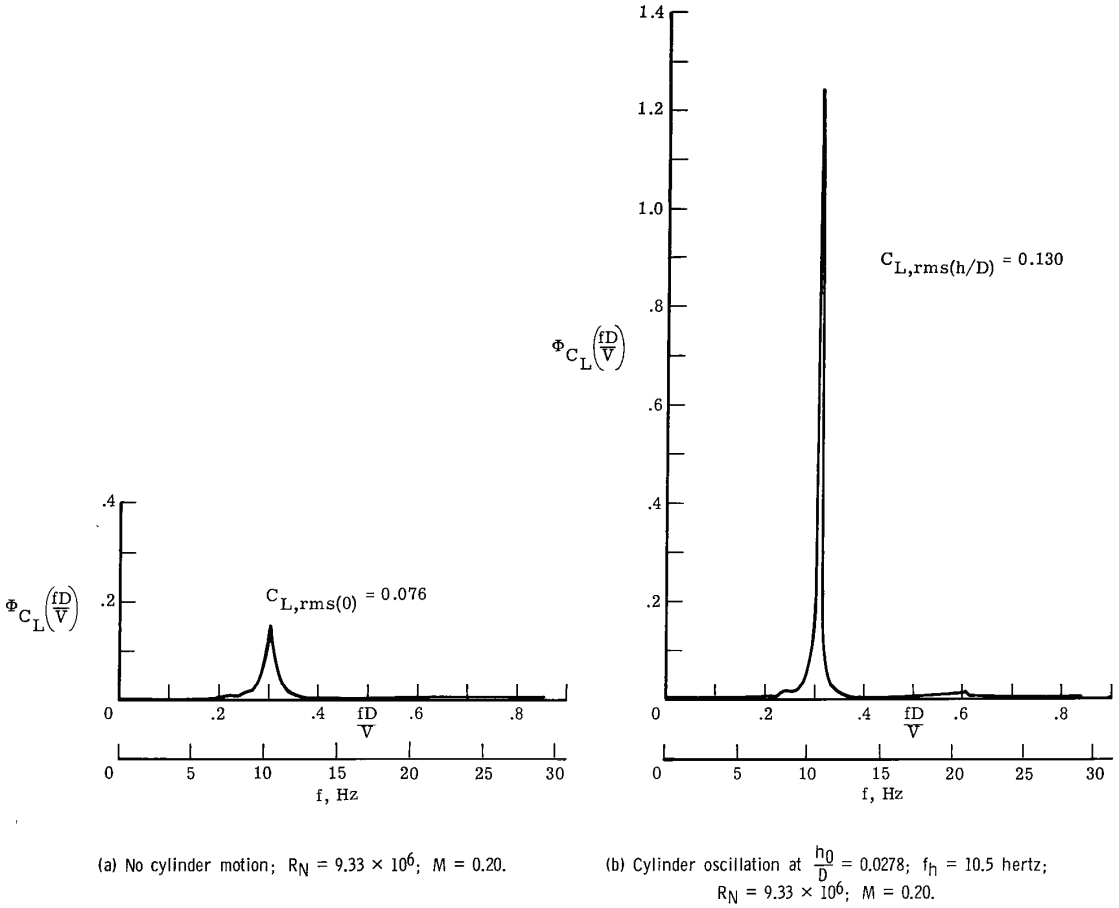

Figure 16. Effect of Amplitude on Lift Force Power Spectral Density.
(used with permission from Jones et al., ref 25)

4.2.5 Extraction of Bending Moment Loads

Depending upon the detail in which the structure of the launch vehicle is known or the availability and detail of an existing FEM, there are three techniques to extract bending moment loads from the time-history deflection outputted from the proposed analytical method.

The first technique is to determine the bending moment loads from the second derivative of the mode shape in accordance with equation 40 (ref. 26). This

method allows an estimate of the loads along the length of the vehicle. However, it is most likely the least accurate. In theory, this method should be exact since the equations of motion and associated mode shapes contain a complete structural representation. However, in order to calculate the second derivative of the mode shape (eqn. 40), one needs to represent the mode shape as an equation. In practice, the mode shape equations are often only estimates that adequately capture the displacement of the structure but not necessarily the curvature. If great care is taken to produce mode shape equations, considering perhaps the use of cubic splines through node displacements, the resulting curvature and corresponding bending moment calculations should be considerably more accurate.

$$Moment = EI \frac{d^2 v}{dx^2} \qquad (40)$$

The second technique involves the use of single point constraint (SPC) loads. SPC loads are easy to output from NASTRAN or similar FEM analyses and are presented as the reaction forces and moments from the point of constraint for each mass-normalized mode shape. The constraint forces and moments (typically a base bending moment for a cantilever-mounted launch vehicle), and associated mass-normalized mode shape deflections can be used to convert the time-history deflections from the analytical method into time-history constraint (vehicle base) loads. This may be more accurate than estimating the loads by determining the curve of the mode shapes and is easy to implement; however, it only provides loads for the vehicle constraint point.

The third and most accurate technique is a detailed conversion of the deflection results into loads by FEM analysis. An FEM can be used to derive the distributed loads associated with each mode shape or individual component loads for critically loaded structural components. The magnitude of modal deflection output from the analytical method can then be scaled to distributed loads along the length of the vehicle. This technique, however, requires detailed FEM analysis independent of the equations shown in the proposed analytical method. Fortunately, once the distributed loads for a given modal deflection are determined for each mode, one can use the results for any output from the proposed analytical method.

When the vehicle (or model) is constructed, the ground vibration test will often reveal that the actual structural frequencies are different than what was anticipated by analysis. When this occurs, it is advisable to adjust the frequencies within the current analytical method in order to provide a better prediction of the resonant WIO velocities. However, this will also alter the equations of motion regardless of the technique used to extract bending moment loads. In the study of dynamic structures, the stiffness *(EI)* is proportional to the square of the natural frequency *(equation 43 in Section 5.0)*. Also, the load is

proportional to the deflection multiplied by the stiffness *(equation 42 in Section 5.0)*. Therefore, when the natural frequencies are altered in the equations of motion due to the results of experimental vibration tests, then the derived load per unit deflection should also be altered by a factor of the frequency ratio squared. This adjustment of the load to account for different structural stiffness is valid provided that the vehicle mass and mode shapes still adequately match the anticipated values. Otherwise, the required mode shape scale relation, presented in equation 14, will not be met.

5.0 Component Validation and Tests of Proposed Analytical Method

5.1 Representation of Steady Loads

All deflections of the launch vehicle are modeled in the current simulation as a sum of each mode shape for both static and dynamic response. For dynamic response this assumption is easily justified by the method of assumed modes. For the static response, however, the method assumes that the static deflection of a cantilever launch vehicle can be closely represented by the deflection of the fundamental mode in the respective axis.

In an effort to validate the output of the current analysis with textbook results, a study was done with a simplified cylindrical geometry assuming a constant mass distribution and stiffness. Calculated deflections under steady load were compared to textbook deflections of uniform beams under uniform load (ref. 11 and 26).

For velocities significantly away from the resonant condition, the drag load on a uniform cylinder exposed to a uniform flow can be represented as a constant distributed load with a magnitude as calculated in equation 41.

$$Drag_{unit\ length} = \frac{1}{2}\rho U^2 C_d D \qquad (41)$$

Hibbeler (ref. 26) dictates that the known tip deflection of a uniform cantilever beam under a constant distributed load (w) is as shown in equation 42. The value of EI can be estimated (for a uniform beam) by utilizing equation 43 if the frequency of the first bending mode, (ω, rad/s) and the mass distribution (m, slugs/ft) is known (Meirovitch, ref. 11).

$$\text{tip deflection} = \frac{-wL^4}{8EI} \qquad (42)$$

$$\omega_1 = 1.875^2\sqrt{\frac{EI}{mL^4}} \qquad (43)$$

Assuming a constant diameter of 18.05 ft, a C_d of 0.8, and a flow velocity of 50 ft/s, the distributed load can be calculated as 42.9 lbs/ft. If the cylinder length is 310 ft, the mass distribution is 201 slugs/ft, and the first bending frequency is 0.2 Hz (1.257 rad/s), the vehicle bending stiffness (EI) is then 2.372×10^{11} lbs-ft^2. This yields a tip deflection of 0.209 ft.

In order to compare the proposed analytical method to the above calculation, the

same constant diameter, mass distribution, and first mode frequency were entered into the analytical method. Accordingly, new mass-normalized mode shapes were created using the beam equations in Meirovitch (ref. 11). Figure 17 shows the calculated first bending mode shape and the generalized coordinate responses for a velocity of 50 ft/s. After an oscillation from the initial condition, the steady state generalized coordinate response in the drag direction is a value of 26.5. Multiplied by the mass normalized mode shape value of 7.98 x 10^{-3} for the tip, this yields a predicted static tip deflection of 0.211 ft, which compares well with value of 0.209 ft calculated from Hibbeler (ref. 26).

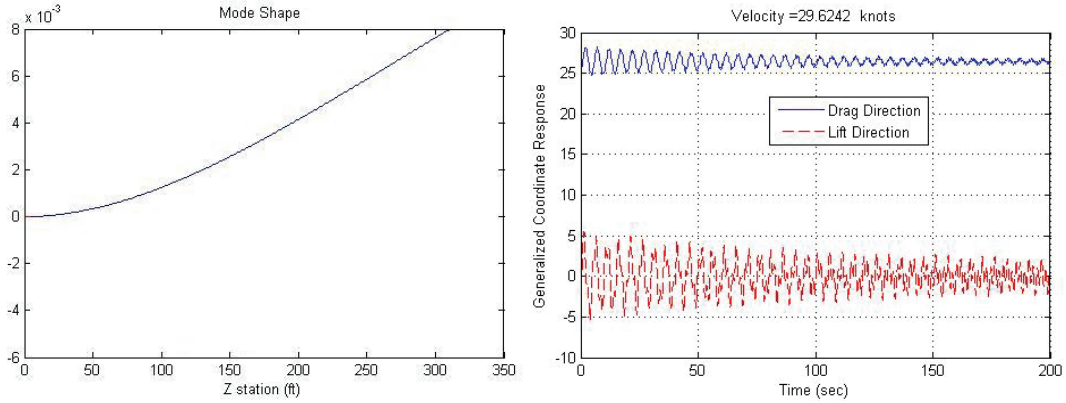

Figure 17. Mass-Normalized Mode Shape and Generalized Coordinate Response for Uniform Cantilever Cylinder.

5.2 Qualitative Comparison of Dynamic Trends

A qualitative comparison was done between the proposed analytical method and wind tunnel data from the Saturn V ground wind loads test acquired by Jones (ref. 27) and Farmer and Jones (ref. 9). Experimental data of the Saturn V bending moments, scaled for full scale values, are plotted as a function of velocity for various damping values in figure 18. The trends in bending moment, illustrated in figure 18, are very close to the displacement trends predicted by the proposed analytical method for the first mode responses of Ares vehicles. For the Saturn V, however, the resonant condition occurs at a much higher velocity (57 knots, equivalent full-scale) as a result of the larger diameter and natural frequencies of the vehicle. Similar to the Ares response predictions presented in this thesis, the Saturn V resonant condition corresponds to a Strouhal number of approximately 0.2.

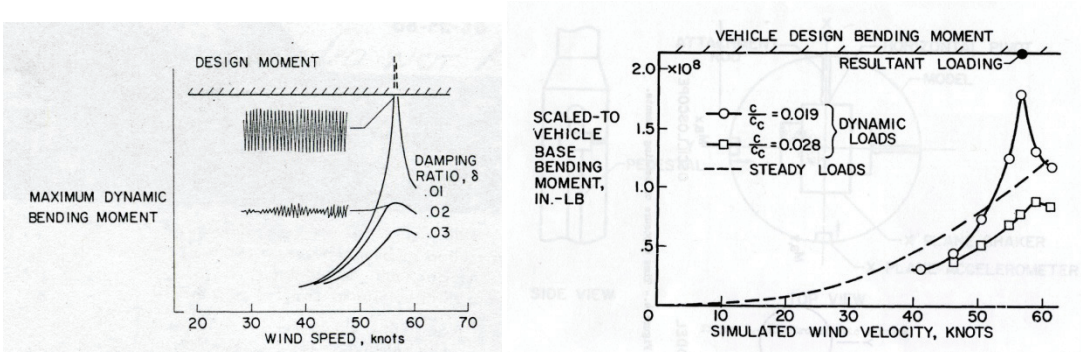

Figure 18. Experimental Data of Peak Response of Saturn V from Wind Tunnel Results.

(used with permission from Farmer and Jones, ref. 9 and Jones, ref. 27)

5.3 Comparison of Steady Bending Moments from Modal Response and Applied Loads

As previously mentioned, bending moment loads can be calculated from the modal displacements by utilizing the Single Point Constraint (SPC) loads output from FEMs. The proposed analytical method was run with a uniform flow and the resulting steady state deflection was multiplied by the SPC load per unit deflection. For comparison, the applied sectional drag loads were multiplied by their respective distance from the base and summed together to determine the applied base bending moment due to steady drag. For the two velocity values examined (100 and 200 ft/s), the SPC displacement-scaled loads yielded results that were about 10% higher than the calculated applied bending moment due to steady drag. It is not expected that these two results should be identical; however, more analysis is required to explain the 10% discrepancy.

6.0 Analytical Results

6.1 General Discussion

As shown in the equations of motion, Section 4.0, there are three levels of complexity (analytical approaches) that were investigated in the current analytical method. Each approach is increasingly complex and capable of modeling more of the results observed during testing. Conservatism usually decreases with increased complexity, except for the effect of turbulence for certain conditions.

In addition to the three different approaches with varying complexity, the proposed analytical method was applied to multiple vehicle concepts. Unless it is otherwise stated, the analytical results shown in this section represent the full-scale Ares I-X vehicle in standard atmospheric air with anticipated full-scale frequency values. For the full-scale analytical simulation, the damping of each mode was chosen as 0.5% of critical in order to produce results believed to be realistic and conservative.

The mass-normalized mode shapes used for the analytical results shown in this section are extracted from FEM results and are similar to those presented in figure 19. The frequencies used for each mode are in the vicinity of 0.2 Hz for the first modes in the η and ζ axes, and in the vicinity of 1.0 Hz for the second modes in the η and ζ axes. Due to the asymmetry of the base of the vehicle associated with the tie-down posts and vehicle attach points, the frequencies and mode shapes differ slightly in the η and ζ axes. This structural asymmetry causes a separation in velocities corresponding to resonant WIO response in the η and ζ axes. Also, the structural response of the vehicle is expected to show more distinct separation in modal vibration compared to a vehicle that has a symmetrical base. The frequencies quoted in this paragraph, and the mode shapes shown in figure 19, do not reflect the actual asymmetry of the launch vehicle nor the actual frequencies and mode shapes in order to protect the sensitive nature of the Ares I-X wind tunnel data.

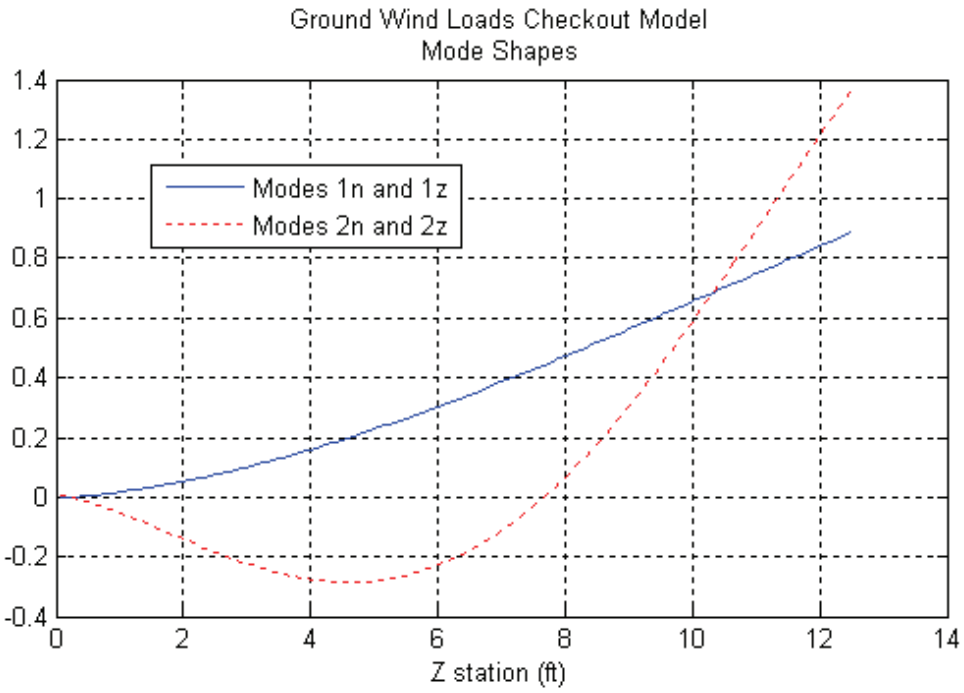

Figure 19. Representative Mode Shapes

Results that refer to a boundary layer profile are for a 3-sigma distribution of wind velocity with altitude as defined in NASA handbook 1001 (ref. 1), and are plotted as a function of velocity at a reference height of 60 feet. The equation for velocity as a function of height (h) above the mean ground plane is shown in equation 44.

$$U = U_{60\,ft}\left(\frac{h}{60}\right)^{1.6\left(0.3048\,U_{60\,ft}\right)^{-0.75}} \qquad (44)$$

where,
$U_{60\,ft}$ = Free stream velocity at a reference height of 60 ft, in ft/s

6.2 Results of Aeroelastically-Coupled Discrete Frequency Approach

The time history and corresponding PSD of the total lift and drag forces summed along the length of the vehicle are shown in figure 20. The reader is reminded that the discrete frequency forcing function is calculated for each vehicle section. The total forcing functions integrated along the length of the vehicle, as shown in figure 20, include a sum of many discrete functions which may or may not be the same frequency for various geometric locations. Therefore, one should not expect the PSD spectra for the total forces summed along the length of the vehicle to be discrete. The results in figure 20 are for a condition with a boundary layer profile and a free stream velocity that is far removed from a

resonant WIO response (velocity = 20 knots).

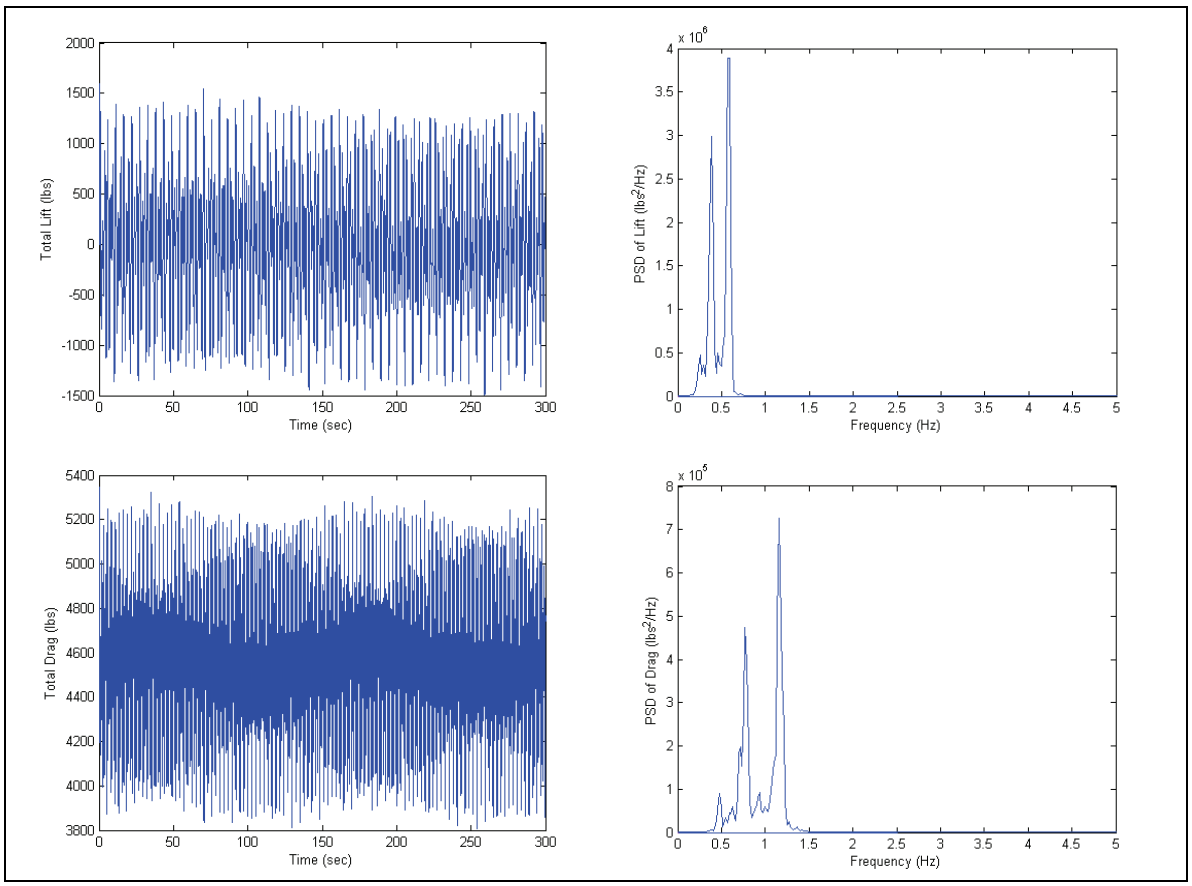

Figure 20. Time History and PSD Result of Total Lift and Drag Forces Acting on the Vehicle. With Boundary Layer Profile, No Resonant Response.

Similarly, figure 21 contains the total lift and drag forces for a condition with a boundary layer profile and a free stream velocity of a resonant WIO response (velocity = 30 knots). One can notice the increase in magnitude of the total lift forces and the change in PSD distribution, both of which should be dependent upon the wind profile and structural motion.

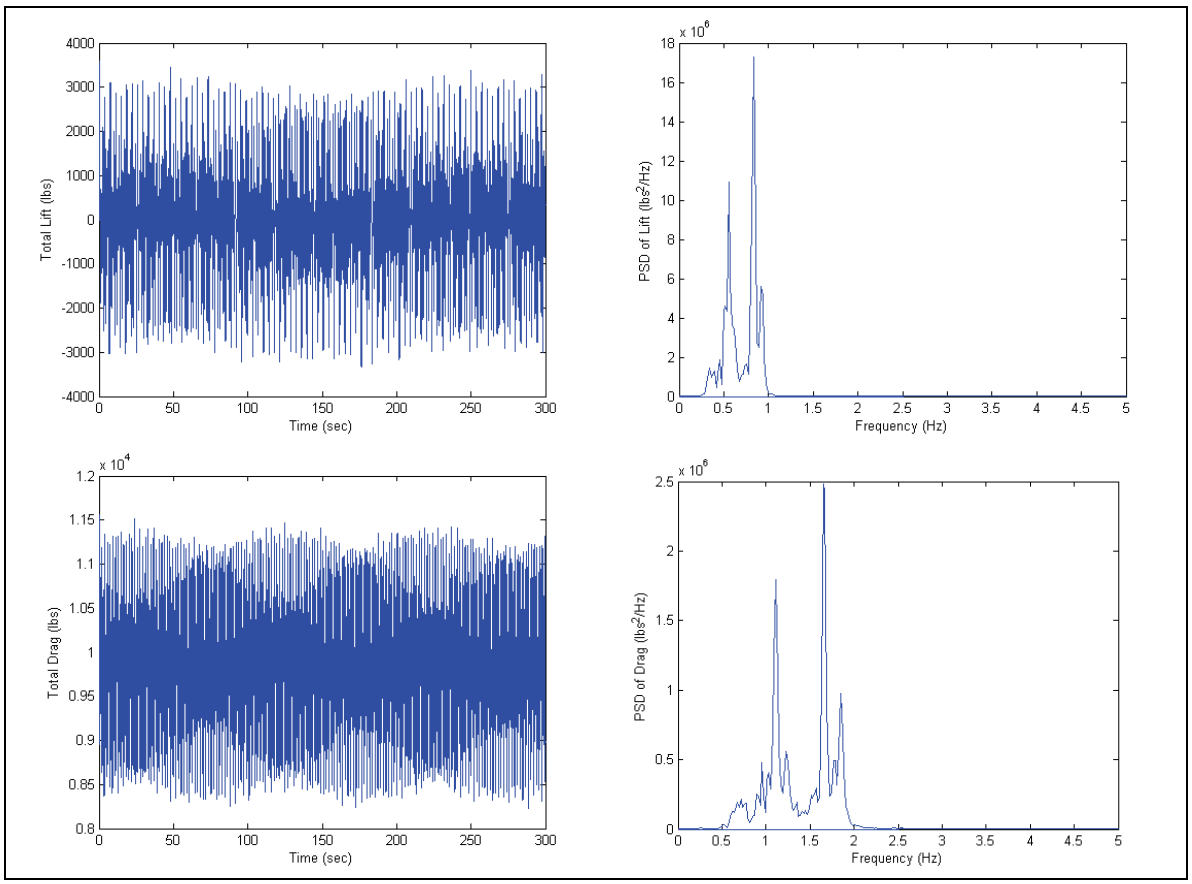

Figure 21. Time History and PSD Result of Total Lift and Drag Forces Acting on the Vehicle. With Boundary Layer Profile, With Resonant WIO Response.

These forces are then converted into generalized forces (Q) as detailed in the equations of motion in Section 4.1. The analytical method was run for the two conditions presented in figures 20 and 21, and the generalized coordinate output was recorded. With the time history of generalized coordinates, one can display the results in many ways. With the use of the mode shape equations, as detailed in Section 4.1, one can derive the dimensional displacement of any portion of the launch vehicle. Figure 22 shows a time history of tip displacement for a condition with a boundary layer profile and a free stream velocity of 20 knots, far removed from a resonant WIO response (the same condition as presented in figure 20).

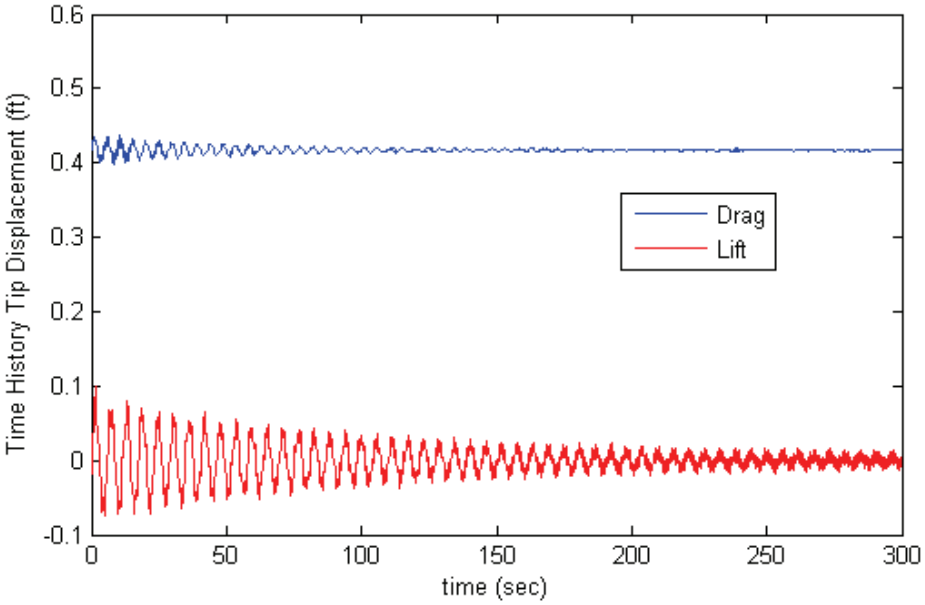

Figure 22. Time History Result of Tip Displacement. With Boundary Layer Profile, No Resonant Response.

Similarly, figure 23 shows a time history of tip displacement for a condition with a boundary layer profile and a free stream velocity of 30 knots; that excites a resonant WIO response with a second bending mode (the same condition as presented in figure 21).

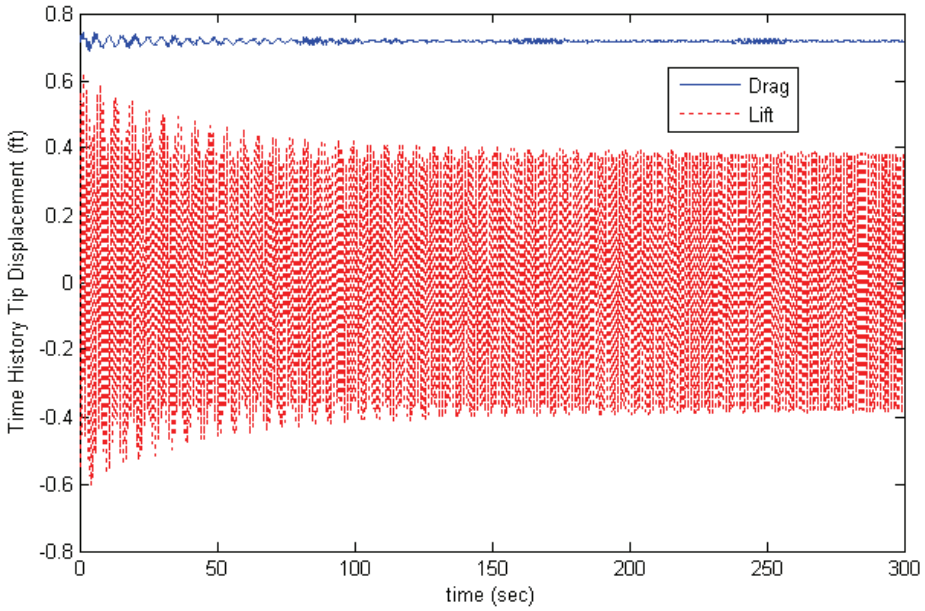

Figure 23. Time History Result of Tip Displacement. With Boundary Layer Profile, With 2nd Mode Resonant WIO Response.

One can also display the results as generalized coordinate time histories for each individual mode shape. Figure 24 shows the time-history generalized coordinate response for the same condition as figures 21 and 23 (at 30 knots). For this condition, θ_{TT} equals 90 degrees, therefore the η axis is normal to the flow and the ζ axis is in-line with the flow.

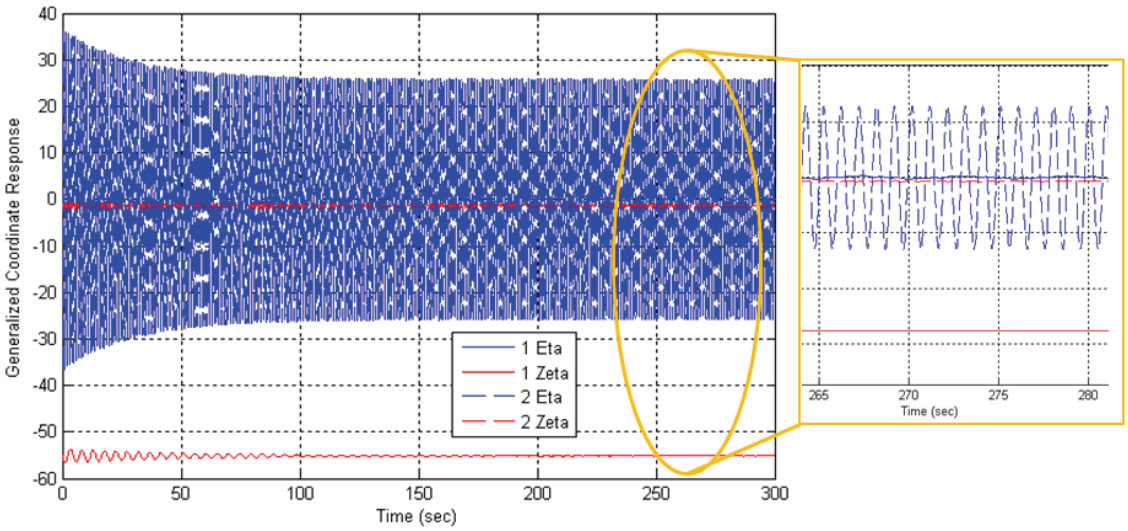

Figure 24. Time History Result of Generalized Coordinates for Each Mode, 2nd Mode Resonant WIO Response.

Most importantly, one can combine the individual modal displacements with FEM results (or other estimations as described in Section 4.2.5) to derive a time history of bending moment. The time-history of base bending moment for each modal contribution is shown in figure 25 for the same condition as that presented in figures 23 and 24. Recall from figure 24 that the vast majority of the tip deflection due to drag is a result of mode 1ζ, and the excitation due to lift is the result of mode 2η. It is important for the reader to notice that the mode 1ζ, aligned with the flow representing drag deflection, has a larger tip displacement than mode 2η *(see figure 23)*. However, mode 2η produces a larger base bending moment, and significantly larger moments at other vehicle sections, than the mode 1ζ even though the physical displacement is less *(see figure 25)*. This increased sensitivity to displacement is a normal feature of higher modes. For the same given tip displacements, the loads associated with higher bending modes are typically much higher and distributed far differently than a fundamental first mode. Therefore, the WIO excitation of a higher mode of vibration is of particular interest and worthy of extra caution.

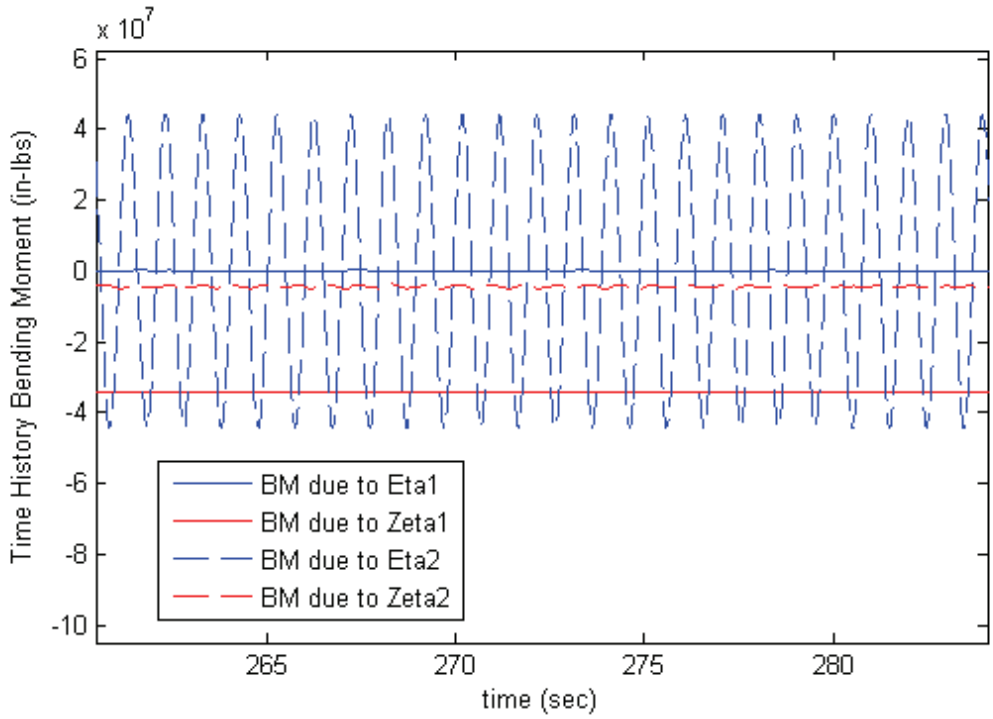

Figure 25. Time History of Base Bending Moment, Contributions of Each Mode.

For each step in time, one can sum the individual modal contributions of bending moment and derive the time history of total bending moment. Using the angle theta, described in the equations of motion in Section 4.1, the resulting bending moment can be displayed in the structural axis or wind axis system. Figure 26 shows the bending moment (of all modes) resolved in the wind axis system thereby yielding a bending moment due to lift and a bending moment due to drag.

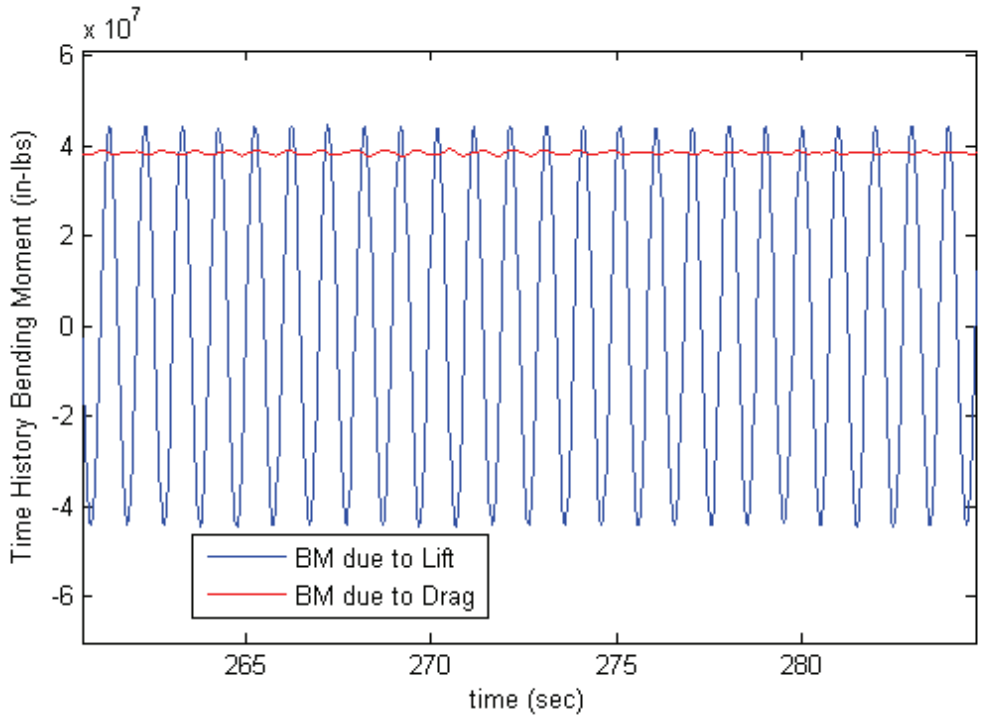

Figure 26. Time History of Base Bending Moment, all Modes Combined, Wind Axis System.

One can record the maximum base bending moment acquired from a time history and investigate the change in maximum base bending moment as a function of velocity. The results shown in figure 26 can then be represented as two points: one at approximately 38×10^6 (in-lbs) representing mean bending moment due to drag, and another at approximately 44×10^6 (in-lbs) representing peak bending moment due to lift. The same iteration described here can be repeated for other velocities and other wind azimuth (θ_{TT}) angles, and the results of peak or mean bending moments can be plotted as a function of velocity for many conditions.

Figure 27 contains the normalized peak (maximum absolute value) base bending moment due to lift and the normalized mean bending moment due to drag as a function of velocity with uniform flow and model-scale properties of the Ares I-X.[2] Included in this figure are the results from two different wind azimuth angles (0 and 90 degrees) which excite different structural modes at different frequencies and lock-on velocities. One can also see that from the results shown in figure 27 that significant dynamic loads are predicted to occur that result from both the first mode responses and the second mode responses.

[2] The bending moment and velocity values have been normalized by arbitrary constants to protect the sensitive nature of the wind tunnel data.

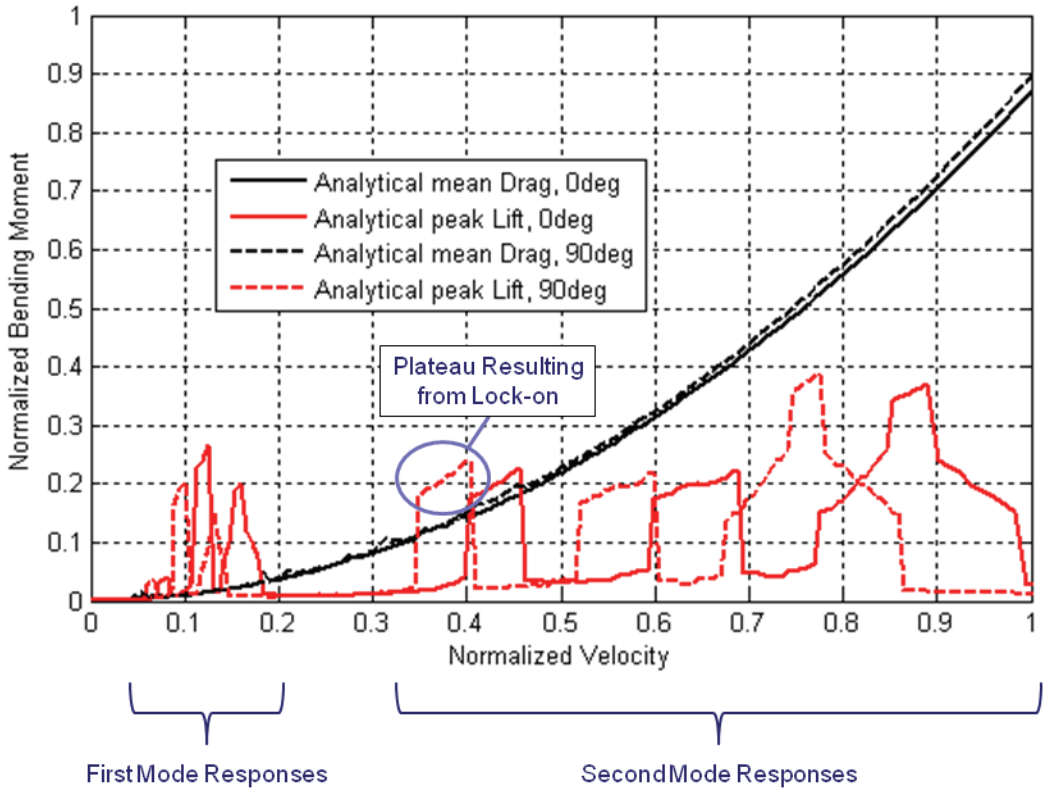

Figure 27. Peak and Mean Base Bending Moment vs. Velocity, Uniform Flow.

Annotated in figure 27 is a characteristic of the simulation of lock-on within the proposed analytical method. As discussed in the equations of motion, when the frequency of vortex shedding is within the range of frequencies where lock-on is expected to occur, the vortex shedding frequency is altered to the appropriate structural frequency. With the proposed analytical method, no adjustments are made to the magnitude of the aerodynamic forcing functions for cases where lock-on occurs and alters the natural vortex shedding frequency. Therefore, a rising "plateau" will be present in the results (for uniform flow) representative of the range of velocities that fix the frequency of vortex shedding to a structural mode. This simulation of lock-on occurs locally and only for the appropriate discrete sections of the vehicle. Therefore, the analytical results with a boundary layer profile are less likely to produce this plateau feature. Shown in figure 28 is the peak base bending moment due to lift and the mean base bending moment due to drag as a function of velocity, at a reference height of 60 feet, with a boundary layer profile and anticipated full-scale vehicle properties (structural damping = 0.5%, all modes).

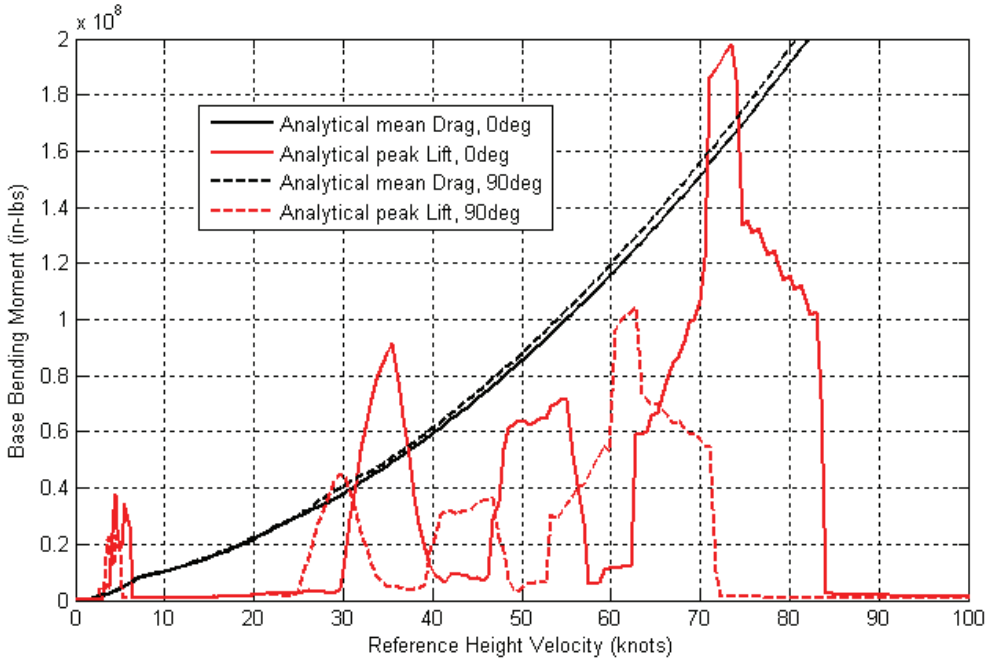

Figure 28. Peak Base Bending Moment vs. Velocity, Boundary Layer Profile.

Another way to view the response for a single velocity and wind-azimuth condition is to plot bending moment in one axis as a function of bending moment in the other. Showing the loads in this manner provides a graphical representation of the vehicle response in two-dimensions and is similar in layout to figure 2, in Section 1.3, which defined the components of base bending moment. Even though such a plot would show bending moment loads, the graphical placement of those loads is analogous and proportional to the displacement of the vehicle in the respective directions. Figure 29 contains a time history trace of base bending moment plotted in the wind axis system with bending moment due to lift plotted as a function of bending moment due to drag.

It is also important to note that the analytical results in figure 29 are for a condition where the approaching wind is offset at an angle of 15 degrees with respect to the vehicle (natural modes) axis system. Even though the lift forcing function is applied in the Z axis, the vehicle responds mostly in the ζ axis because the natural modes (in ζ) respond to the harmonic aerodynamic forcing. This structural response is consistent with the wind tunnel results presented by Ivanco and Keller (ref. 20 and 21). Due to the rotation of the vehicle axes with respect to the free stream flow direction, the dynamic response (and corresponding load) experienced in the vehicle axis system due to lift, will produce large dynamic loads that appear to act in the drag direction. Most importantly, the maximum resultant bending moment load will increase slightly because the distance from the zero load origin to the peak has increased as a result of the axis rotation.

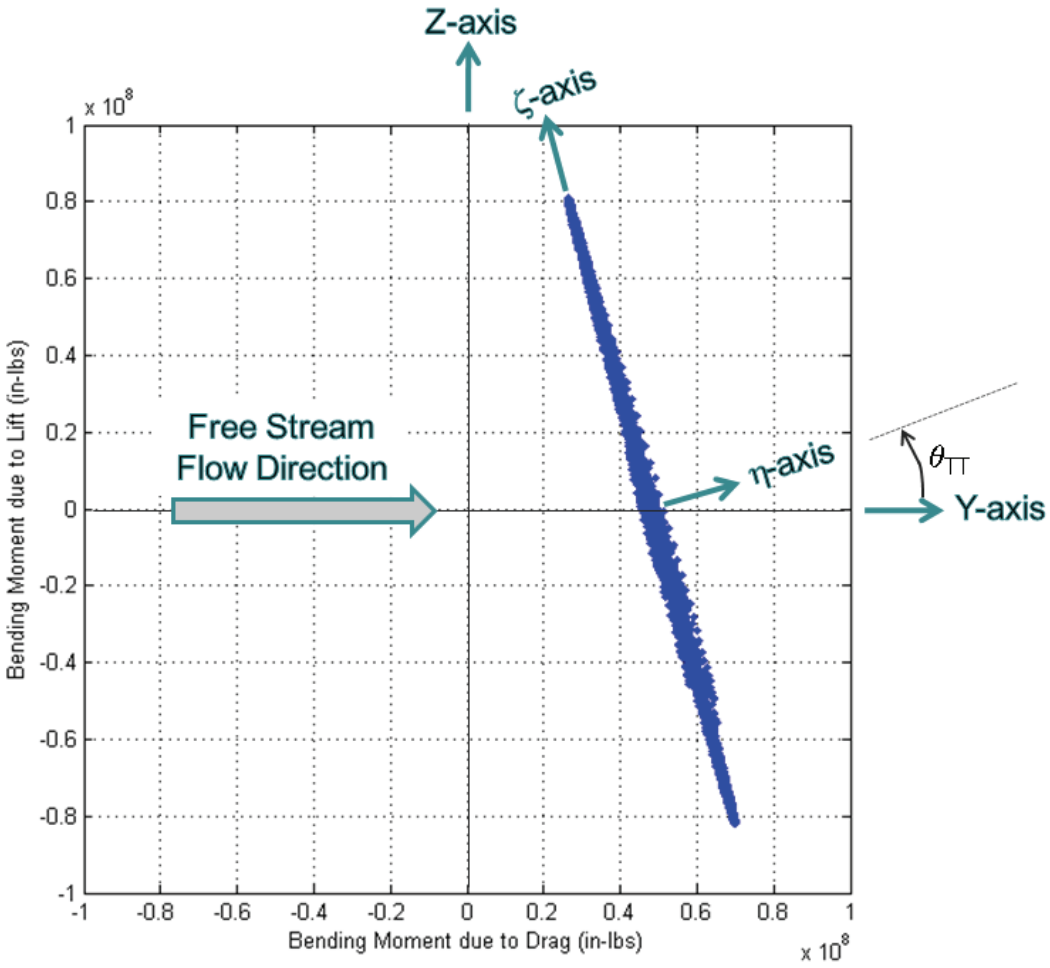

Figure 29. Time History Trace of Bending Moment, Wind Axis System, Free Stream at 15 Degrees to Vehicle Axis System, Velocity = 35 knots.

WIO is an aeroelastically coupled event. Therefore, the amplitude of the dynamic response of the vehicle with respect to a change in structural damping will not scale as systems do with a constant forcing function. For example, a dynamic system with a structural damping of z1, undergoing a dynamic excitation force F will produce a response with a peak amplitude of A1. If this same system has a change in structural damping to z2 with the same excitation force F, the amplitude of the new system, A2, can be determined by equation 45.

$$A2 = A1\sqrt{\frac{z1}{z2}} \qquad (45)$$

However, equation 45 is invalid for aeroelastically-coupled systems where the

forcing function is dependent upon structural motion, and a change in system damping will affect the forcing function F. The aeroelastically-coupled discrete frequency approach was therefore used to evaluate the proposed analytical method's capability to model varying values of structural damping. Figure 30 contains analytical time history results of base bending moment for various values of structural damping. The velocity is fixed (5.5 knots) corresponding to a condition with a large first mode (in ζ) excitation for winds with a boundary layer profile. One can easily observe that the change in dynamic response does not match the relation in equation 45. For example, the result for a structural damping of 0.5% yields a peak amplitude of 33×10^6 (in-lbs), and the result for a structural damping of 1.0% yields a peak amplitude of 18×10^6 (in-lbs).

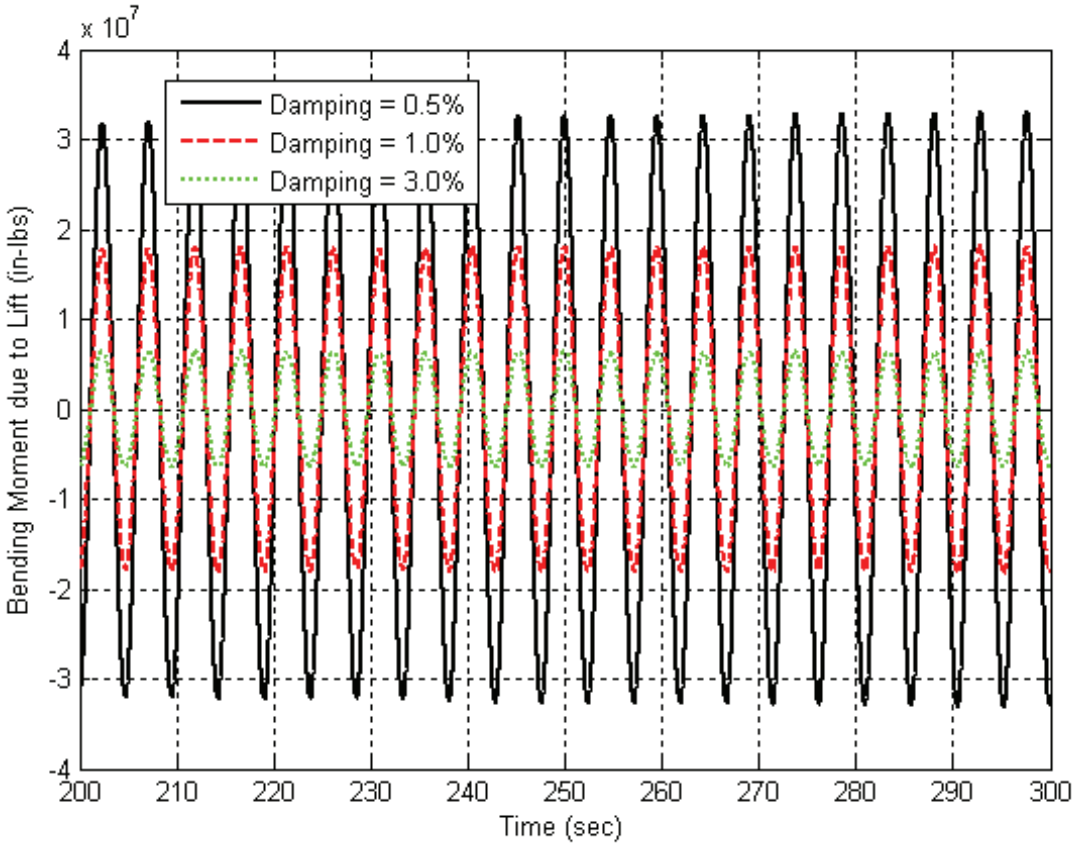

Figure 30. Analytical Base Bending Moment Time Histories for Various Values of Structural Damping. Velocity = 5.5 knots, Mode 1ζ Response. Theta = 0.

The aeroelastically-coupled discrete frequency approach was also used to evaluate various support structure concepts for the` Ares I-X program. Each concept was evaluated by providing the respective mode shape, frequency and expected damping associated with each support concept. Rapid trade studies such as this are a valuable capability of the proposed analytical method. The

results of this trade study are not presented in this thesis.

6.3 Results of Aeroelastically-Coupled Turbulence-Coupled Approach

The aeroelastically-coupled turbulence-coupled approach is computationally intense and fewer conditions were run with the level of detail incorporated in this approach. The PSD distributions of the sectional lift forces, for various levels of turbulence intensity, have already been presented in Section 4.2.4.3. Shown here are the results of this method and the corresponding load predictions for differing values of turbulence intensity. The effect of turbulence on a first mode response is shown in figure 31. The results in figure 31 represent a mode 1ζ resonant WIO response with a structural damping = 0.5% for all modes.

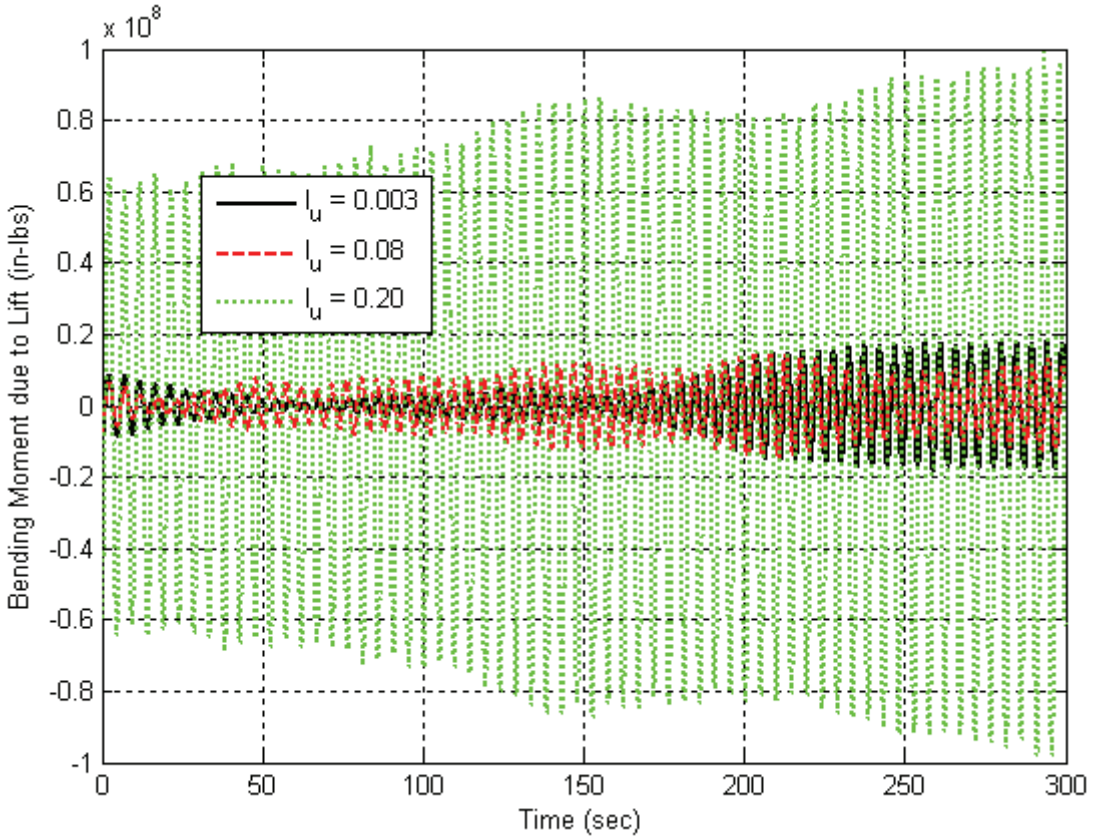

Figure 31. Effect of Turbulence on Mode 1ζ Resonant WIO Response.

Unlike the aeroelastically-coupled discrete frequency approach, the turbulence-coupled approach predicts more variation in the time history amplitude as a result of a widening of the spectral distribution of the forcing function. Additionally, with the inclusion of the random number generator specifying the phase of each Fourier series, multiple runs of an otherwise identical simulation will produce

different results. However, if the time scale is carried to a high enough value, the statistically averaged response should be repeatable and representative. In figure 31, one can observe that the low turbulence prediction (I_u = 0.003) shows a fluctuating load that grows and stabilizes at an amplitude of about 20×10^6 in-lbs. With the inclusion of some turbulence (I_u = 0.08), the peak amplitude is slightly less. It is theorized that this is a result of the reduction in peak PSD magnitude at the resonant frequency. However, with the inclusion of large amounts of turbulence (I_u = 0.20), the peak amplitude increases considerably.

Figure 32 illustrates the effects of turbulence on a mode 2ζ resonant WIO response that occurs at a higher velocity. The inclusion of a small amount of turbulence (I_u = 0.08), increases the second mode response amplitude for parts of the time history and the first mode amplitude for nearly all parts of the time history. The inclusion of large amounts of turbulence (I_u = 0.20), increases the first mode response considerably. The inset to figure 32 contains a portion of the time-history response that allows closer inspection of the frequency content.

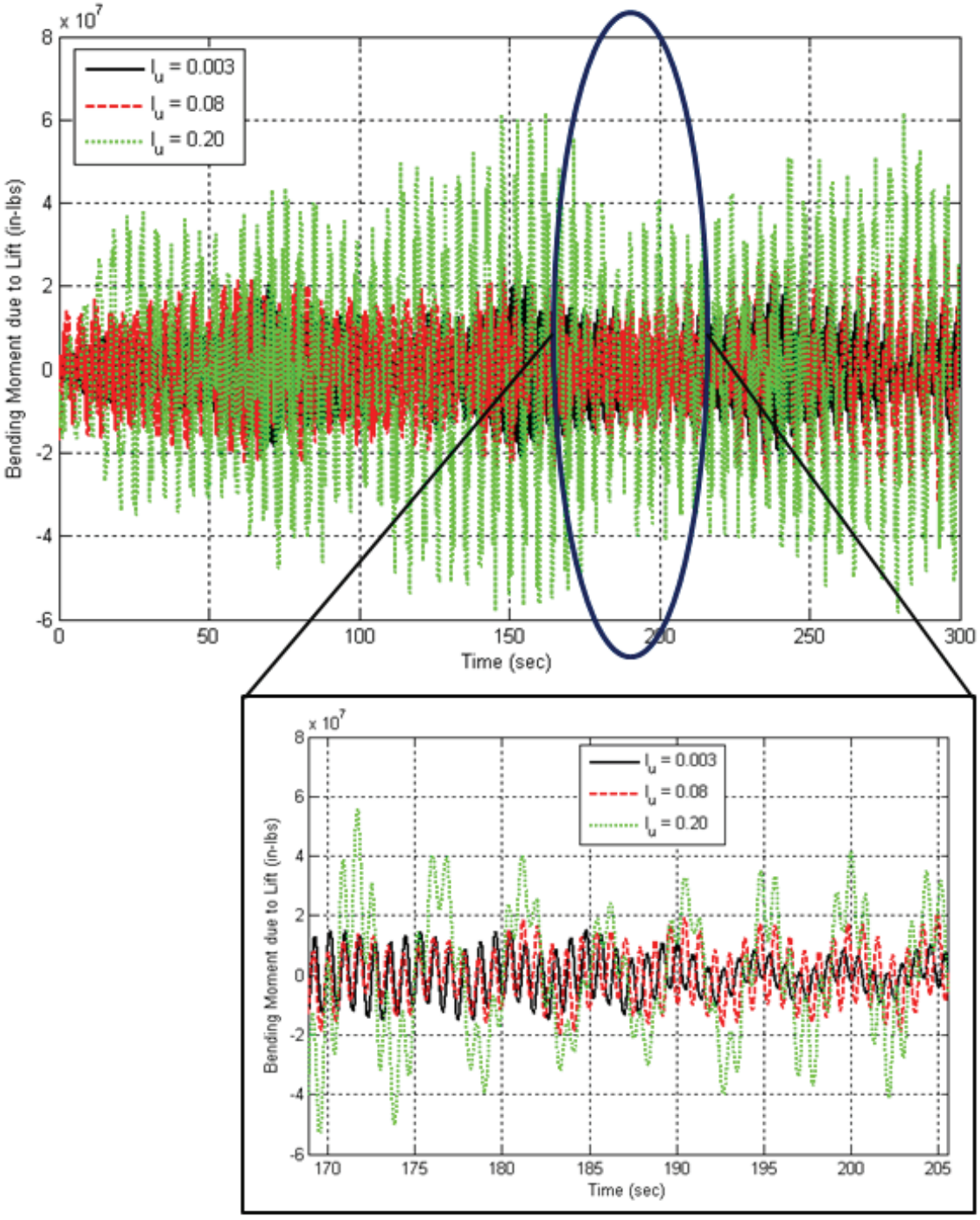

Figure 32. Effect of Turbulence on Mode 2ζ Resonant WIO Response.

A more pronounced effect of turbulence can be observed for velocities far removed from a resonant WIO condition. At these velocities, the frequency of fluctuating lift is not predicted to match that of a structural mode. Therefore, the

majority of the structural response will be due primarily to the turbulence content. It is at conditions such as these where proper modeling of the atmospheric turbulence is critical in determining the peak response of the vehicle. Turbulence modeling becomes especially important for vehicles where the peak design velocity is significantly above any predicted resonant WIO responses. For these cases, proper characterization of turbulence at the higher velocities will be critical in predicting the maximum loads of the full-scale vehicle. Figure 33 shows the effects of turbulence for a condition far removed from a resonant WIO response at a velocity between the predicted first mode and second mode resonant responses (Velocity = approximately 20 knots).

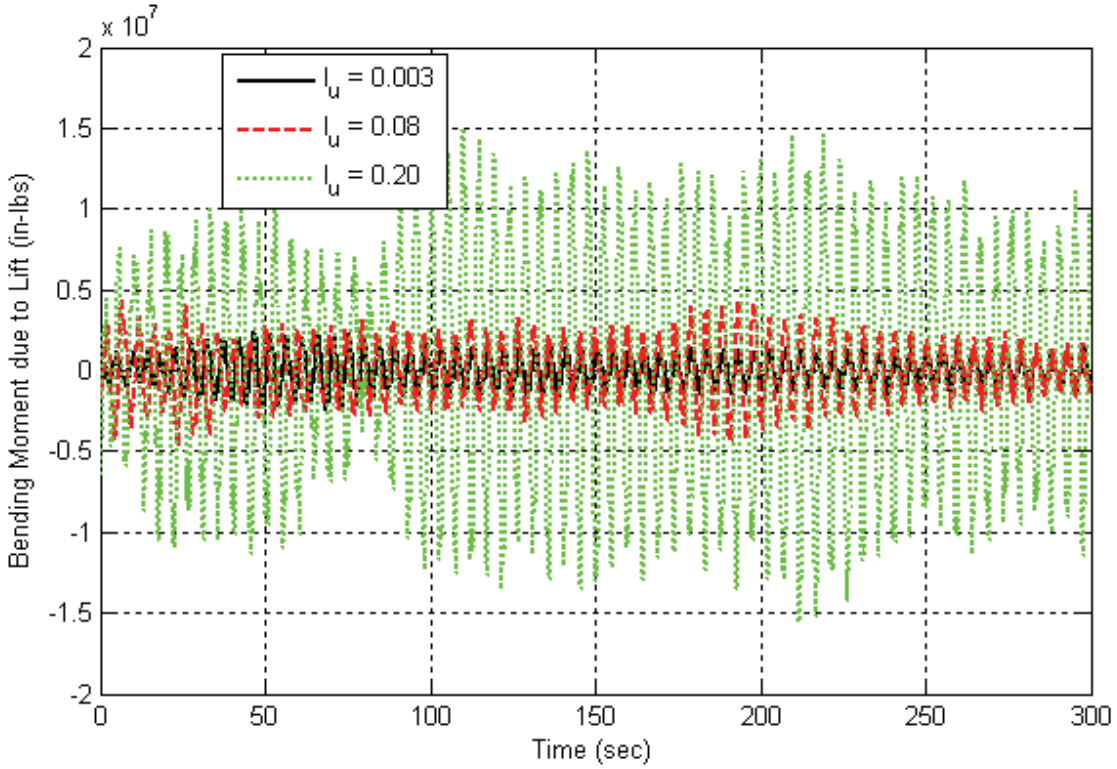

Figure 33. Effect of Turbulence on Vehicle Response, No Resonant WIO Response.

In summary, the addition of turbulence could increase or decrease the WIO response of a vehicle. As shown in the equations of motion, turbulence manifests itself in two ways within the dynamic lift force. First, the frequency bandwidth of the unsteady lift is increased, which also lowers the PSD peak. Second, the RMS value of the lift force is increased. For conditions where large regions of the vehicle are experiencing synchronized shedding at a vehicle natural frequency, the effect of turbulence will most likely decrease the vehicle response. This decreased response can be attributed to the widening of the frequency bandwidth thereby reducing the magnitude of resonant forcing. For

conditions where small regions of the vehicle are experiencing synchronized shedding, the vehicle response may increase. The increase in response can be attributed to an increase in the strength of the lift force, and the widening of the frequency bandwidth which may expand the regions of the vehicle experiencing resonant shedding even though each individual section will have a lower magnitude of resonant forcing.

The results presented in this section predict that turbulence can significantly increase the WIO response of the vehicle for certain conditions. For these conditions, this combined and turbulence-coupled response is expected to be larger than the independent sum of turbulence and WIO response. For all of the comparisons between wind tunnel and full-scale data shown by Foughner and Duncan (ref. 17), and Runyan, Morgan and Mixson (ref. 15), the wind tunnel data was acquired in a low turbulence environment. Figure 33, for example, shows that the addition of turbulence can increase the peak response due to lift by a factor of 6. It is therefore theorized that ignoring the WIO-turbulence coupling produced un-conservative predictions with the use of wind tunnel data and conventional analysis presented by Foughner and Duncan and others.

7.0 Experimental Testing and Data

7.1 Facility and Model Descriptions

7.1.1 Wind Tunnel Facility

Wind tunnel testing was conducted in the NASA Langley Transonic Dynamics Tunnel (TDT) because of the facility's large test section, ground wind loads turntable, and variable pressure capabilities. The TDT is a dedicated aeroelastic test facility designed for high risk dynamic testing and has built-in safety features such as a rapid flow speed reduction capability, observation windows, and a model catch screen. The TDT has a 16 x 16 feet test section and can produce continuous flow speeds from near zero to a Mach number of 1.2 in either air or R134a heavy gas. Total pressure within the tunnel can be varied from a near vacuum to sea level. Maximum Reynolds number is nearly 10 million per foot in heavy gas. LWP-799, (ref. 28) describes the wind tunnel in detail and includes operational envelopes and tunnel characteristics.

7.1.2 GWL Checkout Model

The GWL checkout model was developed in order to regain experience within the Ares I-X team with ground wind loads testing and to verify the operational capability of the wind tunnel facility and associated hardware. Additionally, an objective of the test was to acquire data to validate analytical prediction methods such as the one described in this thesis.

The GWL checkout model was based upon a late 2006 design of the Ares launch vehicle. It is representative of the current Ares I-X design; however, geometric and structural details do not match. Additionally, the diameter was increased by 30% in order to allow for the simultaneous matching of Reynolds number and reduced frequency. As a result of the scaling relationships presented in Section 2.4, the GWL checkout model was aeroelastically-scaled for the first bending modes and the corresponding low velocity range of the full-scale vehicle. However, some data runs conducted in air contained velocities high enough to excite the second bending modes. Reynolds numbers for these air runs were low and the data is considered questionable, however, the magnitude of the dynamic loads for high velocity air runs was comparable to the results of the analytical method. Appendix II contains detailed data of the GWL checkout model test. Figure 34 is a photograph of the GWL checkout model installed in TDT.

Figure 34. GWL Checkout Model installed in TDT.
(Photo Credit: NASA, used with permission)

Due to time and monetary constraints, the GWL checkout model was simple in design and rapidly fabricated. Some of the joints were loose and the inherent damping of the model was higher than desired (greater than 1% of critical for some modes). Higher structural damping will result in lower WIO response with less structural motion. It is expected then that the analytical method may over predict the dynamic response for some conditions.

Strain gages were installed at the base of the model to record base bending moments. However, as a result of instrumentation accuracy issues, the base bending moments were only accurate to approximately 10%. The finite element

model was also rapidly constructed and there is some uncertainty in the mode shapes of the FEM which will affect the accuracy of the analytical method.

The model was nearly symmetrical and no effort was made to replicate the asymmetry that results from the location of the solid rocket booster (SRB) attach points and vehicle hold-down posts. Therefore, there was no significant separation in the first mode frequencies and determination of the fundamental axes of the structure was difficult and dependent upon turntable angle. Structural frequencies and damping also varied with turntable angle as shown in Appendix II. An internal damper was constructed for the checkout model based upon a design conceived for the Apollo program, but it was proven to be ineffective in altering the structural damping.

Surface roughness, protuberances, and Reynolds number were varied throughout testing of the GWL checkout model. This allowed a study of the sensitive parameters with respect to WIO and aided in the assumptions adopted for the proposed analytical method.

7.1.3 Ares I-X GWL Model

The Ares I-X GWL model was meticulously designed and fabricated to accurately represent the mode shapes, frequencies, geometry, and support structures of the Ares I-X vehicle. As a result, the data is sensitive in nature so only normalized values are shown within this thesis and at times details are intentionally lacking. The accuracy of the instrumentation was considerably better than the GWL checkout model, with Ares I-X base bending moment accuracies typically within 1%. Also, the asymmetrical stiffness of the base, resulting from the vehicle attach points and hold down posts, was simulated thereby fixing the fundamental axes of structural vibration. The FEM of the model was also more detailed and greater attention was paid to verify its accuracy with ground vibration testing. This ensures that the mode shapes used within the analytical method are closely matched to the actual mode shapes of the wind tunnel model. Structural damping was also considerably lower than the GWL checkout model, which will yield more structural motion for any given condition. As mentioned in the equations of motion, discussed in Section 4.2.4.2, WIO response magnitude for conditions with significant motion is less dependent upon details of surface roughness, Reynolds number, and flow turbulence. For these conditions, the dominant dynamic forces are primarily associated with sinusoidal vortex shedding loads. It is also theorized that vortex shedding correlation along the longitudinal axis increases with increased structural motion, making the assumptions of the analytical method increasingly valid. Therefore, the proposed analytical method should be more successful in replicating the results obtained by the Ares I-X model rather than the GWL checkout model.

The primary focus of the Ares I-X GWL test was to quantify the WIO response of the second bending modes at higher velocities. As a result of this focus, and the

aeroelastic scaling relationships presented in Section 2.4, low wind velocity and Reynolds number matching of the full-scale vehicle was not possible. Surface roughness was added as described by Szechenyi (ref. 7) to increase the *effective* Reynolds number of the Ares I-X wind tunnel model. All data was acquired with surface roughness added and no smooth configurations were run.

Protuberances were installed based upon the design of the vehicle and no configurations were run without protuberances. Variation of structural damping was made possible with the use of a new damper design developed by the author and described in Appendix I. A small percentage of data was acquired with increased structural damping, and the results confirm that WIO is aeroelastically-coupled and cannot be scaled by equation 45.

Rollout and on-pad configurations were both simulated in the Ares I-X GWL test. For rollout, only the vehicle and mobile launch platform (MLP) were installed in the wind tunnel. For on-pad configurations, applicable tower and service structures were also added to simulate their aerodynamic influence. Figure 35 shows the Ares I-X GWL model in the TDT wind tunnel with the applicable launch pad support structures installed.

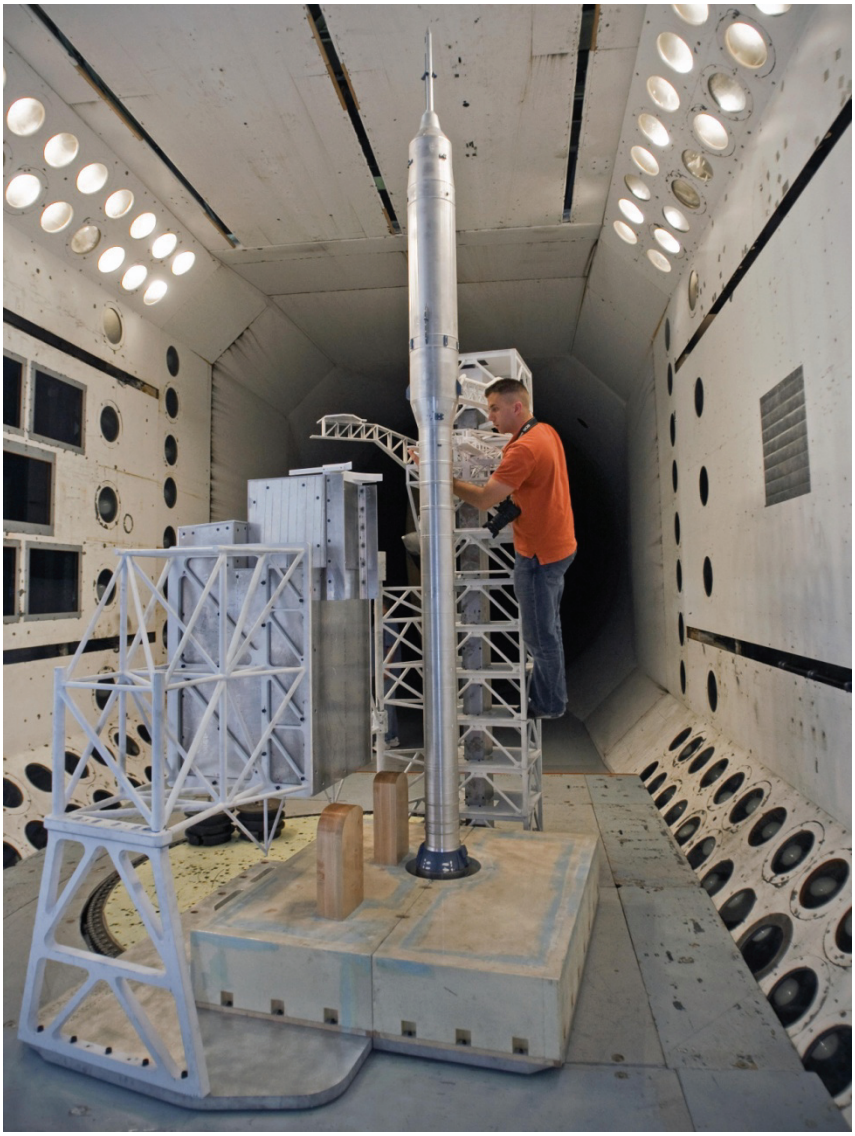

Figure 35. Ares I-X GWL Model Installed in TDT with Launch Pad Hardware Installed.
(Photo Credit: NASA/Sean Smith, used with permission)

7.2 Experimental Results

The experimental results shown in this section are categorized into two groups. The first is a presentation of the experimental results from the GWL Checkout Model that validate the general assumptions. The second is a comparison of experimental data with results of the proposed analytical method. For reference, Appendix II contains additional data from the GWL checkout model wind tunnel test.

7.2.1 Experimental Results that Support the General Assumptions

7.2.1.1 Experimental Results to Support Assumption A10 (Protuberances)

As mentioned by Ivanco and Keller (ref. 20), four configurations of the GWL Checkout Model were experimentally tested: no grit no protuberances, no grit with protuberances, with grit with protuberances, and with grit no protuberances. Protuberances include small geometric details such as a systems tunnel, roll control motors or other items that can be seen in figure 34 that add asymmetry to the launch vehicle OML. Grit refers to surface roughness added to the model on the upper stage in the form of sand grit.

If we consider otherwise identical conditions and compare the results of protuberances on to protuberances off, we can investigate the effect that Ares-like protuberances have on WIO response. Figure 36 shows the ratio of "peak" (3-sigma)[3] dynamic bending moment due to lift to mean bending moment due to drag for the model configuration with Protuberances on. The data has been converted to equivalent full-scale values of velocity. The different symbols represent different test medium total pressure values. "HG2000" denotes data acquired at near atmospheric pressure (total pressure = 2000 psf) in heavy gas (R134a). Similarly, "HG1500" denotes data acquired at a total pressure of 1500 psf in R134a heavy gas. Also, "Air" denotes data acquired in air at atmospheric pressure. HG2000 represents data at full-scale Reynolds number, and with the ideal gas laws, one can quickly determine that HG1000 is at approximately 1/2 of full-scale Reynolds numbers and "Air" is at approximately 1/6 of full-scale Reynolds number. For reference, 15 knots equivalent full-scale velocity yields a Reynolds number of approximately $3x10^6$.

Similarly, figure 37 shows the same ratio of 3-sigma bending moment due to lift over mean bending moment due to drag for the model configuration with protuberances off.

[3] 3-sigma bending moment due to lift is used in the GWL Checkout Model database in lieu of peak (maximum absolute value) bending moment due to lift. As explained in the database report (ref. 20), considering the statistical value of sigma produced more consistent results. More discussion is contained in Section 7.2.2.1 regarding the selection of 3-sigma values.

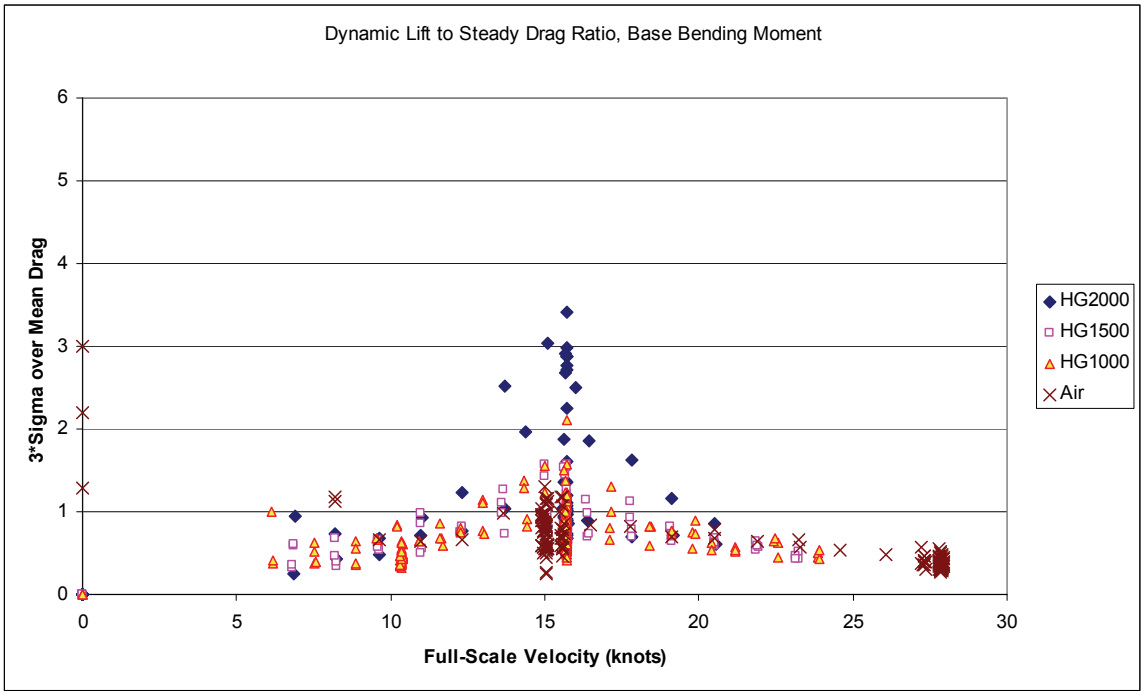

Figure 36. GWL Checkout Model Data, Base Bending Moment Ratio, With Protuberances, With Grit.

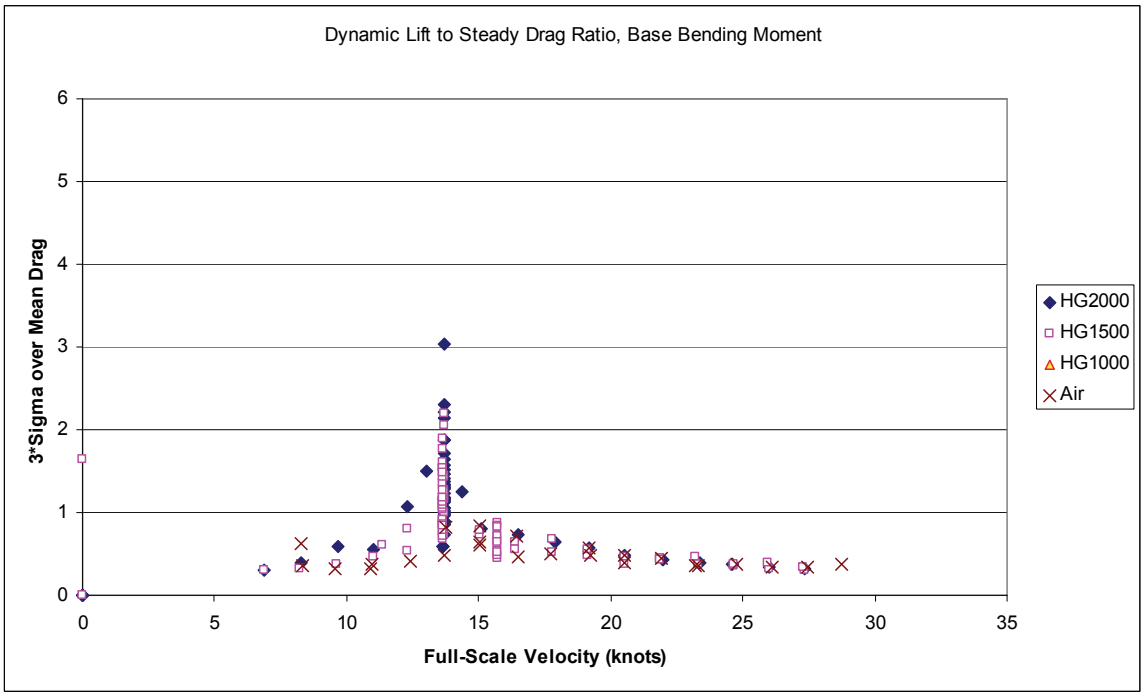

Figure 37. GWL Checkout Model Data, Base Bending Moment Ratio, Without Protuberances, With Grit.

Comparison of figures 36 and 37 reveals that the ratio of "peak" lift to mean drag (bending moment) is nearly constant regardless of whether or not the protuberances are installed. This indicates that the overall unsteady aerodynamic lift coefficient is the same between both configurations. An interesting difference, however, is that the velocity of resonant WIO response is notably different. The resonant WIO response in figure 36 produces a tip shedding Strouhal number of 0.14, where as the condition in figure 37 produces a tip shedding Strouhal number of 0.16. ESDU (ref. 3) states that the tip shedding Strouhal number for structures with parallel sides or taper ratios greater than 0.02 should be 0.16. Therefore, it is theorized that the presence of protuberances increased the size of the wake around the structure creating a larger *effective* diameter. This larger effective diameter produces a lower Strouhal number when calculated with the actual structural diameter.

Another theorized effect of protuberances (especially long narrow ones such as a systems tunnel) is that they may act to fix the separation point along certain lengths of the vehicle. This fixed and correlated separation point may also help synchronize and correlate the shed vortices along constant diameter sections of the vehicle. It was noted during wind tunnel testing of the GWL Checkout Model and the Ares I-X GWL model (Ivanco and Keller, ref. 20 and 21) that the probability for large dynamic response increased greatly when the systems tunnel was at an angle of approximately 75 to 80 degrees from the upstream stagnation point.

Summarizing the dominant effects of protuberances, it is theorized that protuberances have two large influences on WIO response. First, the local Strouhal number is decreased by approximately 0.02 for small "typical" protuberances such as that seen on Ares vehicles. Second, at certain wind azimuth angles, the protuberances will increase the probability of large dynamic response at resonant WIO velocities. However, as demonstrated in this section, it is still possible to obtain a resonant WIO response of the same magnitude (in coefficient form) without protuberances.

It should also be noted that the maximum dynamic response conditions discussed in figures 36 and 37 occurred at different wind azimuth angles. Additionally, if one only considers the data at 15 knots, then one may incorrectly conclude that a protuberance will increase the dynamic response by several factors. Therefore, it is considered of secondary importance to model the exact wind azimuth angle and velocity of a large WIO response, and of primary importance to characterize the magnitude of the large WIO response and velocity range where it may occur.

7.2.1.2 Experimental Results to Support Assumptions A10 (Grit)

Grit was added to GWL checkout model for certain model configurations in order

to study the affect of surface roughness and boundary layer turbulence. Figure 38 shows the ratio of "peak" dynamic bending moment due to lift to mean bending moment due to drag for a model configuration with protuberances and without grit. By comparison with the data presented in figure 36, one can see that the addition of grit (in the case of the GWL Checkout Model) decreases the dynamic response of the model to WIO. However, it is important for the reader to realize that the size of the grit used in the GWL Checkout Model test was large and applied with rough double-sided tape further increasing the surface roughness. According to Szechenyi (ref. 7), oversized grit (roughness height to diameter ratio >= 2.2×10^{-3}) will decrease WIO response due to a disruption of the shed vortices. However, Szechenyi also shows that proper sizing of surface roughness will enable simulation of higher Reynolds numbers and will not disrupt the vortex shedding. Therefore, surface roughness can be handled within the proposed analytical method by the calculation of *effective* Reynolds number and proper selection of aerodynamic coefficients.

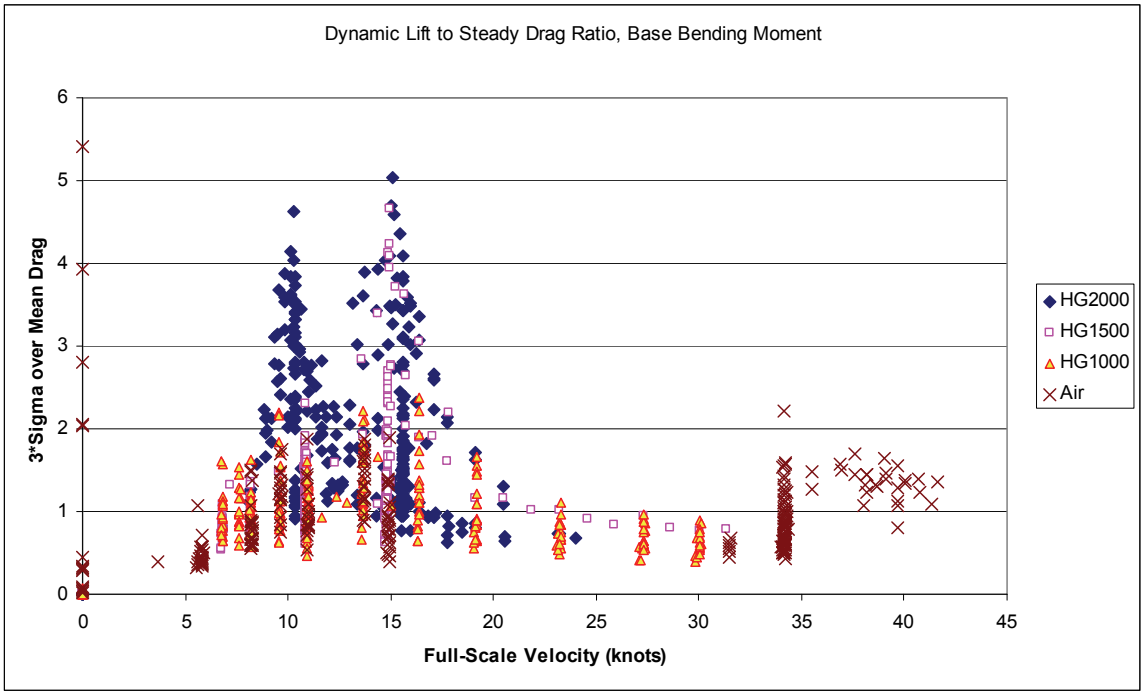

Figure 38. GWL Checkout Model Data, Base Bending Moment Ratio, With Protuberances, Without Grit.

7.2.1.3 Experimental Results to Support Assumption A7 (Extrapolation of 2D Aerodynamics)

One can also investigate the lift and drag dynamic loads calculated by integrating the time history values of the unsteady pressure data acquired by the GWL Checkout Model, as documented by Ivanco and Keller (ref. 20). Lift and drag per unit length are calculated along with C_L and C_D time histories for the

instrumented sections of the model. One can extract the experimental values of steady C_L and C_D and the oscillatory values of C_L' and C_D'. If we assume that the oscillatory lift value is sinusoidal in response, then the amplitude of C_L, hence C_L' in the analysis, would be the $\text{Lift}_{RMS} \cdot \sqrt{2}$. For the majority of data points, this yields a C_L' of about 0.2 and is reasonably consistent with the data shown by Chen (ref. 2), the curve fit of which is defined by equation 25 in Section 4.2.4. Recall, the curve fit used in the proposed analytical method assumes the largest values of the data scatter presented by Chen.

7.2.1.4 Experimental Results to Support Assumption A5 (Lock-on)

Shown in this section is an experimental example of the occurrence of Lock-on with the GWL Checkout Model for a Reynolds number of approximately 3×10^6. Several charts are presented where each chart contains several PSD plots. The PSD plots are of the unsteady pressure transducers (denoted as Press###) located around the azimuth of the model in the upper stage. The locations of the PSD plots around the circumference of the chart are such that they approximate the azimuthal position of the transducer with respect to the flow. The PSD plots in the center of the chart show the structural response measured with accelerometers aligned with the structural axes and the base bending moments due to lift and due to drag (denoted as LBM and DBM respectively). Information regarding the test condition is also shown at the top of the chart indicating the wind tunnel velocity, the Reynolds number (based on upper stage diameter) and model configuration.

Figure 39 shows the results for a wind tunnel velocity of 110.3 ft/s (equivalent full-scale velocity of 15 knots). The peak responses of the pressure PSD's align with the structural frequency of the first bending mode (16 Hz) and yields a Strouhal number of 0.14 (tip-shedding event).

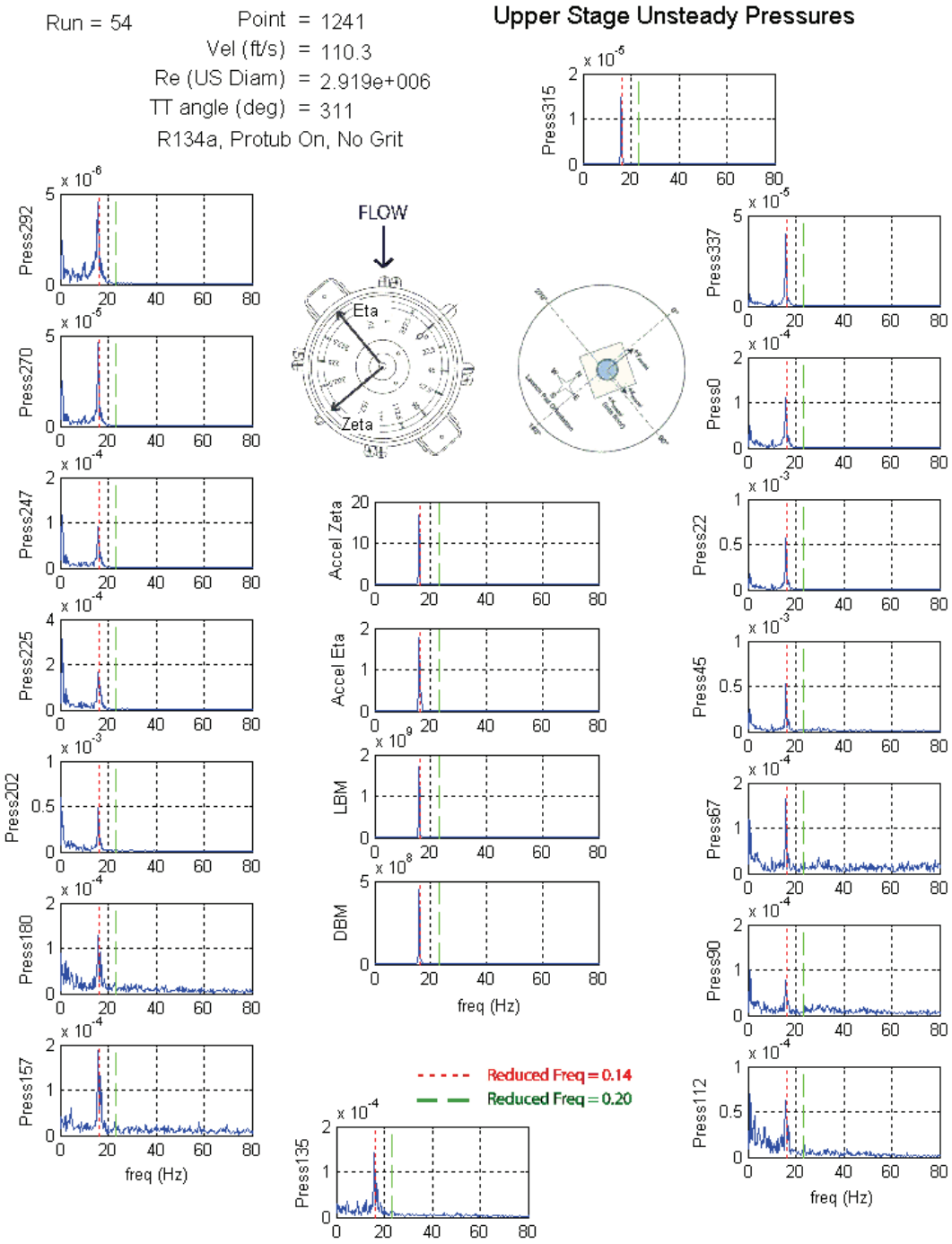

Figure 39. PSD Plots of Unsteady Pressures for Velocity of 110.3 ft/s, Peak Excitation, Resonant WIO Response.

Figure 40 shows the PSD results for a wind tunnel velocity of 120.1 ft/s. One can observe that the shedding frequency measured by the unsteady pressure transducers is still at the structural frequency even though the velocity has increased by approximately 10% above the peak resonant velocity.

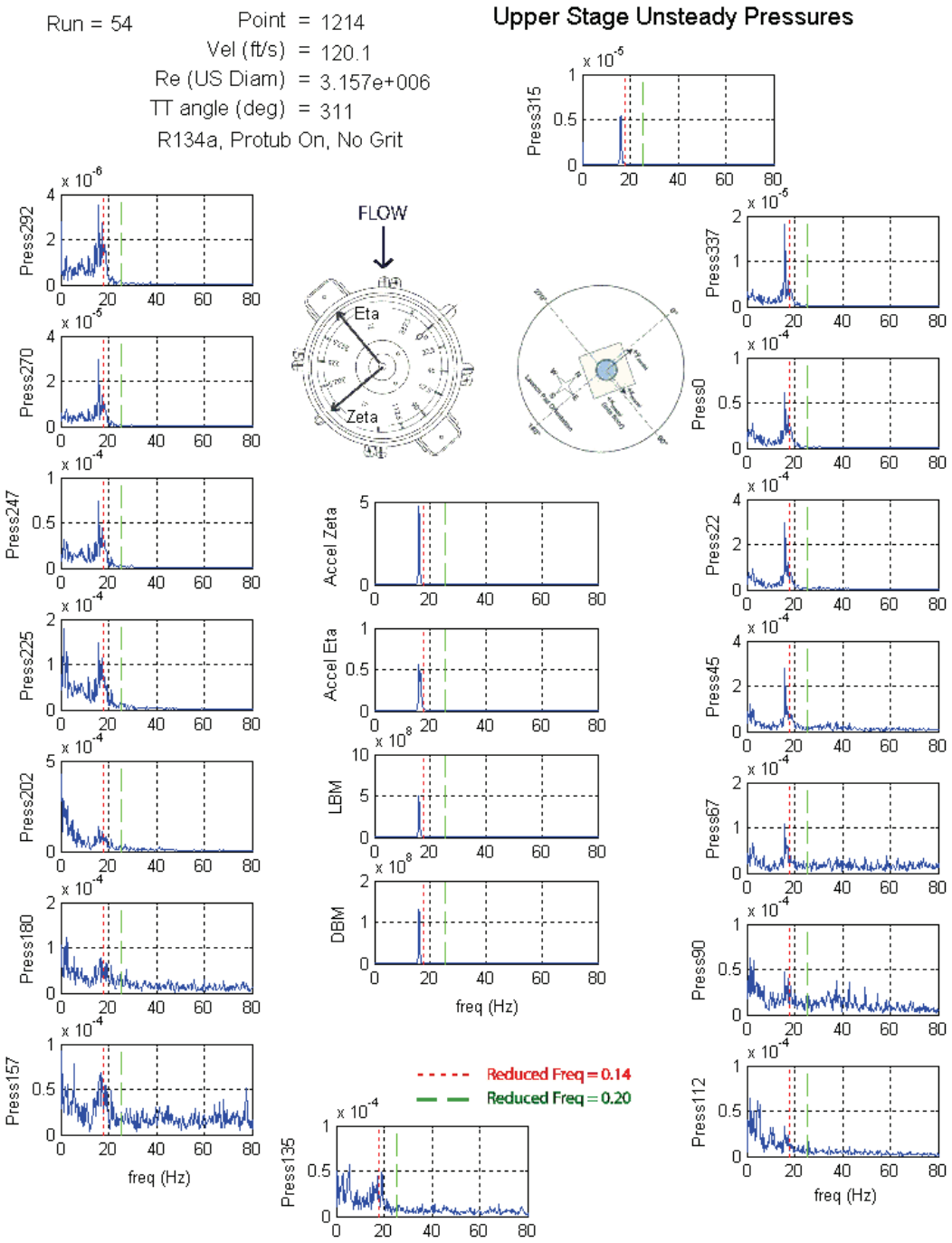

Figure 40. PSD Plots of Unsteady Pressures for Velocity of 120.1 ft/s, Example of Lock-on, Shedding Frequency Removed from Natural Shedding Frequency and Aligned with Structural Frequency.

Finally, figure 41 contains the PSD results for a wind tunnel velocity of 130.1 ft/s. In figure 41, one can see that the shedding frequency has returned to the

Strouhal shedding frequency (St=0.14) at approximately 20 Hz and is no longer aligned with the structural frequency of 16 Hz. This velocity is 18% above the lock-on velocity and, according to theory, the shedding should return to its natural frequency at this condition (ref. 2 and 3).

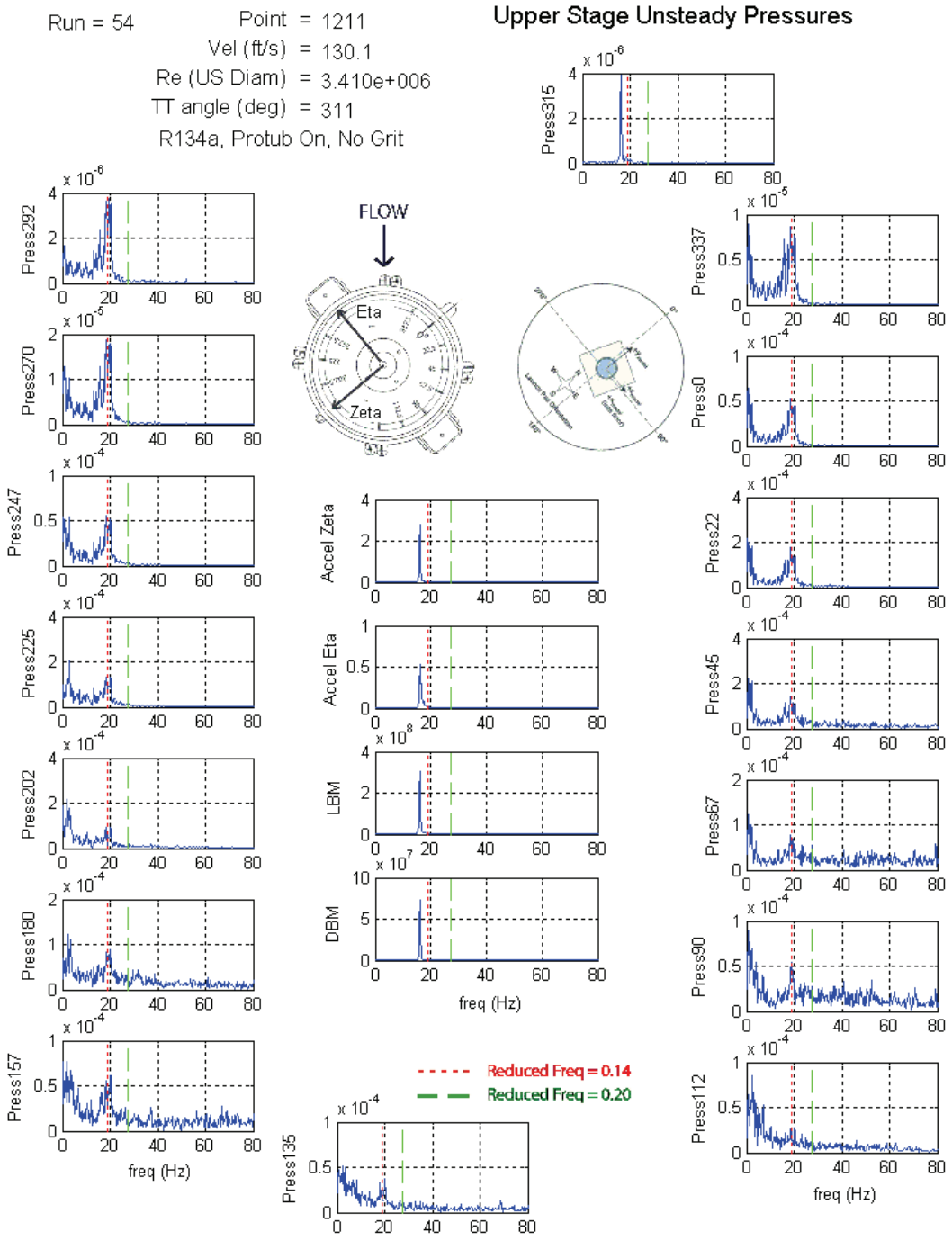

Figure 41. PSD Plots of Unsteady Pressures for Velocity of 130.1 ft/s, Shedding Frequency Returns to Natural Shedding Frequency and No Longer Aligned with Structural Frequency.

7.2.2 Comparison of Analytical Method with Experimental Data

The analytical results shown in this section are determined with the aeroelastically-coupled discrete frequency approach. Analytical predictions were performed for the GWL Checkout Model, the Ares I-X GWL model, and the Ares I-X full-scale vehicle. To preserve the sensitive nature of the data, the results for the Ares I-X GWL model are shown on normalized axes only. The analytical results for the full-scale Ares I-X shown in other sections of this thesis; however, are shown on dimensional axes. It is important to note that the analytical predictions of the full-scale Ares I-X will be significantly different than the scaled wind tunnel data (and associated predictions) of the Ares I-X GWL model. This is because the model-scale Ares I-X analytical results and data shown in this section are for the as-tested model properties of structural damping, frequency, wind profile, and fluid properties of R134a heavy gas. The full-scale Ares I-X results, shown in other sections of this thesis, are for different values of structural damping, wind profile, and fluid properties. Therefore, one cannot deduce the dimensional Ares I-X GWL wind tunnel results from comparison of the data shown in this section with analytical results in other sections of this thesis.

7.2.2.1 GWL Checkout Model Comparison with Analysis

The analytical model was used to predict the response of the GWL Checkout Model for code validation and development. The Checkout Model geometry, frequencies, damping and fluid properties were input into the aeroelastically-coupled discrete frequency approach. The analytical results compared with tunnel data are shown in figure 42. For the wind tunnel data, the value representing the peak bending moment due to lift is the 3-sigma value. For the Checkout Model, the dynamic response was rarely sinusoidal and the zero-offset of the bending moment gages drifted with time. Therefore, it is considerably more consistent (and considered more accurate) to represent the peak bending moment due to lift as a 3-sigma value of the dynamic bending moment due to lift. The Ares I-X model utilized higher quality bending moment gages that were more accurate and did not drift in time. Therefore, for other sections of this thesis, “Peak” refers to the maximum absolute value of the time history.

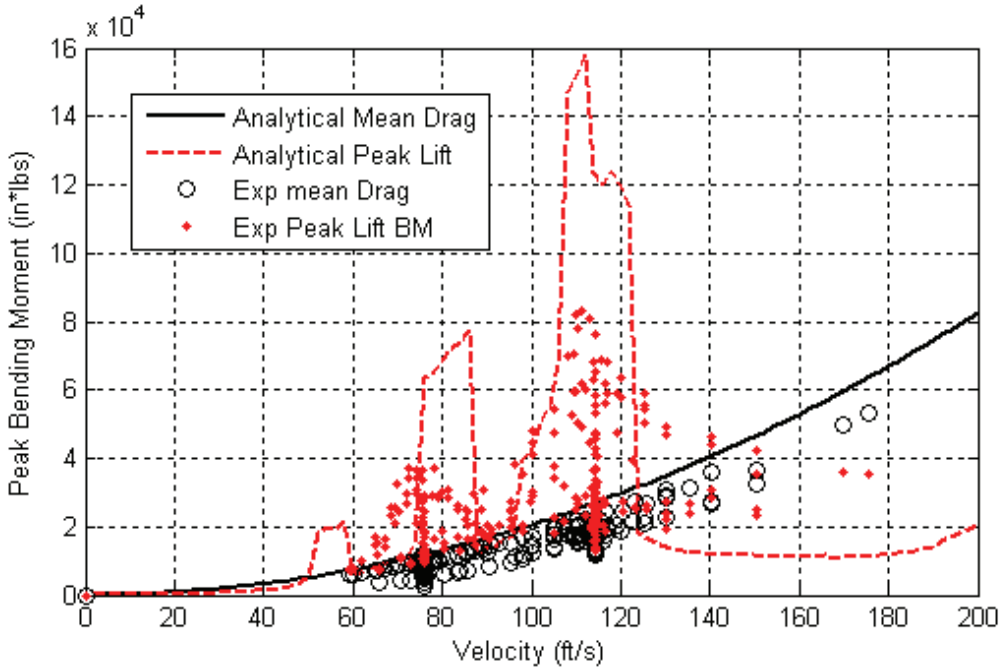

Figure 42. Comparison of GWL Checkout Model Data with Analytical Method Predictions, Bending Moments due to Lift and Drag.

Using the Strouhal number distribution presented in this report, the velocities of predicted resonant WIO response match well with the wind tunnel data. However, the analytical method magnitude is rather conservative. For the Checkout Model, damping of the first modes was 1% of critical and damping of the second modes was 1.25% of critical. As previously discussed, it is theorized that lower structural damping will increase the synchronization of vortex shedding along constant diameter sections as a result of an increase in structural motion. The discrete frequency approach assumes complete vortex shedding synchronization along constant diameter sections that are exposed to the same velocity and posses the same Strouhal number. Therefore, models with lower structural damping (less than 1%) are expected to show better correlation with the analytical results.

The multiple peaks shown in figure 42 are all first mode WIO excitations that result from resonant vortex shedding occurring on different sections of the vehicle. Second bending mode excitations are expected to occur at higher velocities than those shown in figure 42.

A phenomenon that was not predicted with the aeroelastically-coupled discrete frequency approach is that the dynamic bending moment in the lift direction is on the order of the steady drag loads for conditions removed from a resonant WIO response. This response is expected to be an effect of a forcing function that is not explicitly discrete and turbulence as discussed in Section 6.3.

7.2.2.2 Ares I-X GWL Model Comparison with Analysis

The aeroelastically-coupled discrete frequency approach was run with the Ares I-X GWL model-scale values of geometry, frequency, damping, and fluid properties. The structural frequencies in the η and ζ axes differed, as mentioned in Section 7.1.3. Therefore, the velocities associated with resonant WIO response are different for orthogonal wind azimuth angles. Presented in figure 43 are the analytical results for two different wind azimuth angles, each angle placing one of the fundamental structural axes orthogonal to the flow direction. The wind tunnel data shown in figure 43 is for all wind azimuth angles tested (approximately 73 different angles) between 0 and 360 degrees. As previously mentioned, the Ares I-X data is sensitive; therefore the values shown here are normalized by an arbitrary constant. Damping for the Ares I-X wind tunnel model was considerably below 1% for the first bending modes. As a result, one should expect a larger dynamic response and expect better correlation with predicted first mode magnitudes than shown for the GWL Checkout Model.

The peak WIO responses in figure 43 at normalized velocities of 0.2 and below are first mode responses. The analytical peak WIO responses above a normalized velocity of 0.3 are second mode responses. The experimental peak response at a normalized velocity of 0.33 is exclusively a second mode response and corresponds to the predicted analytical "plateau" ranging from 0.35 to 0.4. The other experimental responses (due to lift) for normalized velocities above 0.4 contain a mix of second and first mode with a large percentage of the overall load corresponding to first mode responses.

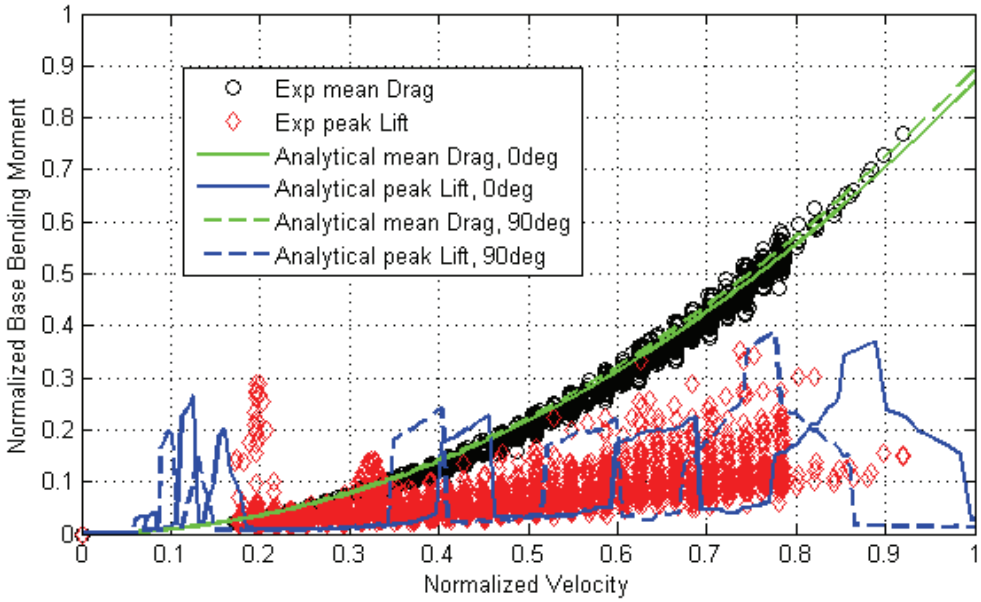

Figure 43. Comparison of Ares I-X GWL Data with Analytical Method Predictions, Bending Moments due to Lift and Drag.

For the comparison shown in figure 43, the analytical method correlates well with experimental data regarding bending moments at the base. The peak WIO response velocities, however, do not match as well as they did for the Checkout Model. This is a direct result of assuming a two-dimensional Strouhal number of 0.2 for all velocities, even though higher velocities will produce supercritical Reynolds numbers. It is also anticipated that there would be more experimental WIO response peaks for normalized velocities below 0.2 if the wind tunnel model and facility where capable of modeling that velocity range. As mentioned in Section 7.1.3, the aeroelastic scaling relationships and desired full-scale velocity range prohibited the simulation of low velocity conditions where most of the first mode WIO responses will occur.

Referring to figure 2 in Section 1.3, one can also investigate the maximum resultant bending moment as a function of velocity. Figure 44 is comparison of the analytical and experimental results of maximum resultant bending moment.

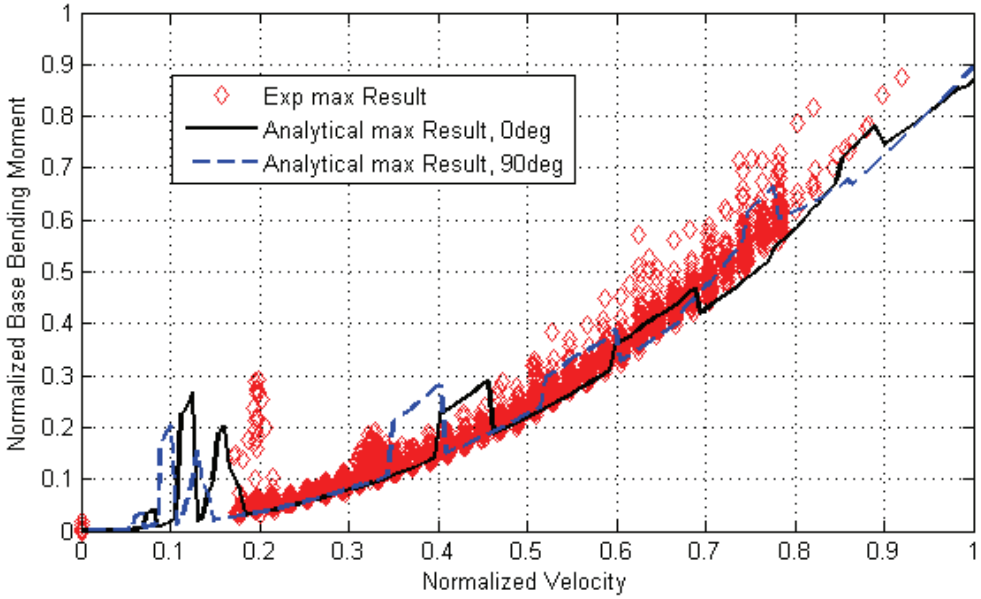

Figure 44. Comparison of Ares I-X GWL Data with Analytical Method Predictions, Maximum Resultant Bending Moments.

Experimental configurations were also run with nearby tower structures present. These structures did not make contact with the launch vehicle and were included for aerodynamic influence only. The current analytical method does not have the capability to simulate the aerodynamic effect of nearby structures except for qualitatively estimating a turbulence increase and associated effects with the aeroelastically-coupled turbulence-coupled approach, not shown in this section of the thesis. Figure 45 shows a comparison between the experimental results (with tower structures present) compared to the analytical results from the aeroelastically-coupled discrete frequency approach. Note that the analytical

results in figure 45 are identical to those shown in figure 43. As one may expect, there is a greater scatter in the experimental mean bending moment due to drag resulting from the vehicle being exposed to the wake of the tower structures for certain wind azimuth angles.

In figure 45, the magnitude of the peak bending moment due to lift (measured at the base) is only slightly increased for normalized velocities above 0.3 by comparison to figure 43. However, it was observed during testing that the frequency content of the dynamic response was considerably different than the rollout configuration presented in figure 43. The dynamic response with tower structures present was dominated by second mode content with a magnitude very similar to the analytical results. Even though the base bending moment magnitude is similar for the experimental data in figures 45 and 43, it is important to note that the distributed load magnitude will be considerably different. Recall, distributed bending moment loads of the second modes are considerably different than the distributed bending moment loads of the first modes as illustrated in figure 7.

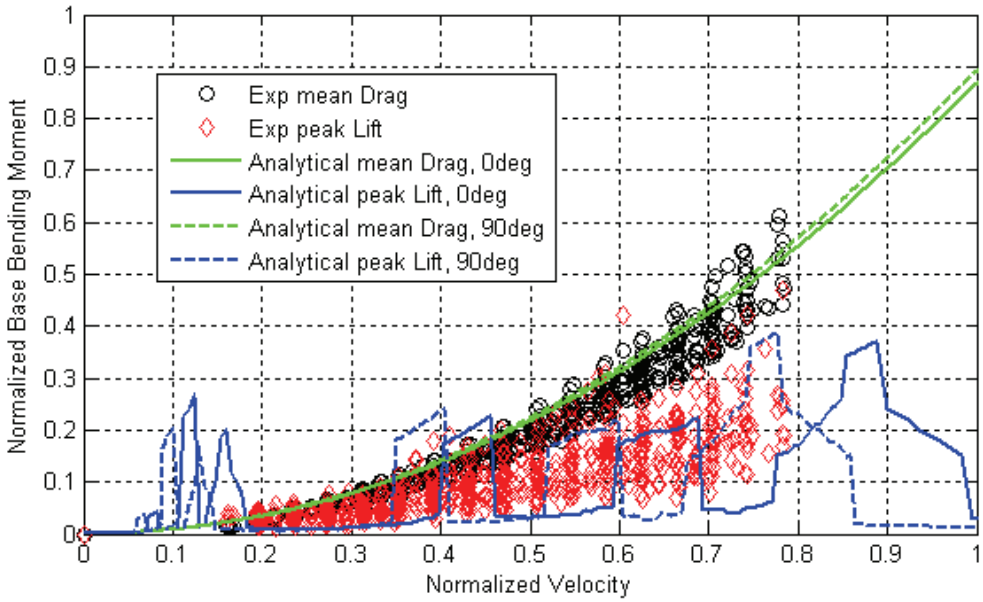

Figure 45. Comparison of Ares I-X GWL Data with Analytical Method Predictions, Bending Moments due to Lift and Drag, Experimental Data has Tower Structures Present.

Similarly, figure 46 is a comparison between the analytical predictions and experimental results with tower structures present of the maximum resultant bending moment. Note that the analytical predictions are identical to those shown in figure 44.

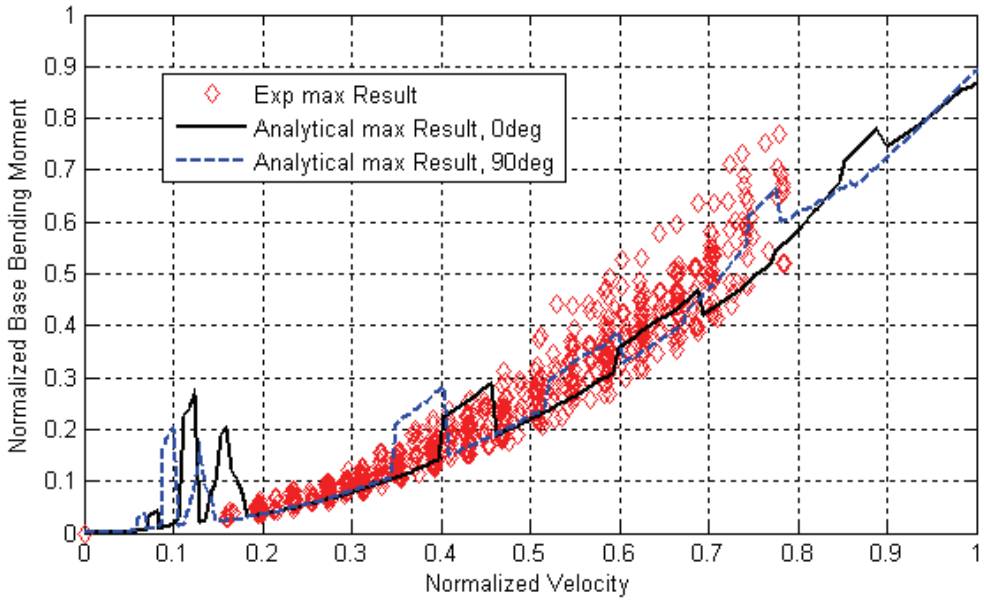

Figure 46. Comparison of Ares I-X GWL Data with Analytical Method Predictions, Maximum Resultant Bending Moments, Experimental Data has Tower Structures Present.

8.0 Recommendations for Future Analyses

Recommendations for future analyses are divided into two sections. The first section discusses improvements to the analytical method and proposed studies that can be done to further validate or improve the method accuracy. The second section discusses the application of the proposed analytical method to future launch vehicle designs.

8.1 Future Development and Validation of Analytical Method

It is recommended that more research and study be conducted investigating the effect of turbulence upon WIO. One can further investigate the aeroelastically-coupled turbulence-coupled approach over longer time records to gain better statistical quantities and trends. This approach can also be expanded to include turbulence forcing functions in the drag direction. The results of these additional studies should then be compared with methods that treat WIO and turbulence response as independent functions to confirm the ability to model WIO-turbulence coupling. Experimental data measuring the effect of turbulence on launch vehicle WIO response in the supercritical Reynolds number range is not known and would aid greatly in the study of this problem. It is also not understood if the increase in turbulence (due to the presence of tower effects) played a role in the significant increase in second bending mode response observed in the Ares I-X GWL test with the inclusion of tower structures.

In addition to more analysis of turbulence effects, it is recommended to explore gust modeling. Incorporating gust loads into the current method is already possible with the current equations of motion, however, no such time-varying forcing function (g') was proposed in this thesis.

More investigation of the low amplitude effects on the oscillating lift coefficient RMS should be done using the data presented by Jones, Cincotta, and Walker (ref. 25). Jones et al. show a greater sensitivity to small amplitude motion than modeled in this thesis but a smaller rigid oscillating lift coefficient RMS.

Finally, it is recommended that the current analytical method be compared to full-scale data (when available). This requires detailed knowledge of the full-scale wind profiles, turbulence levels, vehicle geometry, frequencies, mode-shapes, and mass-distribution. Jones and Gilman (ref. 10) show data for a full-scale Scout launch vehicle that contain the needed parameters.

8.2 Application of Proposed Analytical Method to Future Launch Vehicle Designs

When applying the proposed analytical method to future designs, it is advisable to start with the simple approach using conservative coefficients. If necessary, one can refine the analysis and use the aeroelastically-coupled discrete

frequency approach. It is then recommended to spot check certain velocity and azimuth angles with the aeroelastically-coupled turbulence-coupled approach. Checking a non-resonant WIO response with the turbulence-coupled approach should provide insight regarding the required load increase factor to account for turbulent atmospheric flow. It is also advisable to run the turbulence-coupled approach for the most critically loaded resonant WIO response to investigate WIO-turbulence coupled effects.

Wind tunnel testing of final configurations is still recommended to verify the assumptions and design loads, and to quantify the effects of nearby structures. Gust and turbulence effects still need to be determined analytically and evaluated by combination with wind tunnel data, as shown in Section 2.5, and by independent analytical study as shown in Section 6.3. All required equations are presented in Section 4.0, and guidance is given within each approach regarding the selection of coefficients.

9.0 Summary and Conclusions

A dynamic modal analysis method has been developed to calculate the structural response of launch vehicles to ground wind loads (GWL). Ground wind loads refer to the loading a launch vehicle (or similar structure) experiences while exposed to atmospheric winds. Of particular interest is the response to vortex shedding, referred to as wind-induced oscillation (WIO), which has the potential to produce nearly harmonic aerodynamic loads. At certain wind velocity and flow angle conditions, this harmonic forcing can excite natural modes of the structure and force it in resonance. The primary focus of the proposed analytical method is the calculation of this resonant response; however, steady loads and dynamics at other than resonant conditions are also calculated.

The proposed analytical method utilizes aerodynamic equations derived from wind tunnel data of two-dimensional cylinders for various values of surface roughness, Reynolds number, structural motion, and turbulence intensity. The two-dimensional aerodynamic equations are corrected for three-dimensional tip effects based upon the vehicle fineness ratio and experimental results presented in ESDU (ref. 3) and by Ivanco and Keller (ref. 20 and 21). Results of this new analytical method show reasonably good correlation with wind tunnel data of launch vehicles. The newly developed analytical method is presented in this thesis as three different “approaches” each of different complexity: A simple approach, an aeroelastically-coupled discrete frequency approach, and an aeroelastically-coupled turbulence-coupled approach. Each increasingly complex approach is capable of modeling more of the observed behavior of wind tunnel and full-scale vehicles. However, the turbulence-coupled approach may produce un-conservative load predictions as it is currently presented and should be used in conjunction with the discrete frequency approach. This proposed analytical method can also be extended to fields of similar study such as the dynamic response of chimneys or underwater structures.

Through the development and validation of this analytical method, there were several characteristics of GWL that were calculated and/or observed in testing.

1. Excitation of structural modes other than the fundamental bending mode is possible. The higher modes of vibration can also be excited with very little participation of other modes and the response can be nearly-sinusoidal.
2. Structural damping of 3% or greater significantly reduces dynamic response to wind-induced oscillations.
3. Historically, full-scale data has shown a significant increase in dynamic WIO response beyond what wind tunnel and previous analytical methods have shown. The proposed analytical method shows that this may be the result of atmospheric turbulence that was not simulated in the wind tunnel tests.
4. The effects of atmospheric turbulence, as predicted with the proposed analytical method and the equations presented in ESDU (ref. 3) are:

a. Turbulence widens the frequency bandwidth of dynamic lift, and lowers the peak PSD magnitude.
b. Turbulence increases the RMS value of dynamic lift.
c. For velocity regions far removed from a resonant WIO response, turbulence content significantly increases the dynamic response of the vehicle, especially in the fundamental modes.
d. WIO strength is affected by turbulence content. Turbulence may increase the WIO response beyond what the independent addition of smooth air WIO response and random turbulence response will predict for many conditions. This is especially true for conditions where the vehicle region experiencing resonant WIO forcing is small and the broadening of the lift force PSD may expand the vehicle region that experiences resonant WIO forcing. Turbulence can also reduce the WIO response encountered for conditions that have large regions of resonant WIO forcing that yield large sinusoidal response in smooth flow.

Application of this analytical method is recommended for future launch vehicles and offers the user the ability to predict GWL early in design. A reasonably accurate prediction of GWL early in the design of a vehicle and support systems is critical for making intelligent design decisions, guiding wind tunnel testing, and in the establishment of operational restrictions.

REFERENCES

1. Terrestrial Environment (Climatic) Criteria Handbook for use in Aerospace Vehicle Development. NASA-HDBK-1001. August, 2000.
2. Chen, Shoei-Sheng; Flow-Induced Vibration of Circular Cylindrical Structures. Hemisphere Publishing Corporation. 1987
3. Response of Structures to Vortex Shedding. Structures of Circular or Polygonal Cross Section. Engineering Sciences Data Unit (ESDU) Report 96030. December, 1996. Amended July, 1998.
4. Arunachalam, S.; Govindaraju, S.P.; Lakshamanan, N.; Appa Rao, T.V.S.R.; Across-Wind Aerodynamic Parameters of Tall chimneys with Circular [Cross-Section]. Engineering Structures – ELSEVIER. May 2000.
5. D'Asdia, P.; Noe, S.; Vortex Induced Vibration of Reinforced Concrete Chimneys: In Situ Experimentation and Numerical Previsions. Journal of Wind Engineering and Industrial Aerodynamics 74-76 (1998) 765-776.
6. Hanson, Perry.; Jones, George; On the Use of Dynamic Models for Studying Launch Vehicle Buffet and Ground Wind Loads. NASA Langley Research Center. NASA TM X 50548. September 1963.
7. Szechenyi, Edmond; Supercritical Reynolds Number Simulation for Two-Dimensional Flow over Circular Cylinders. Office National d'Etudes et de Recherches Aerospatiales (ONERA), France. April, 1974.
8. Prelaunch Ground Wind Loads. Space Vehicle Design Criteria, NASA SP-8008. November, 1965.
9. Farmer, Moses; Jones, George; Summary of Wind Tunnel Studies of Ground Wind Loads on Launch Vehicles. NASA Langley Research Center N66-32228.
10. Jones, George; Gilman, Jean; Measured Response to Wind-Induced Dynamic Loads of a Full-Scale Scout Vehicle Mounted Vertically on a Launching Tower. NASA TN D-757. April 1961.
11. Meirovitch, Leonard; Elements of Vibration Analysis, Second Edition. © 1986, McGraw-Hill, Inc.
12. Wang, Meng; Catalano, Pietro; Iaccarino, Gianluca; Prediction of High Reynolds Number Flow over a Circular Cylinder Using LES with Wall Modeling. Center for Turbulence Research, Annual Research Briefs, 2001.
13. Reed, Wilmer; Models for Obtaining Effects of Ground Winds on Space Vehicles Erected on the Launch Pad. NASA Langley Research Center. 1964.
14. Constellation Program Design Specification for Natural Environments (DSNE), CxP 70023. Revision A, Change 1. November 2008.
15. Runyan, H. L.; Morgan, H. G.; Mixson, J. S.; Role of Dynamic Models in Launch Vehicle Development. NASA 1962.
16. Jones, George; Farmer, Moses; Wind Tunnel Studies of Ground Wind Loads on Saturn Launch Vehicles. NASA Langley Research Center. Journal of Spacecraft. Volume 4, No 2. February 1967.

17. Foughner, Jerome; Duncan, Rodney; A Full-Scale Ground Wind Loads Program. NASA Langley Research Center. N66 32230. January 1966.
18. Meeting on Ground Wind Loads Problems in Relation to Launch Vehicles. NASA Langley Research Center, June 7-8, 1966. Compilation of Papers. N66 32226 through N66 322250. NASA TM X-57779.
19. Mackey, Alden; Schwartz, Robert; Apollo Experience Report – the Development of Design-Loads Criteria, Methods, and Operational Procedures for Prelaunch, Lift-off, and Midboost Conditions. NASA TN D-7373. August 1973.
20. Ivanco, Thomas; Keller, Donald; Database Release, Ground Wind Loads Checkout Model, Transonic Dynamics Tunnel Test 595. Ares-AE-TA-0003. April, 2008.
21. Ivanco, Thomas; Keller, Donald; Ares I-X Ground Wind Loads Database Release and Data Analysis Report. Ares-AE-TA-0007. April 2009.
22. Structural Interaction with Control Systems. Space Vehicle Design Criteria. NASA SP-8079. November 1971.
23. Houbolt, John; Steiner, Roy; Pratt, Kermitt; Dynamic Response of Airplanes to Atmospheric Turbulence Including Flight Data on Input and Response. NASA TR R-199. June 1964.
24. von Kármán, Theodore; Progress in the Statistical Theory of Turbulence. Presented at the Heat Transfer and Fluid Mechanics Institute. Vol. 34. June 1948.
25. Jones, George; Cincotta, Joseph; Walker, Robert; Aerodynamic Forces on a Stationary and Oscillating Circular Cylinder at High Reynolds Numbers. NASA TR R-300. February 1969.
26. Hibbeler, R.C.; Mechanics of Materials, Second Edition. © 1994, Prentice Hall.
27. Jones, George; Unsteady Lift Forces Generated by Vortex Shedding about a Large Stationary and Oscillating Cylinder at High Reynolds Numbers. ASME Symposium on Unsteady Flow. Philadelphia, PA. May 1968. ASME 68-FE-36.
28. Staff of the Aeroelasticity Branch. The Langley Transonic Dynamics Tunnel. Langley Working Paper LWP-799, September, 1969.
29. Hammond, C. E.; Doggett, Robert; Determination of Subcritical Damping by Moving-Block/RandomDec Applications. NASA Symposium Flutter Testing Techniques. NASA CP-415 p. 59-76. October, 1975

Appendix I - Design, Development and Use of an Internal Damper in Wind Tunnel Testing

I.1 Damping Discussion

The damper discussed in this appendix was conceived and designed by the author to vary structural damping of the wind tunnel models. This device enabled the direct comparison of damping variation with analytical predictions with respect to WIO. This damper design is unique and more effective than other dampers of comparable mass and size.

Structural damping is a critical parameter that affects vehicle response to WIO. The primary mechanism driving WIO is the periodic aerodynamic forcing associated with vortex shedding. At certain velocities, this shedding frequency can occur at one of the natural frequencies of the vehicle, and as a result, the magnitude of dynamic response is heavily dependent upon structural damping. As mentioned by Chen, ESDU, and Jones (references 2, 3 and 27) and as demonstrated in this thesis, structural motion can significantly increase the magnitude of the aerodynamic forcing function thereby making WIO an aeroelastically-coupled event.

To investigate the effect of structural damping upon the dynamic response of the Ares I-X model, an internal mass-spring-damper was designed and fabricated for use in the wind tunnel test. Structural damping was experimentally determined by analyzing the time-history data from appropriate accelerometers or base bending moment readings taken during hammer impact tests. The data were reduced using the moving block technique described by Hammond and Doggett (ref. 29). Damping was also evaluated as part of the ground vibration test (GVT), although the data from the GVT is not presented in this thesis.

I.2 Tuned Mass-Spring-Damper Description and Design

Several parameters were considered during the design of the tuned mass-spring-damper. The apparatus had to fit internally to avoid affecting the airflow around the vehicle. It also needed to weigh the same as and replace an existing mass-ballast in the model. It also needed to be adjustable in overall mass and adjustable in effectiveness to achieve a target damping value. Finally, the most difficult design constraint was the damper could not affect the vehicle mode shapes, frequencies, or introduce a new mode of vibration while varying structural damping as much as 2% or more.

A MATLAB simulation was developed based upon the FEM predictions for the wind tunnel model geometry, mass, frequencies, mode shapes, and proposed damper location. This simulation was employed to determine the maximum

allowable damper mass such that the damper component loads were not exceeded and the vehicle vibration was not altered. If the moving mass of the damper was too large, the vibration energy would trade between the vehicle and damper causing the vehicle response to "beat" as it decays, in addition to creating large loads in the dynamic components of the damper. In general, a beating response is acceptable for any damped system except for the case of model simulation where the intent of the damper is to simulate the free response of a system with higher inherent damping. In such a case, matching the dynamic characteristics of the response of the simulated system is important. Conversely, if the moving mass of the damper was too low, the effectiveness of the damper would be reduced.

The MATLAB simulation also determined the required spring rates for each target mode of vibration, viscosity, and the predicted range of motion of the moving mass. A peak damping increase of 2.5% was targeted as the damper design point based upon the conclusions of Jones and Farmer (ref. 16). Lower damping values were then easily achieved by intentional off-tuning of the damper. The weight of the overall damper system was adjustable by adding or removing mass from the fixed damper frame as needed to keep the frequencies and mode shapes of the wind tunnel model unaltered. Once tuned for particular modes of vibration, the damper had a minimal impact on the damping of other modes of the wind tunnel model. A patent has been applied for by the author for the damper concept.

[image removed]

Figure I.1. Tuned Mass-Spring-Damper

I.3 Damping Test Results

Due to limited test-time, only one model configuration was run with the damper installed and only for a limited set of wind azimuth angles and velocities. An inspection of the data revealed that the modes 1ζ and 2η both encountered a significant WIO response in the Rollout configuration with baseline damping for the Ares I-X wind tunnel model. Since these responses occurred in different axes, the tuned-damper could be configured to target both modes simultaneously.

The damper was tuned in the η-axis to increase the system damping of mode 2η and the ζ-axis to increase the system damping of mode 1ζ. No attempt was made to increase the damping of modes 1η or 2ζ. Figure I.2 shows the damping results of the vibration modes 1ζ and 2η with and without the damper installed, expressed as normalized values of damping to protect the sensitive nature of the wind tunnel data.

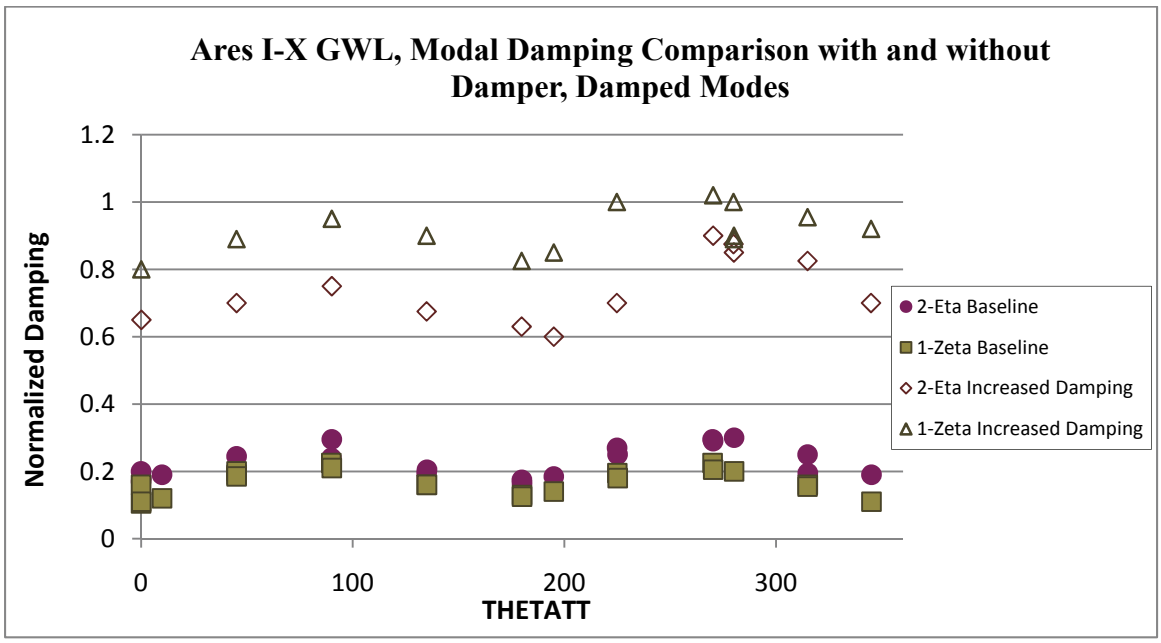

Figure I.2. Structural Damping Comparison, Modes 1ζ and 2η, at Various Turntable Angles Showing Damper Effectiveness

Figure I.3 contains the damping results, expressed as a normalized value, for the modes 1η and 2ζ. In general, the presence of the damper has a minimal impact upon the damping of modes 1η and 2ζ.

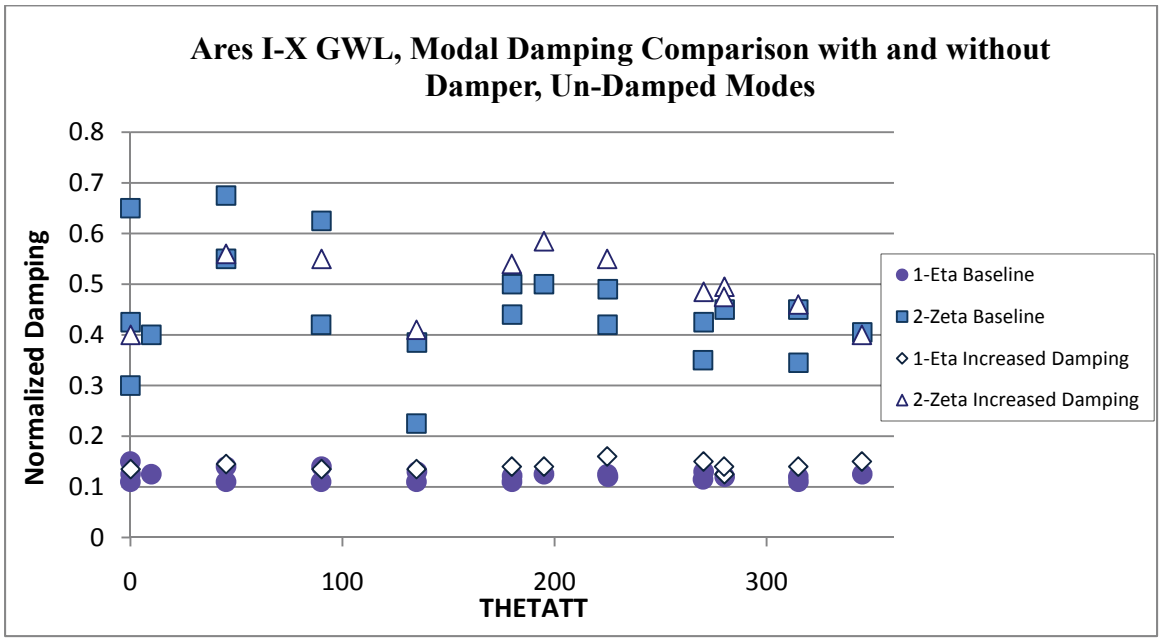

Figure I.3. Structural Damping Comparison, Modes 1η and 2ζ, at Various Turntable Angles for Modes that the Damper does not Affect

Figures I.4 and I.5 contain the normalized frequency content for the same data

records as shown in figures I.2 and I.3. One can observe that the frequency content of each mode is unaffected by the presence of the damper.

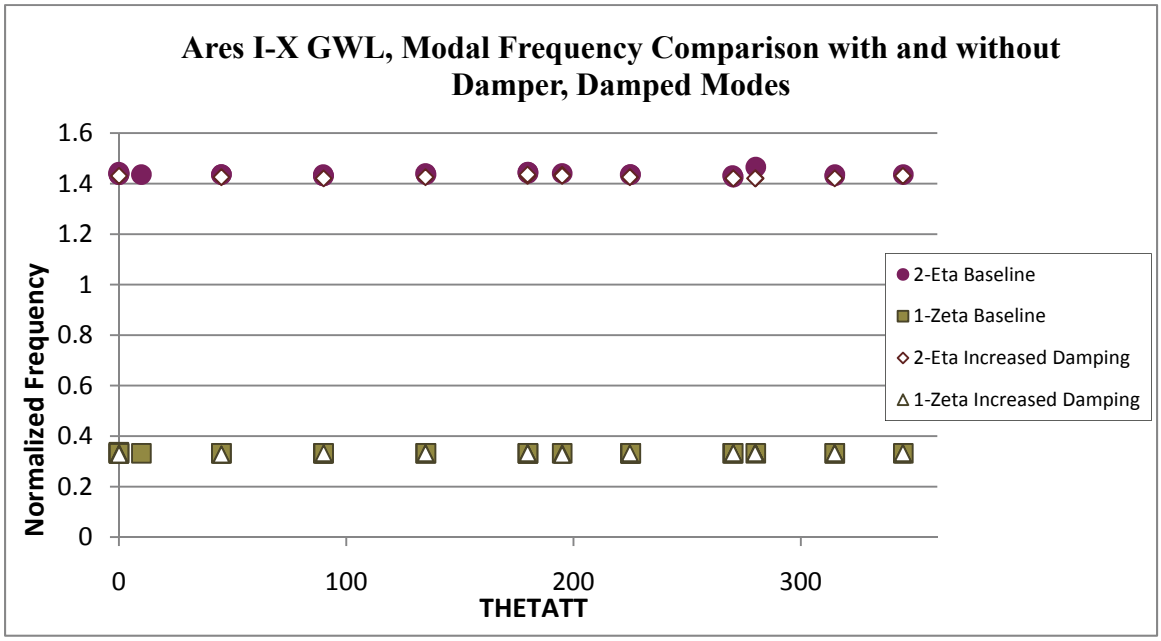

Figure I.4. Modal Frequency Comparison, Modes 1ζ and 2η

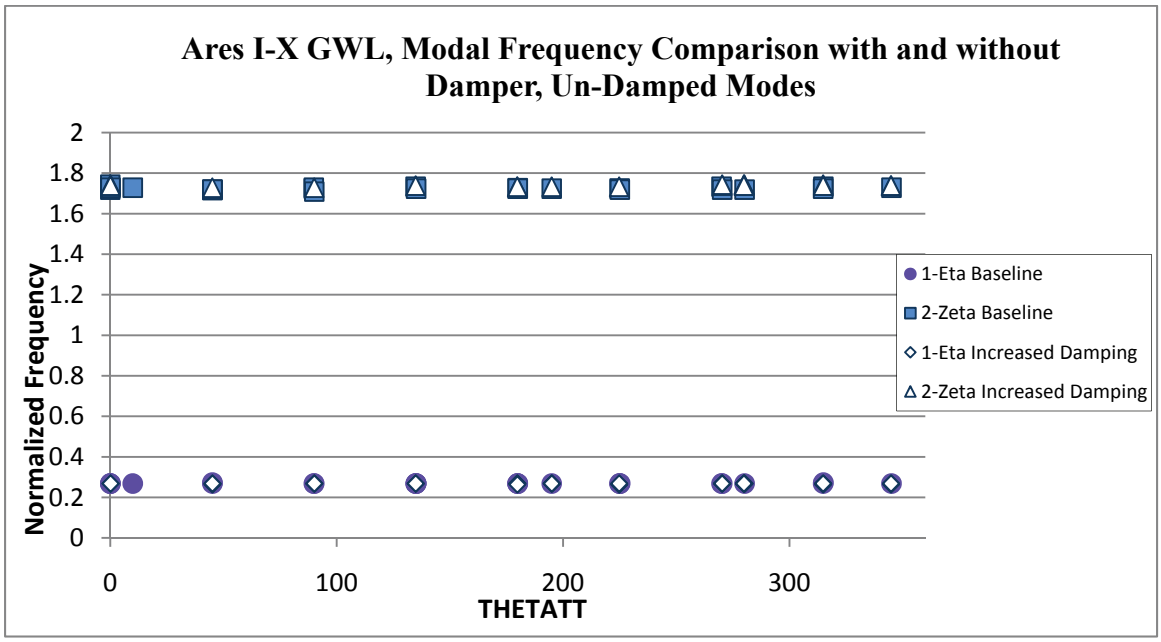

Figure I.5. Modal Frequency Comparison, Modes 1η and 2ζ

To better illustrate the effect of the damper upon modes 1ζ and 2η, the time history traces of acceleration in the ζ-direction and η-direction respectively are shown in figures I.6 and I.7. This data is compiled from separate hammer

impacts acquired without the damper installed (Baseline Damping) and with the damper installed (Increased Damping). The time-histories were band-pass filtered to isolate the mode of interest.

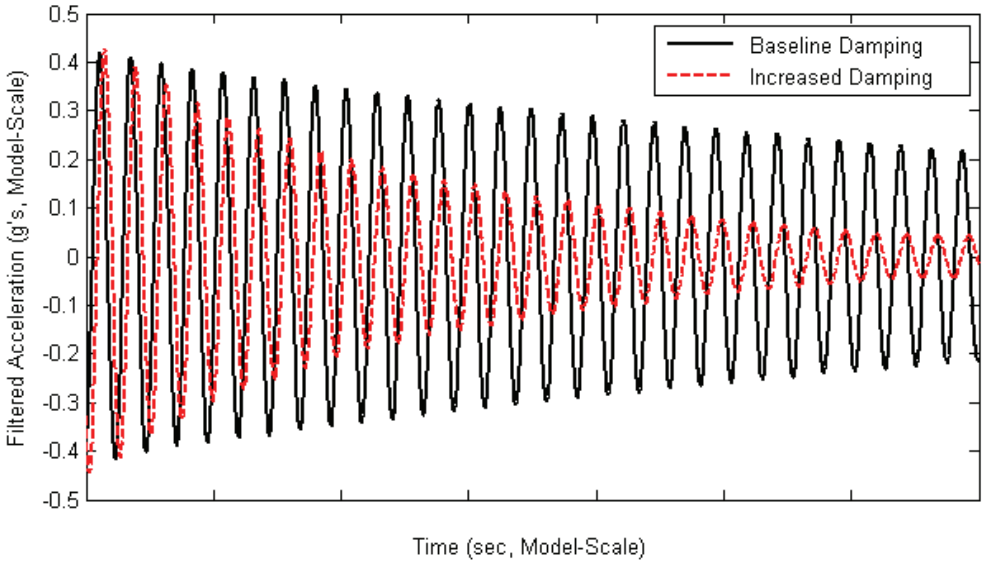

Figure I.6. Effect of Damper on Mode 1ζ During Hammer Impact, Time-History Traces of Acceleration

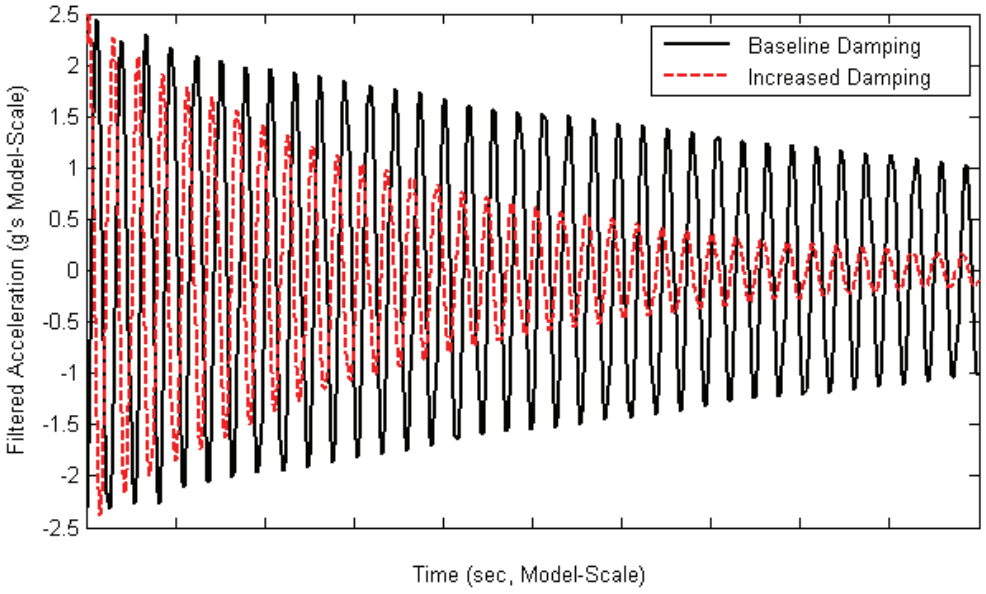

Figure I.7. Effect of Damper on Mode 2η During Hammer Impact, Time-History Traces of Acceleration

Contained in figure I.8 are time-history values of bending moment due to lift for a condition that produced a mode 1ζ resonant WIO response. One time history

presents the bending moment for the model without the damper installed and the other time history presents the bending moment with the damper installed for the same tunnel and model conditions. As one can see from figure I.8, the inclusion of the damper and the corresponding increase in structural damping has reduced the dynamic loads by an order of magnitude. The values of the axes in figure I.8 are stripped, however, the scale for both time-histories is identical.

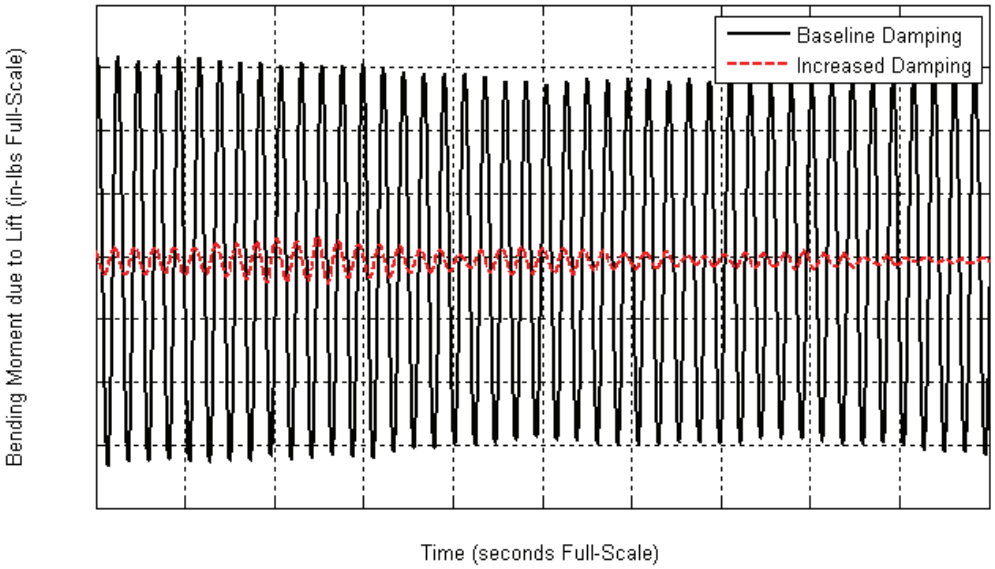

Figure I.8. Effect of Damper on Mode 1ζ Resonant WIO Response in Wind Tunnel, Time-History of Bending Moment due to Lift

Similarly, figure I.9 contains the time-history values of bending moment due to lift for a mode 2η resonant WIO response. Once again the inclusion of the damper, and corresponding increase in structural damping, significantly reduces the dynamic bending moment due to lift.

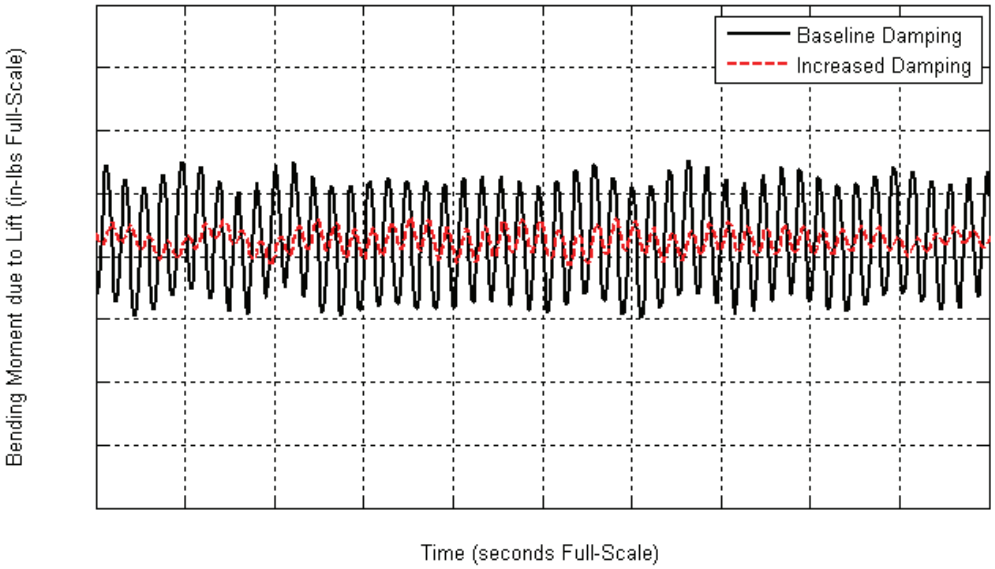

Figure I.9. Effect of Damper on Mode 2η Resonant WIO Response in Wind Tunnel, Time-History of Bending Moment due to Lift

Appendix II - Ground Wind Loads Checkout Model Data

This appendix contains summarized data from the Ground Wind Loads Checkout Model. The data in this appendix shows summarized values of bending moment organized by model configuration, followed by a section showing the frequencies and damping of the Checkout Model.

II.1 With Protuberances, Without Grit

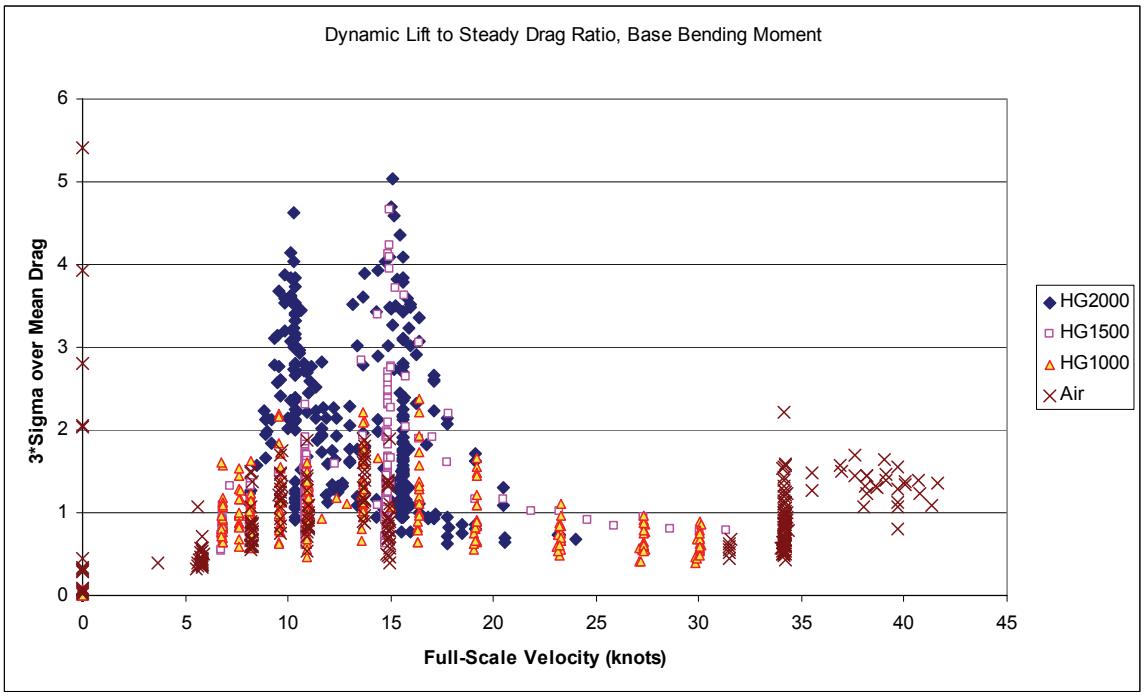

Figure II.1. Ratio of 3-Sigma Bending Moment due to Lift to Mean Bending Moment due to Drag.

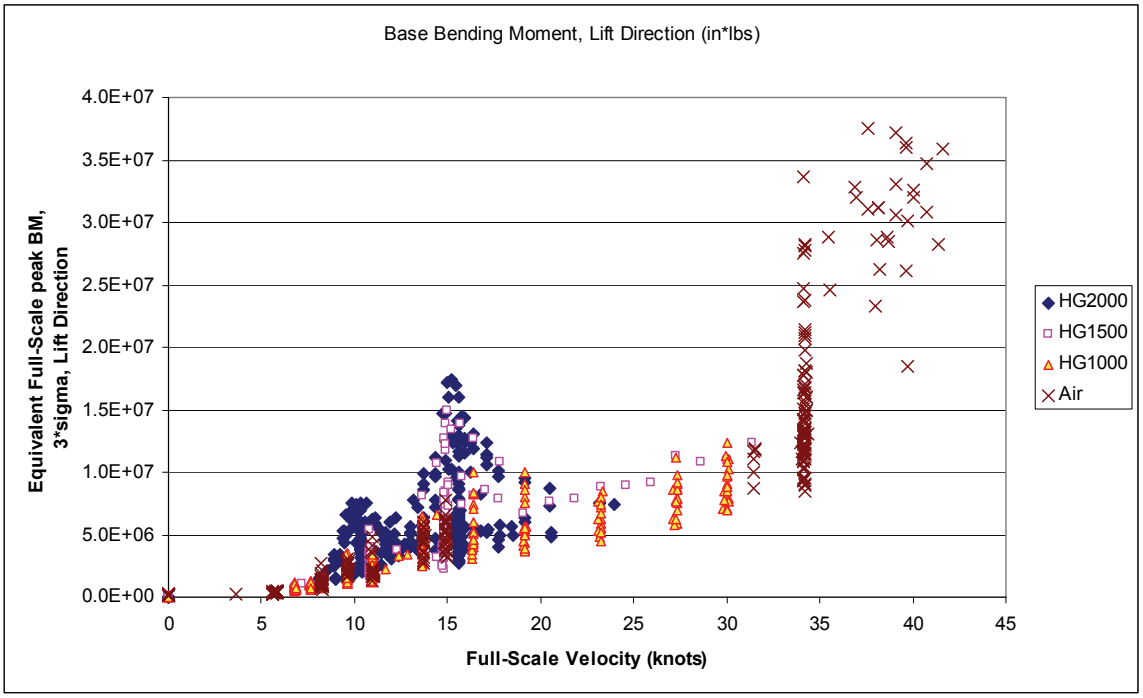

Figure II.2. Equivalent Full-Scale, 3-Sigma Bending Moment due to Lift.

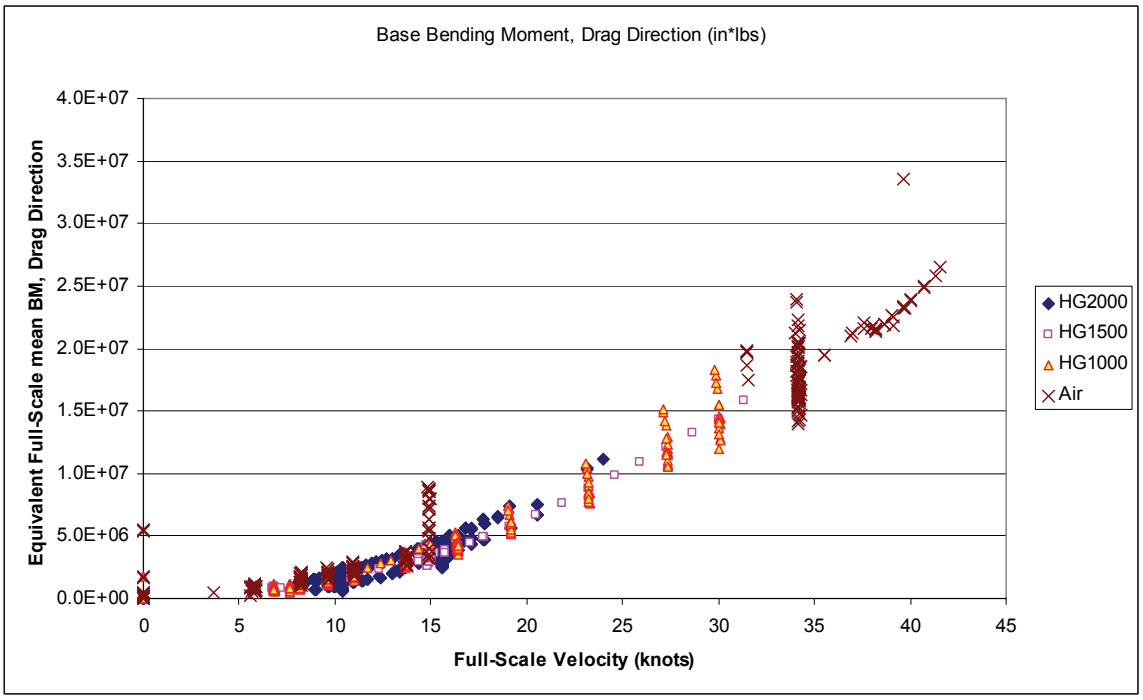

Figure II.3. Equivalent Full-Scale, Mean Bending Moment due to Drag.

II.2 With Protuberances, With Grit

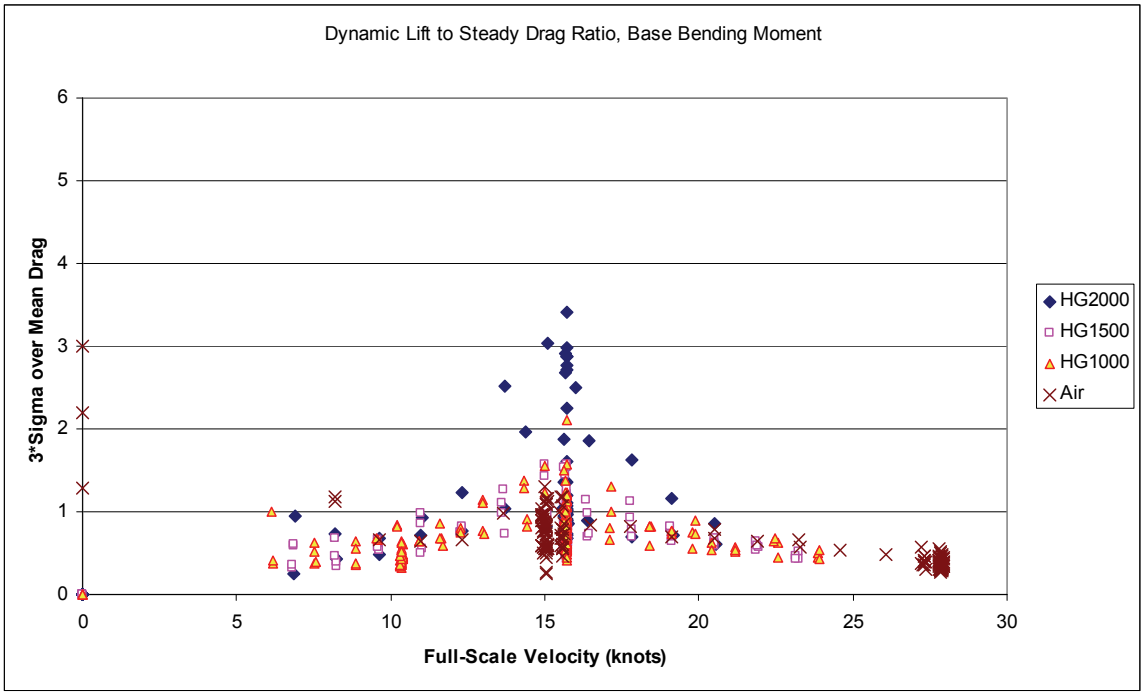

Figure II.4. Ratio of 3-Sigma Bending Moment due to Lift to Mean Bending Moment due to Drag.

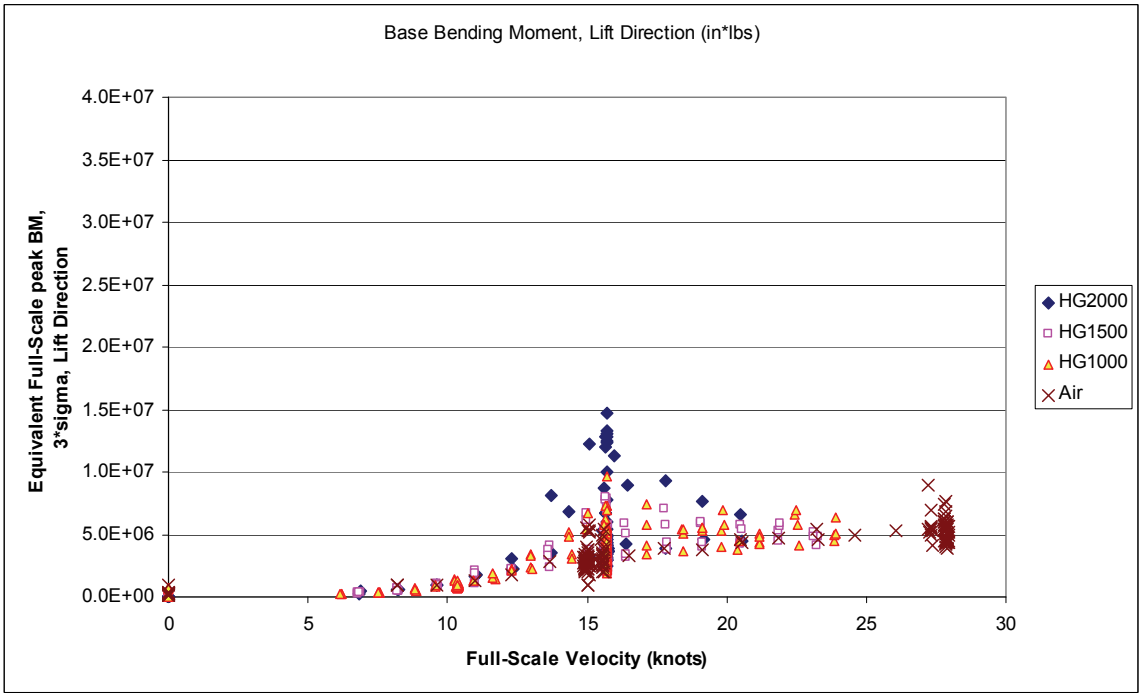

Figure II.5. Equivalent Full-Scale, 3-Sigma Bending Moment due to Lift.

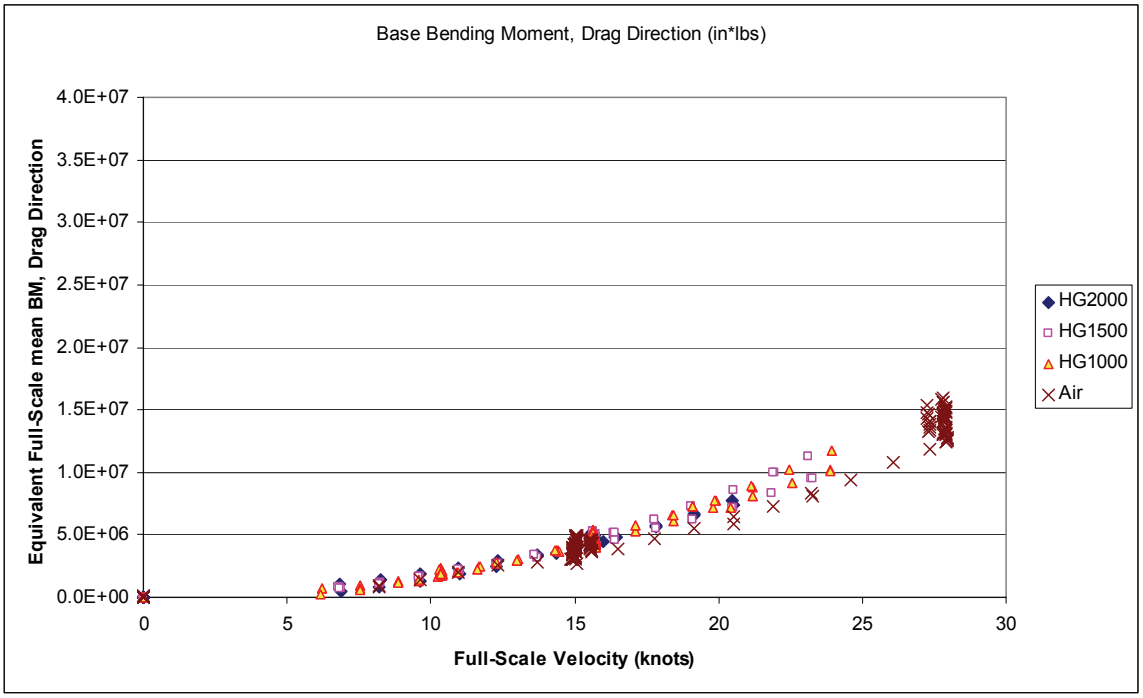

Figure II.6. Equivalent Full-Scale, Mean Bending Moment due to Drag.

II.3 Without Protuberances, With Grit

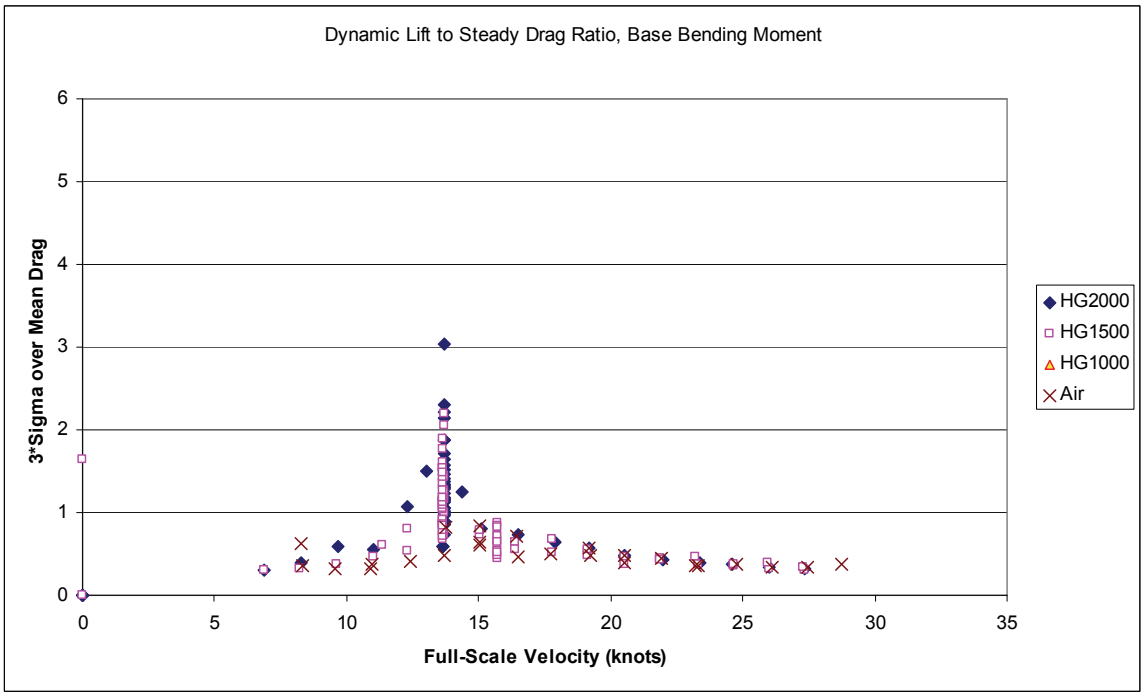

Figure II.7. Ratio of 3-Sigma Bending Moment due to Lift to Mean Bending Moment due to Drag.

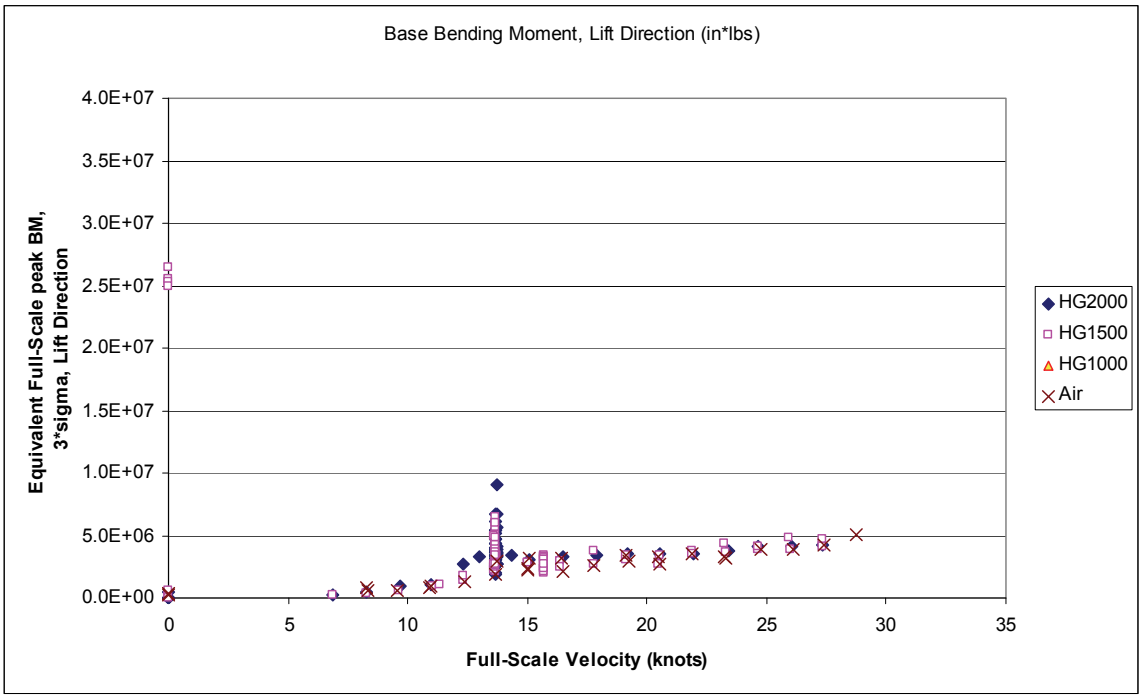

Figure II.8. Equivalent Full-Scale, 3-Sigma Bending Moment due to Lift.

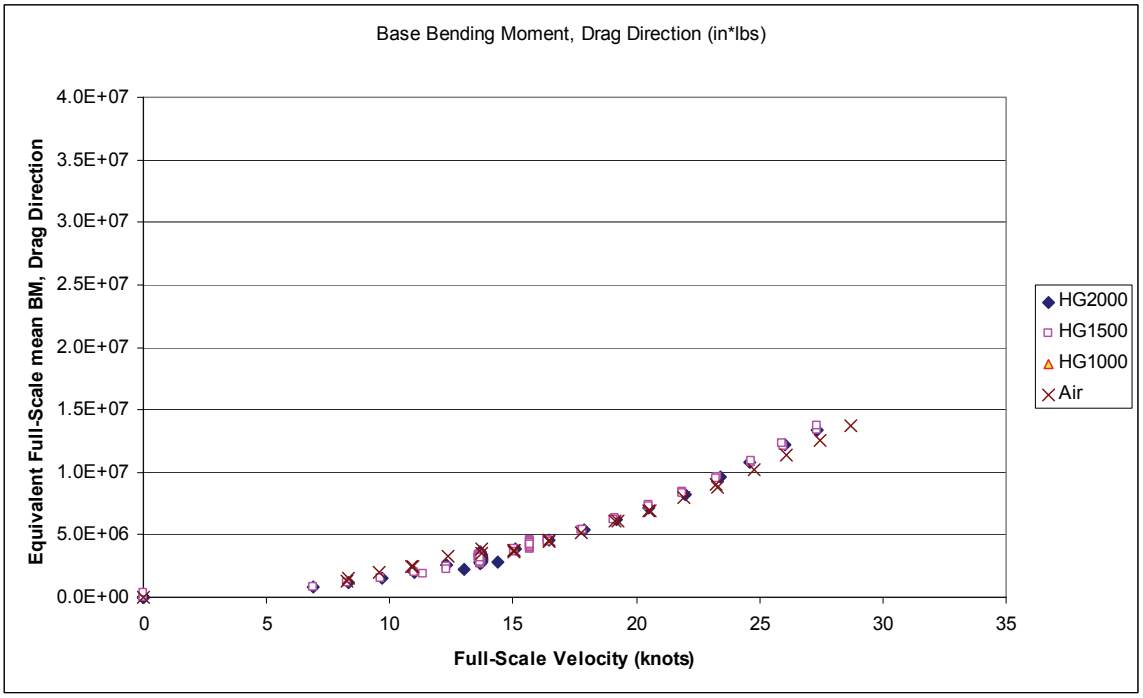

Figure II.9. Equivalent Full-Scale, Mean Bending Moment due to Drag.

II.4 Without Protuberances, Without Grit

Heavy Gas (R134a) data was not collected for this configuration.

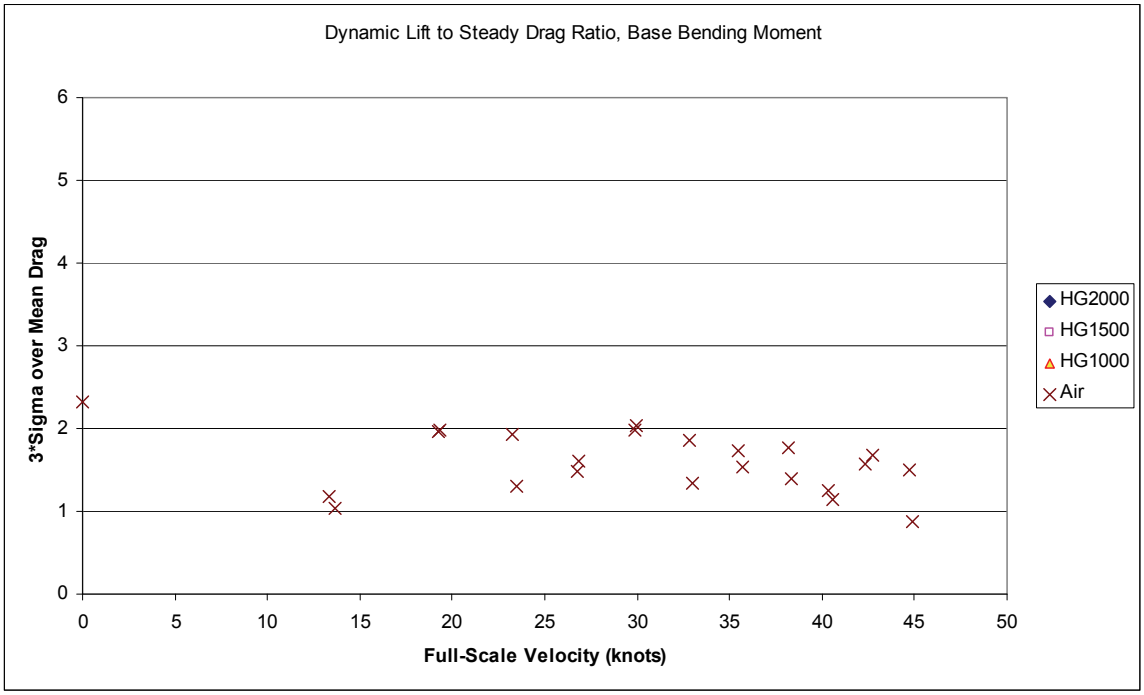

Figure II.10. Ratio of 3-Sigma Bending Moment due to Lift to Mean Bending Moment due to Drag.

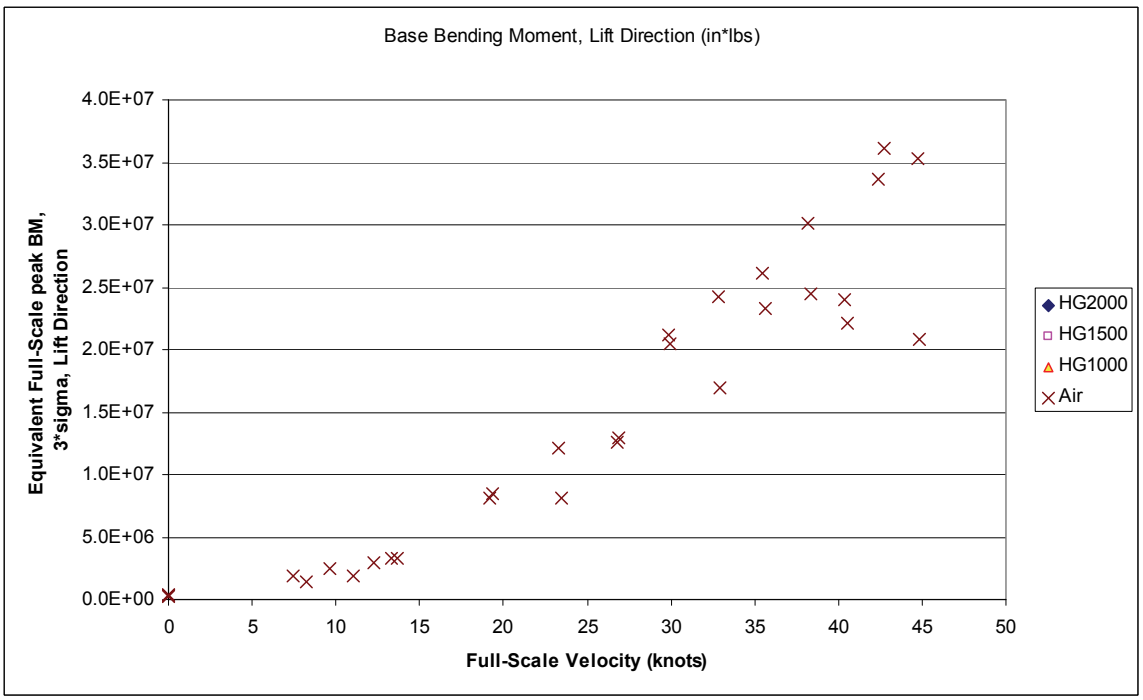

Figure II.11. Equivalent Full-Scale, 3-Sigma Bending Moment due to Lift.

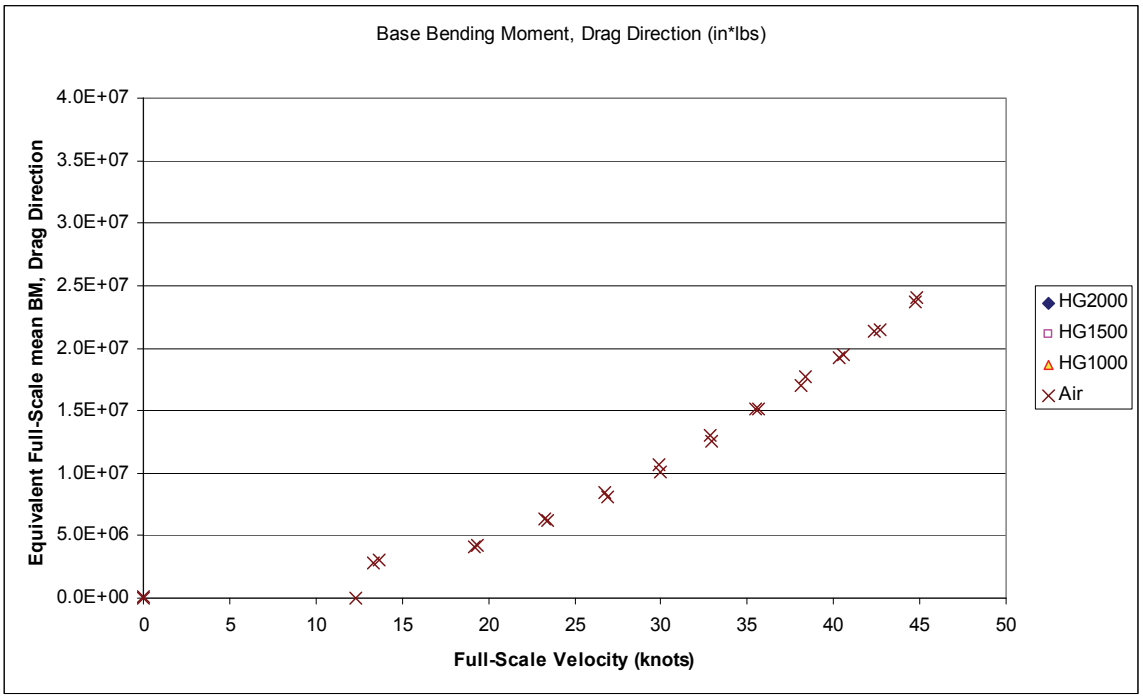

Figure II.12. Equivalent Full-Scale, Mean Bending Moment due to Drag.

II.5 Modal Frequencies and Damping of GWL Checkout Model

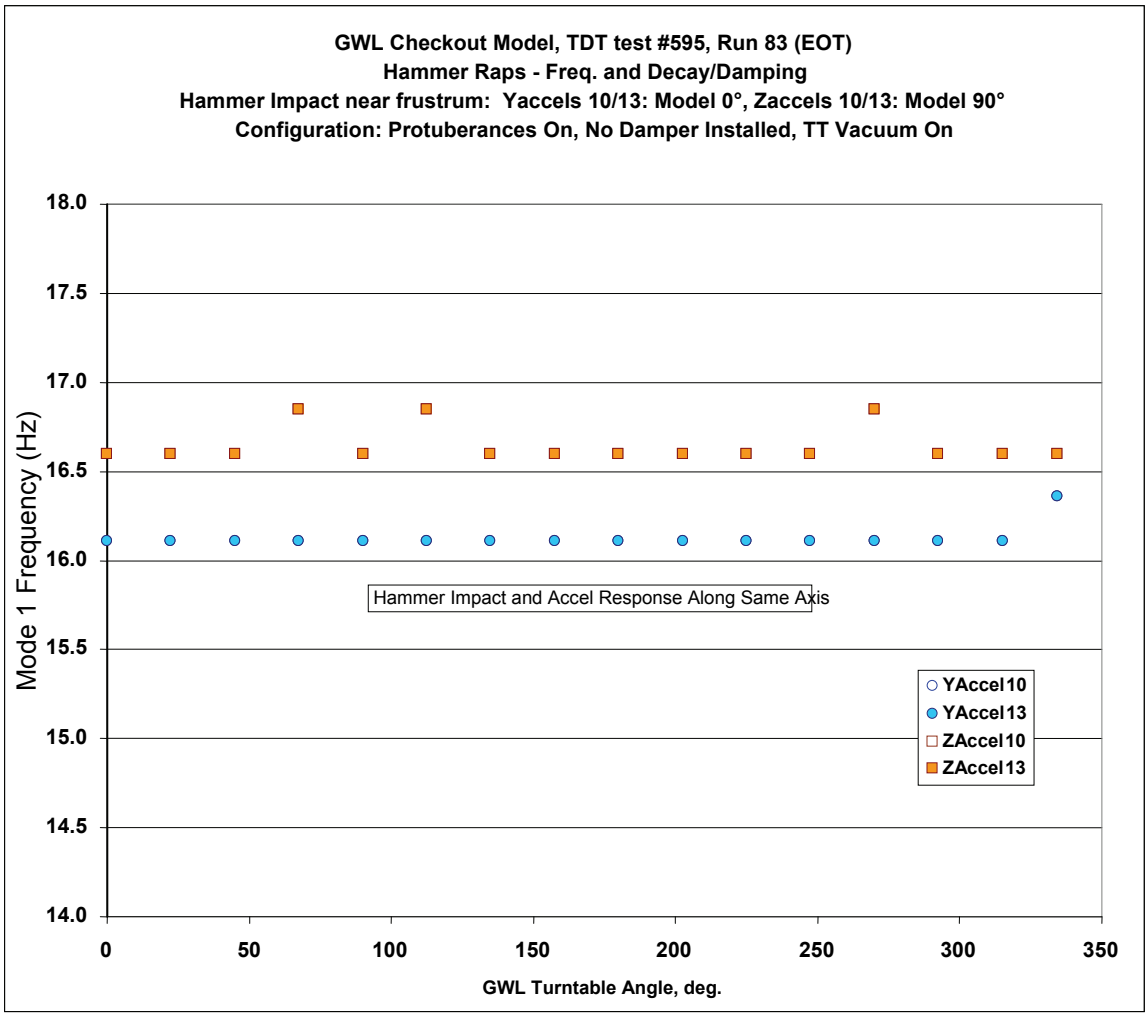

Figure II.13. First Bending Mode Frequencies, in η and ζ axes.

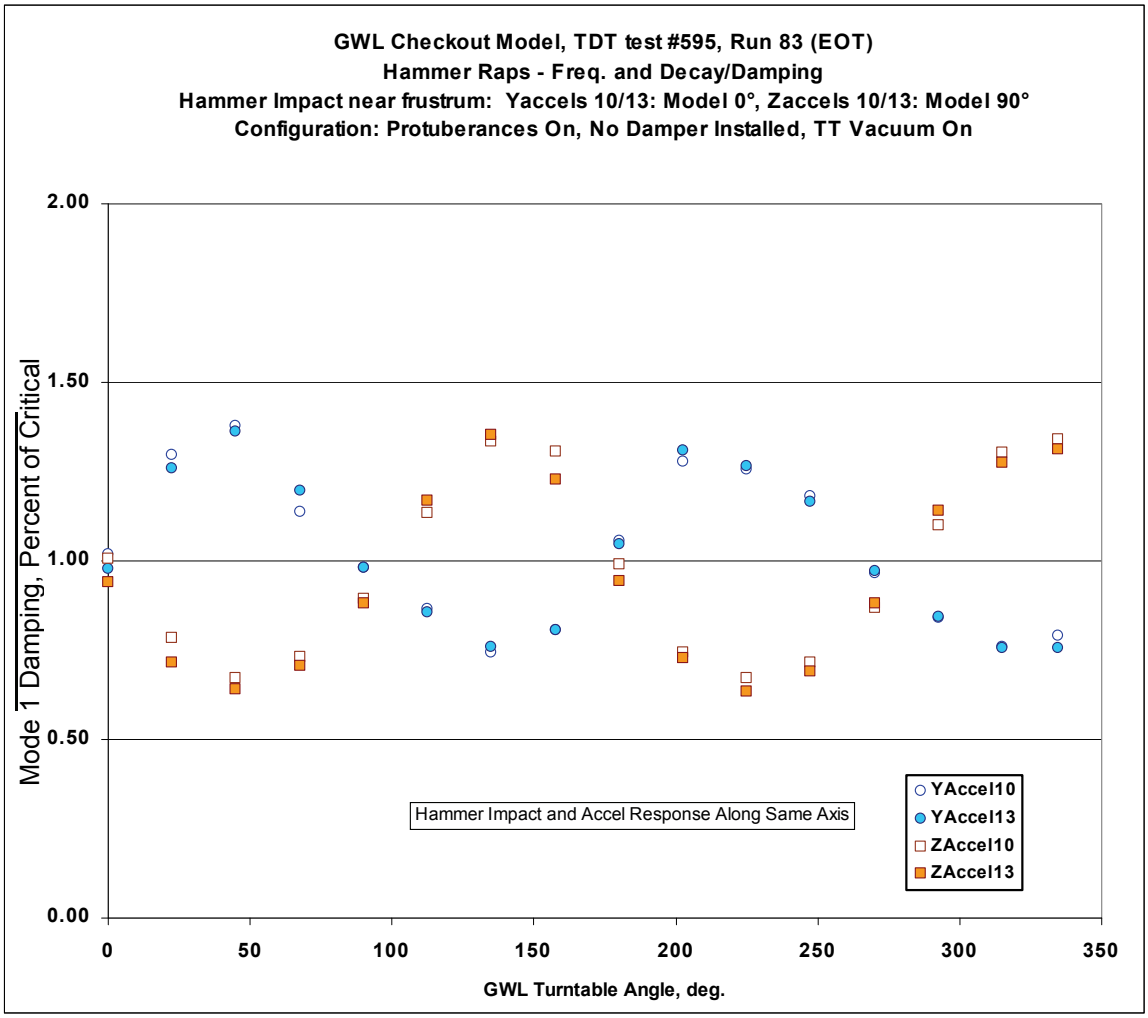

Figure II.14. First Mode Damping, in η and ζ axes, Percent of Critical.

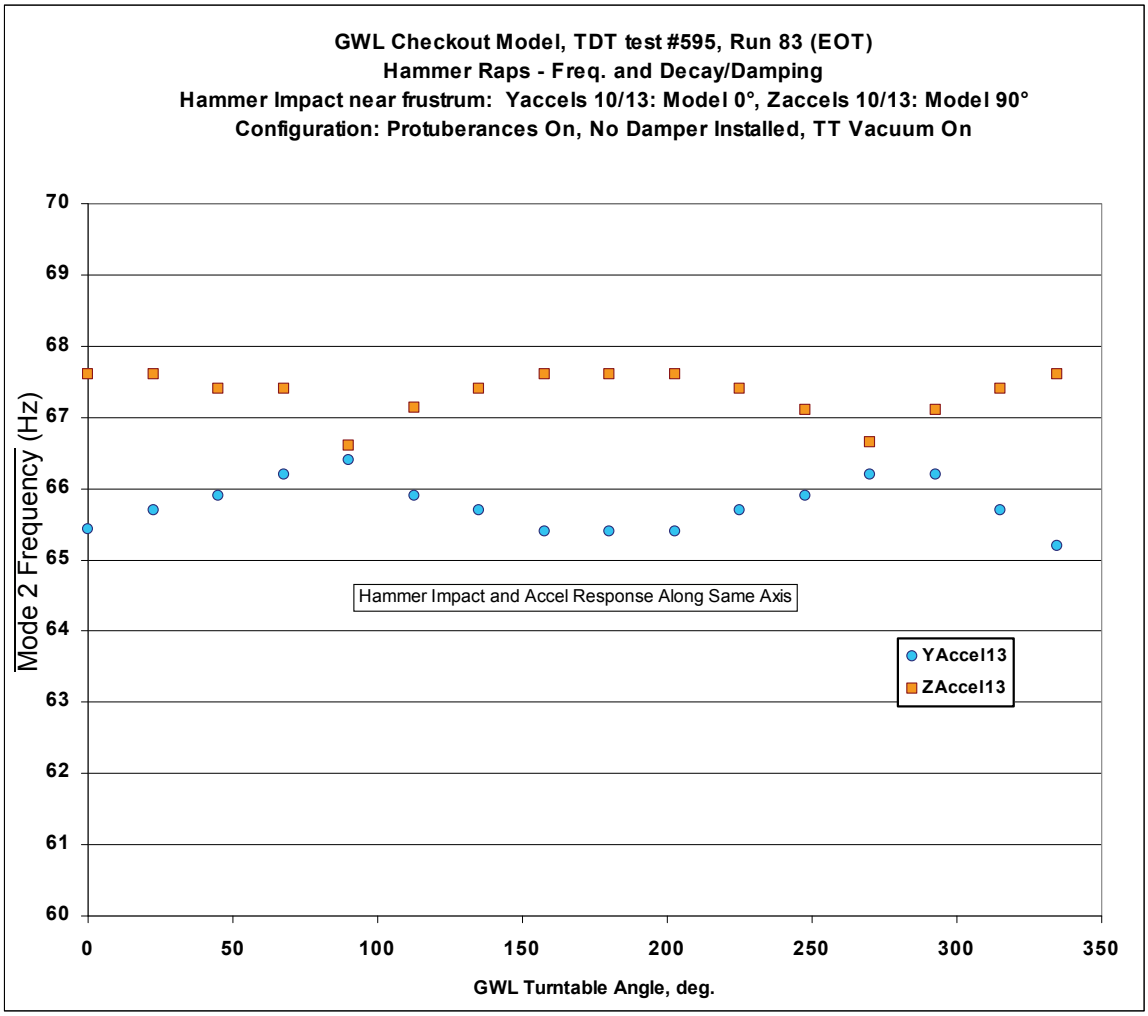

Figure II.15. Second Bending Mode Frequencies, in η and ζ axes.

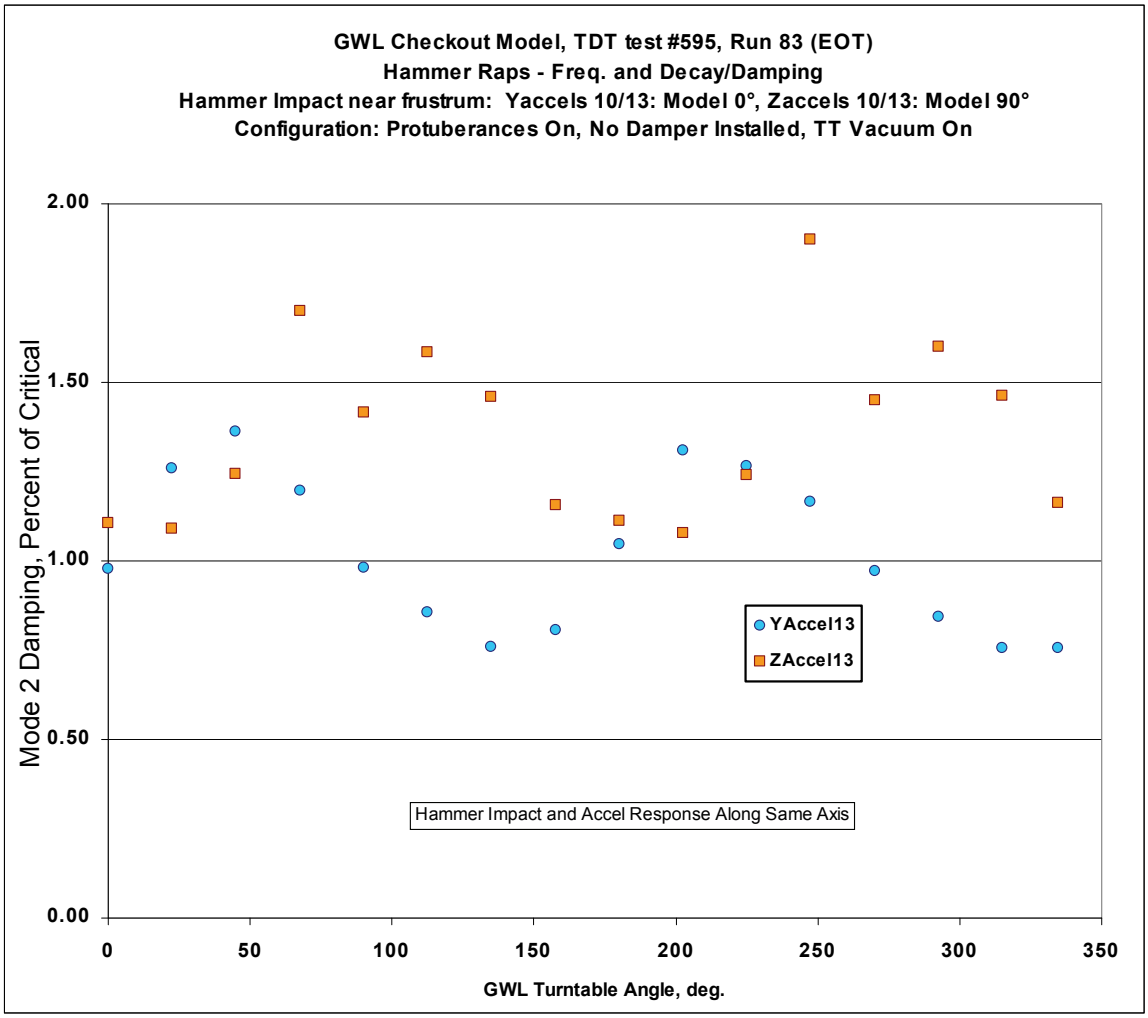

Figure II.16. Second Mode Damping, in η and ζ axes, Percent of Critical.